Summer 7-18-2014

Opto-Electronic Devices with Nanoparticles and Their Assemblies

Chieu Van Nguyen
University of Nebraska-Lincoln, chieu.nguyen@huskers.unl.edu

OPTO-ELECTRONIC DEVICES WITH NANOPARTICLES AND THEIR ASSEMBLIES

by

Chieu Van Nguyen

A DISSERTATION

Presented to the Faculty of

The Graduate College at the University of Nebraska

In Partial Fulfillment of Requirements

For the Degree of Doctor of Philosophy

Major: Chemical & Biomolecular Engineering

Under the Supervision of Professor Ravi F. Saraf

Lincoln, Nebraska

August, 2014

OPTO-ELECTRONIC DEVICES WITH NANOPARTICLES AND THEIR ASSEMBLIES

Chieu Van Nguyen, Ph.D.

University of Nebraska, 2014

Adviser: Ravi F. Saraf

Nanotechnology is a fast growing field; engineering matters at the nano-meter scale. A key nanomaterial is nanoparticles (NPs). These sub-wavelength (< 100nm) particles provide tremendous possibilities due to their unique electrical, optical, and mechanical properties. Plethora of NPs with various chemical composition, size and shape has been synthesized. Clever designs of sub-wavelength structures enable observation of unusual properties of materials, and have led to new areas of research such as metamaterials. This dissertation describes two self-assemblies of gold nanoparticles, leading to an ultra-soft thin film and multi-functional single electron device at room temperature. First, the layer-by-layer self-assembly of 10nm Au nanoparticles and polyelectrolytes is shown to behave like a cellular-foam with modulus below 100 kPa. As a result, the composite thin film (~ 100nm) is 5 orders of magnitude softer than an equally thin typical polymer film. The thin film can be compressed reversibly to 60% strain. The extraordinarily low modulus and high compressibility are advantageous in pressure sensing applications. The unique mechanical properties of the composite film lead to development of an ultra-sensitive tactile imaging device capable of screening for breast cancer. On par with human finger sensitivity, the tactile device can detect a 5mm imbedded object up to 20mm below the surface with low background noise. The second

device is based on a one-dimensional (1-D) self-directed self-assembly of Au NPs mediated by dielectric materials. Depending on the coverage density of the Au NPs assembly deposited on the device, electronic emission was observed at ultra-low bias of 40V, leading to low-power plasma generation in air at atmospheric pressure. Light emitted from the plasma is apparent to the naked eyes. Similarly, 1-D self-assembly of Au NPs mediated by iron oxide was fabricated and exhibits ferro-magnetic behavior. The multi-functional 1-D self-assembly of Au NPs has great potential in modern electronics such as solid state lighting, plasma-based nanoelectronics, and memory devices.

ACKNOWLEDGEMENT

The road to the completion of my Ph.D. program has been a long and winding journey, away from home. Through its highs and lows, knowledge accrues and character shapes. The passion and courage required for this life-time opportunity a successful one is only possible with the perpetual support and love from family and friends.

I bear a deep gratitude to Dr. Ravi Saraf for this opportunity and the constant guidance and challenges. My gratitude extends to his family for the kindness and joyous meals.

I am also grateful to our past and present group members: Dr. Vivek Maheshwari, Dr. Gaurav Singh, Dr. Rafal Korlacki, Chris Hassler, Dr. Jennifer Kane, Dr. Seung-Woo Lee, Dr. Eun-Hee Lee, Dr. Chichao Yu, Jason Ong, David Moore, Ellen Eberggren, Devor O'Connor, Steve Szalewski for making this journey rich with information and great memories. My appreciation to Dr. Maheshwari for being a mentor is undoubted. The technical expertise in machining of Mr. Leonard Akert and his friendship aided my research significantly.

Last but not least, I would like to thank Ngan Chung and Tam Nguyen for their lasting support and understanding.

TABLE OF CONTENTS

LIST OF FIGURES

LIST OF TABLES

CHAPTER 1

INTRODUCTION

Electron tunneling is a quantum mechanical phenomenon due to the wave nature of particles that has been a powerful prescription to build electronic devices. In nanostructured device this is an intrinsic principle of the system. In essence, an electron has a finite probability to "tunnel" through a potential barrier well above its total energy. If the barrier is physically thin enough, typically in few nm, there is a substantial transmission of the electrons to tunnel through. This is in stark contrast to classical physics where the transmission will be zero irrespective of barrier thickness. The principle is pervasively leveraged in most solid state devices, such as transistors, photovoltaic solar cells, light emitting diodes, and analytical instruments such as the (famous) scanning tunneling microscope, which has been central to developments in nanotechnology. We built two types of nanoscale devices based on electron tunneling. The fabrication strategy of the two devices are significantly different: The ultra-soft multilayer film tactile sensor is made by a layer-by-layer self-assembly approach; while the functionalized one dimensional (1-D) nanoparticles (NPs) necklace based single electron device is fabricated by directed self-assembly approach.

1.1 NANOPARTICLE ASSEMBLY

The last several decades have witnessed rapid and significant decrease in the size of electronics, from macro to micro and now nano-scale. This reduction is possible mainly due to advances in nanotechnology. Nanotechnology is a relatively young scientific field that studies the structures, properties, behaviors of nano-sized materials (nanomaterials) and their interactions. Nano-materials differ from macro-sized material in that at least one of their dimensions (width, length, radius, etc.) must be nano-meters (< 100nm). Counterintuitive and surprising phenomena have been discovered. The well-known laws of physics in the macro classical world are not applicable in this new scale where quantum mechanical phenomena dominate.

Spurred by curiosity and new applications, nanotechnology has been the fastest growing field in modern physics era. Nanotechnology has become a multi-disciplinary field involving chemists, physicist, engineers, biologist and pharmacists all aiming to solve problems in their respective fields by leveraging nano-scale phenomena. For example, nanoparticles are widely studied from synthesis by chemists to characterization by physicists and engineers with a variety of shapes, sizes, and geometries. Much of the research involving NPs primarily focuses on assemblies to study interactions and behaviors among themselves or with biological molecules.[1-3]

NPs assembly is a collection of individual NPs in a special arrangement of some order. A prominent method to create a large scale structure from NPs is self-assembly. This process is an autonomous process in which a larger structure (i.e. micro scale structure) is formed by a smaller (nanoscale) material without human input.[4] This

process is sometimes referred to as dimensional transformation. Self-assembly usually takes advantage of interaction such as Van der Waals, or electrostatic forces. Depending on the geometry of the basic element (nanosphere, nanorod, nanoflakes…) a wide variety of materials can be obtained with different assembling strategies.[1,5] NPs are in general coated with a surfactant and dispersed in a solvent solution. The surfactant chemistry is critical in determining the characteristics of the NPs assemblies.[2-4,6-13] 2-D assembly (monolayer) of NPs can be achieved by solvent evaporation,[6] spin-coating,[1] Langmuir-Blodgett,[8] or contact printing.[7] In all of these methods, the NPs are self-assembled to form an ordered 2-D structure in which the packing density and quality of NPs are determined by the surfactants. Disordered 2-D assemblies have also been observed by a 2 step spin-coating and evaporation method.[14] Self-assemblies of NPs naturally extend to 1-D arrays.[9,11] Also studies of nanorods have shown its versatility in self-assembling to form 1-D chains, rings, or bundles.[1,10,12,13] Diversity of self-assembling NPs and nanorods is summarized in Figure 1.1. Thus, NPs self-assembly is of great interests due to their unique electronic, photonic, and magnetic properties.[2,6,11,12,14]

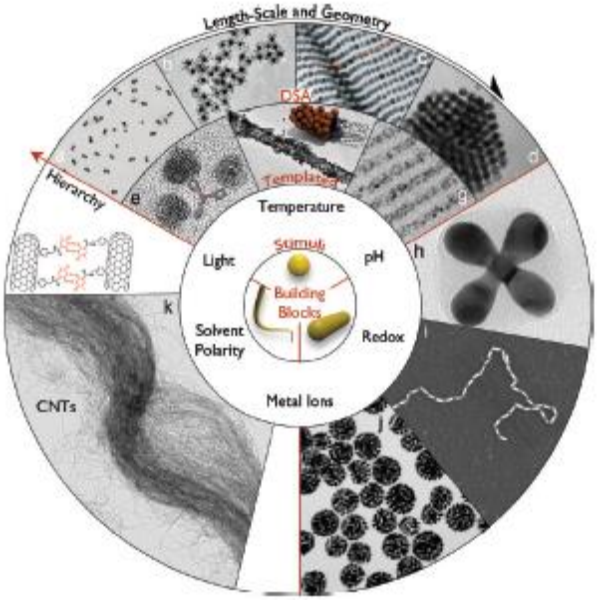

Figure 1.1 – Summary of various self-assemblies of nanoparticles by molecular interactions.[1]

Layer-by-layer Self-assembly

In nanotechnology, heterogeneous structures such as composite thin films (thickness < 100nm) have been of great interest due to their unique behaviors in electronics, magnetics, photonics, and sensors. Layer-by-layer self-assembly is a well-established method for building multilayer thin film (3-D) structures in alternating orders of polyelectrolytes;[15] polyelectrolyte and NPs;[16] and proteins/DNAs on charged surface.

Similar to self-assembled 1-D and 2-D structures of NPs (stated above), layer-by-layer self-assembly takes advantage of long-range interactions: Langmuir-Blodgett, Van der Waals, hydrophobicity, and electrostatic forces. Self-assembled multi-layer film based on electrostatic force is a simple process for depositing cation-anion polyelectrolytes; and functionalized NPs on various charged surfaces. An example of this process is shown in Figure 1.2. Typically the first step is modifying a substrate,

rendering surface charges either chemically activated in piranha solution or submerging in plasma. Next a solution of polyelectrolyte with opposite charges is dispensed on the substrate for a period of time to adsorb on the surface. Then a solution containing the NPs of interest with opposite charge to the polyelectrolyte is deposited by adsorption. Apparently each step results in a deposition of a single layer (monolayer) of each material. These steps can be repeated until a desired thickness is obtained, hence layer-by-layer. The extent of interaction of the polyelectrolyte and NPs constitutes the deposition of each layer (density of deposition, smoothness, etc.).

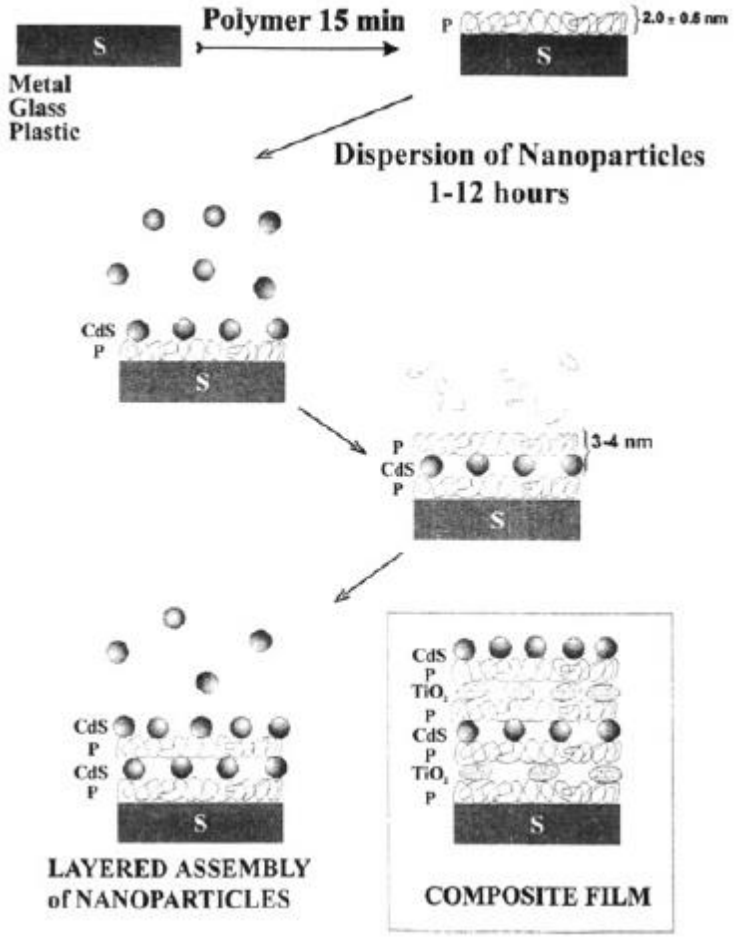

Figure 1.2 – Schematics of self-assembly of ultrathin films of alternating layers of polycations (P) and CdS NPs on metal, glass or plastic substrates (S).[16]

Layer-by-layer self-assembly method can readily be used to create interesting composite of NPs and polymers. Ultra-thin layers of polyelectrolytes on the surface of polystyrene NPs, thus modifying the NPs size, have been obtained. With a similar idea, magnetic luminescent nanocomposites (~10nm) can be achieved (Figure 1.3).[17] The layer-by-layer self-assembly strategy is also effective in building bio-sensors in which streptavidin immobilized on substrate can detect biological macromolecules such as proteins or DNA.[18] In another study Au NPs were deposited on the entire surface of live bacteria for bio-sensing application.[19]

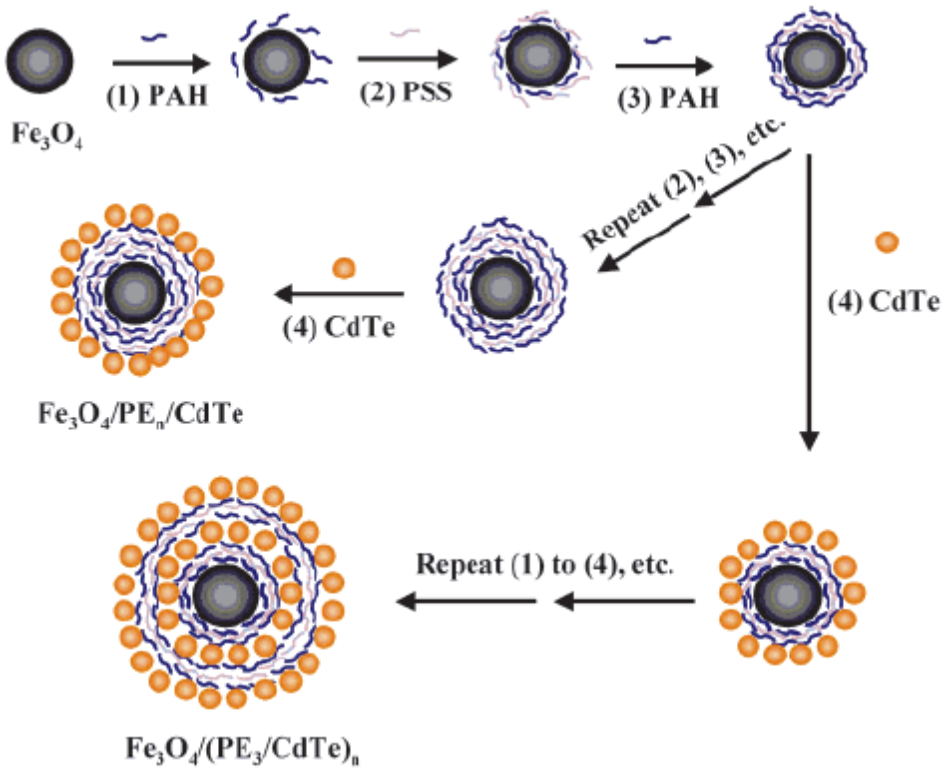

Figure 1.3 – Schematics of the layer-by-layer self-assembly of the magnetic luminescent nanocomposites.[17]

This dissertation will focus on two self-assemblies of gold (Au) NPs. The first device is based on a layer-by-layer self-assembly of Au NPs and poly-electrolytes to build a composite nanoscale thin film. The thickness was measured to be approximately 100 nm. Due to the unique void-filled 3-D structure, the thin film exhibits Zero Poisson ratio, resulting in a modulus of ~ 100 kPa, a 5 orders of magnitude decrease than a comparable polymer thin film (Chapter 2). This unusual softness leads to an ultra-high sensitivity to pressure. As a result, layer-by-layer self-assembly of Au NPs is used to make robust tactile sensor (Chapter 3). The second device is a micro meters long 1-D chains of Au NPs self-assembled by forming ion-bridges. Subsequently the ion-bridges can undergo further chemical reaction to form nanocement. The end products are multi functional single electron devices operating at room temperature (Chapter 4 and 5).

1.2 BREAST CANCER

1.2.1 INTRODUCTION

Cells are the biological building blocks of all living organisms. In human, the body is made up of several trillion various cells, all containing DNA. Under normal condition, the cells grow, divide, die and are replaced by new cells. This cycle occurs continuously in a regulated manner. Under abnormal conditions (errors in DNA by the natural reproduction processes or inheritance) cells grow and divide but do not die. In most cases, these cancer cells develop into an extra mass, called tumor.

In breast cancer, the tumor originates in breast cells.[20,21] Tumors can be categorized as benign (not cancerous) or malignant (cancerous).[20,21] They differ in the degree of invading neighboring tissue and the ability of spreading to other parts or organs of the body. Benign tumors are often not life threatening, and can be removed permanently. On the other hand, malignant tumors are life threatening, and can grow back after removed. Both men and women are susceptible to breast cancer although the occurrence is predominant in women.[20] For this reason, the current dissertation mainly focuses on breast cancer in women.

1.2.2 BREAST ANATOMY

The normal female breast includes three main parts: the lobules, the ducts and the stroma. The lobules produce milk that transports through the ducts to the nipples. The stroma contains all fatty tissue and connective tissue surrounding the lobules and ducts, as well as the blood vessels and lymphatic vessels (Fig. 1.4a). The lymphatic vessels are small veins connecting the lymph nodes (collections of immune system cells) to transport the lymph. The lymph contains tissue fluids, waste products and immune cells. The breast is mostly connected to the lymph node under the arm (axillary nodes), inside the chest (internal mammary nodes) and above or below collar bone (supraclavicular lymph nodes) (Fig. 1.4b). Depending on the types and stages, the lymph system is the most common spreading method of breast cancer cells to other part of the body.

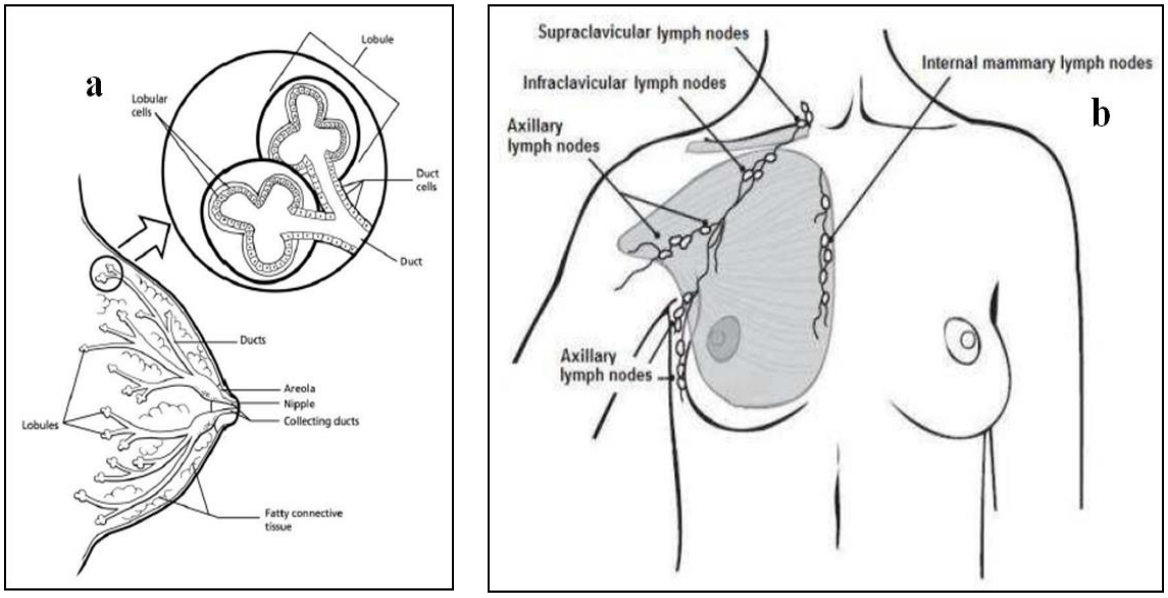

Figure 1.4 – Schematics of the female breast and its lymph nodes.[20]

1.2.3 TYPES OF BREAST CANCER

There are many types of breast cancer. The diversity depends on the origin of breast cancer and the extent of widespread. Only the most common types are described here. Ductal Carcinoma In Situ (DCIS) is the most common type of non-invasive breast cancers with about 60,000 new cases diagnosed in the U.S each year, or 1 in every 5 cases.[20] DCIS breast cancer begins from the cells in the milk ducts and is non-invasive (hence in situ).

A less common non-invasive breast cancer type is Lobular Carcinoma In Situ (LCIS), which originates from the lobules cells. LCIS is not considered a true breast cancer, but a condition with high risk of breast cancer. Invasive Ductal Carcinoma (IDC) or infiltration ductal carcinoma is the most common type of all breast cancers, accounting for about 80% of all breast cancer cases.[20] Similar to DCIS, IDC also originates from cells in the ducts, except it is invasive or has spread to the neighboring tissue of the breast, or to the lymph nodes, or to other parts of the body. Second to IDC is Invasive Lobular Carcinoma (ILC). About 10% of all breast cancer is ILC.[20] Similar to LCIS, ILC starts at the lobules but spreads to other tissues of the breast or to the lymph nodes, or to other parts of the body. Both ILC and IDC can affect women at any age. About two-thirds of women 55 or older are diagnosed with invasive breast cancer.[20]

1.2.4 BREAST CANCER STAGES

The stage of breast cancer indicates the extent of the disease. Different stages correspond to the size of the tumor, the invasiveness, and the degree of widespread. Determination of a stage is important because it dictates the treatment strategy. The most common staging system is the American Joint Committee on Cancer TNM system.[21] Each letter is followed by a number corresponding to a specific stage. The letter T with a number 0 to 4 describes the tumor size, and the degree of spread within the breast. The letter N with a number from 0 to 3 describes the possibility of cancer spreading to the lymph nodes, and the number of affected lymph nodes. The letter M with a number 0 or 1 describes the possibility of cancer spreading to distant organs such as lungs or bones.

The TNM information can be integrated into a more familiar staging system in stage grouping process, numbering from 0 to IV[21,22] (Table 1). Stage I (T1, N0, and M0) indicates a tumor size less than 2cm, and the cancer has not spread to the lymph node (IA) or cancer cells have been found in the lymph nodes (IB). Stage II means larger tumor size (2 to 5cm), and cancer cells may or may not be spreading to underarm lymph node. Stage III indicates tumor size of about 5cm and the cancer has spread to the underarm lymph nodes, the lymph nodes behind the breastbone, or the lymph nodes above or below the collar bone. In stage IV, the tumor can be of any size, and cancer has spread to distant organs.

Stage	Tumor Size	Invasiveness	Extent of Spread	5-year Surviving Rate
0	Negligible	No	Has not spread	100%
IA	< 2cm	No	Has not spread	100%
IB	< 2cm	Yes	Spread to lymph nodes only	100%
IIA	< 5cm	Yes	Spread to underarm lymph nodes only	93%
IIB	2 - 5cm or larger	Yes	Spread to underarm lymph nodes only	93%
IIIA	< 5cm	Yes	Spread to underarm or behind-breast-bone lymph nodes only	72%
IIIB	Any size	Yes	Spread to chest wall or skin, axillary lymph nodes only	72%
IIIC	Any size	Yes	Spread to 10 or more axillary lymph nodes or lymph nodes under and above collar bone	72%
IV	Any size	Yes	Spread to distant organs, most likely in bone, liver, brain, lung	22%

Table 1.1 – Staging of Breast Cancer and Relative Survival Rate.[20]

Today breast cancer (and all other cancers) is still an incurable disease. However early detection (during stage I) can completely eliminate breast cancer mortality.[20-22]

1.2.5 BREAST CANCER SCREENING MODALITIES

Currently there are three most common screening modalities widely employed to diagnose breast cancer.[21-23] The method of choice is mammography. The others are clinical breast examination (CBE) and magnetic resonance imaging (MRI). Due to various working principles, each method has its own advantages and limitations.

Mammography is the most commonly used screening method in breast cancer.[20-23] Mammography is an x-ray imaging method in which a low dose of x-ray material must be injected into the breast. A black and white image (mammogram) of the breast is then acquired by a detector. The contrast (black to white) in a mammogram reflects the variation in tissue density of the breast. Thus a mass would appear brighter than the normal surrounding tissue. Due to this characteristic, mammography often produced false positives or over diagnosed results in women with more dense breasts, leading to patience anxiety and unnecessary follow-ups. Therefore, mammography is only recommended for women 40 years of age or older, and women with high risk factors. In younger women (in their 20s or 30s) mammography may increase the risk of breast cancer due to x-ray exposure. Modern dedicated breast mammography instruments are capable of higher sensitivity with a smaller amount of required x-ray material. Other limitation includes substantial cost, and lack of access in developing countries. Mammography can detect breast cancer tumors about 10mm in size.[24]

Clinical breast exam is an effective screening method complementary to mammography. Currently its effectiveness as a primary screening modality is questionable. In CBE, a professional physician manually feels the breast (palpate) for

any abnormal lumps (Fig. 1.5).[25] The method is based entirely on human sense of touch through palpation. Thus CBE result is subjective, depending on the proficiency of the physician in palpation for lumps; and the palpation procedure itself.[25] Despite these limitations, CBE has been shown to detect breast cancer tumors often missed by mammography. The minimum tumor size detected by CBE is 21mm.[26] Breast cancer is often found by human fingers, either of a professional (CBE) or of the patient self (breast self-exam, BSE).

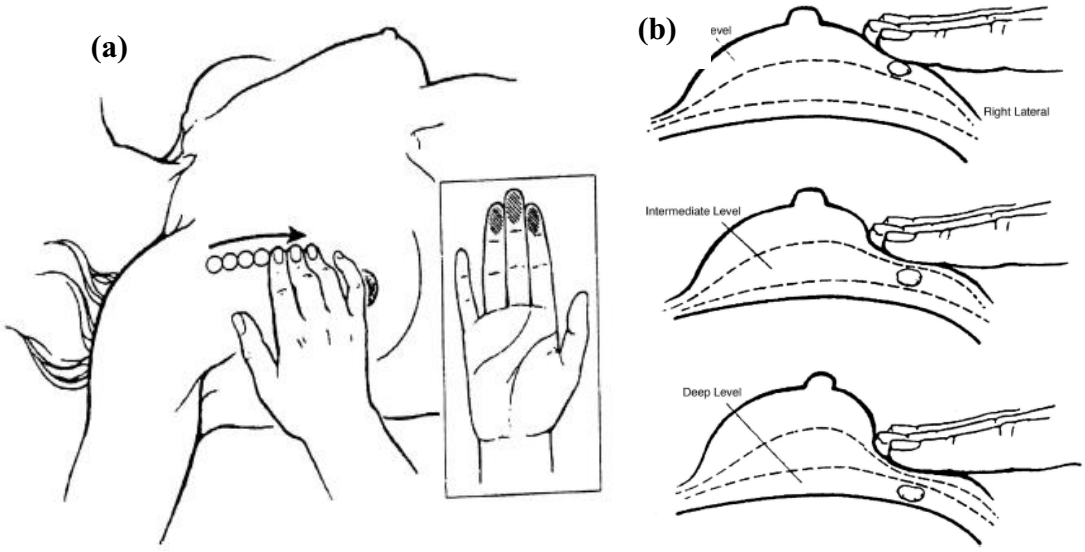

Figure 1.5 – Recommended palpation technique (a) and levels of pressure for palpation of breast tissue (b).[23]

MRI is a screening modality that is more sensitive than mammography.[21,23] MRI is NMR – based tomography to measure, say H_2O content as a function of depth. With this contrast mechanism, breast cancer tumor can be detected. MRI is very sensitive in detecting tumor it often produces false positive results.[23] Thus, it is only recommended for women with 15% risk or higher. It is more expensive than mammography and

requires the patient keeping still in a small enclosure for up to one hour. Similar to mammography, breast cancer MRI also requires dedicated instruments specifically for imaging the breast.

1.2.6 DIFFERENTIATION OF BENIGN/MALIGNANT BREAST CANCER TUMORS

Knowledge of the mechanical properties of breast cancer tumors is necessary in designing screening and detection approaches. In addition to its size, a tumor can be detected based on its stiffness compared to the surrounding normal tissue and its location as well as its depth from the breast surface. In general, a breast cancer tumor is 8 to18 times stiffer than the neighboring tissue (table 2).[27] As the cancer progresses, the tumor stiffness increases. This can be attributed to the fact that the tumor is a built-up mass of immortal cells.

Tissue Type	Elastic Modulus at Strain 0.01	SD	Elastic Modulus at Strain 0.05	SD	Elastic Modulus at Strain 0.10	SD	Elastic Modulus at Strain 0.15	SD
Fat	4.8	2.5	6.6	7	10.4	7.9	17.4	8.4
Gland	17.5	8.6	33	12.0	88.1	66.7	271.8	167.7
Phyllodes Tumor	56.6	0.0	90.8	8.6	164.3	0.0	297.7	0.0
Papilloma	22.2	5.8	54.4	19.7	169.7	80.6	537.8	209.1
Lobular Carcinoma	34.7	0.0	78.9	0.0	221.8	0.0	628.4	0.0
Fibroadenoma	45.5	20.1	100.5	39.6	288.4	110.9	889.2	205
Infiltrating Ductal Carcinoma	47.1	19.8	115.7	42.9	384.5	126.9	1366.5	348.2
Ductal Carcinoma in Situ	71.2	0.0	188.7	0.0	638.7	0.0	2162.1	0.0

Table 1.2 – Stiffness of normal breast tissue and breast cancer tumors.[26]

The shape (boundary) of the tumor can help distinguish between benign and malignant tumors which is important in screening. Studies have shown most of benign tumors are round with continuous circumferences, while malignant tumors are spiculated

with rough edges and corners (Fig. 1.6).[28] Thus, accurate identification of the overall shape of the tumor is highly desired in screening method.

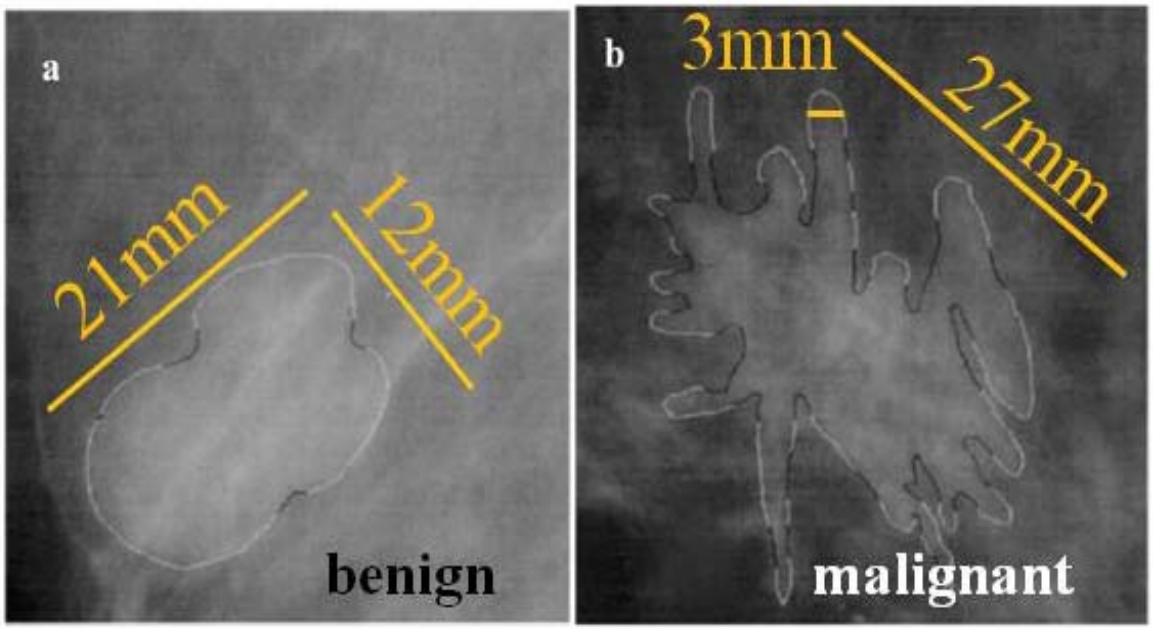

Figure 1.6 – Cross – sectional mammograms of benign (a) and malignant (b) tumors in breast cancer. Image size is 31.5 x 36.5 mm in (a), and 37.2 x 47.7 mm in (b).[27]

1.3 TACTILE SENSOR

1.3.1 HUMAN TOUCH

Touch is a highly critical way humans interact and perceive our tangible surroundings. Humans rely on the sense of touch for all physical activities ranging from grasping, texture feeling, to writing and reading. Unlike other senses such as vision or audition, touch does not belong to any localized sensory organ[29] but rather contributed entirely under the skin. Skin is the largest organ covering the entire human body. Due to this wide diversity, touch sensitivity differs from one region to another. One of the most sensitive areas is the fingertip.[30] Thus the current dissertation describes touch sensation by human fingertips from here on.

The sense of touch is achieved through a sophisticated process. In general, tactile perception of shape/roughness is a product of (i) pressure mapping transduction of the skin outer most layer (the epidermis) to the mechanoreceptor located in the inner layer (the dermis) resulting in a signal relayed to the brain; and the translation process of the stimulated signal by the brain.[29,30] Most of research on touch focuses primarily on the former process. There are 4 types of mechanoreceptors (Figure 1.7). Each type of mechanoreceptors is optimized for different purposes (Table 3).[29] In addition, the conformity of the epidermis and dermis layers of the fingertips are optimized for discerning shapes and surface features. As a result, human fingertips can detect surface roughness at a spatial resolution of 40um and at stress level at small as 10-40 kPa.[31] Recently it has been demonstrated that human fingertip can distinguish a minimum

amplitude of 10nm surface wrinkles with a wavelength of 760nm.[32] Therefore nanotechnology plays an important and promising role in mimicking touch sensation.

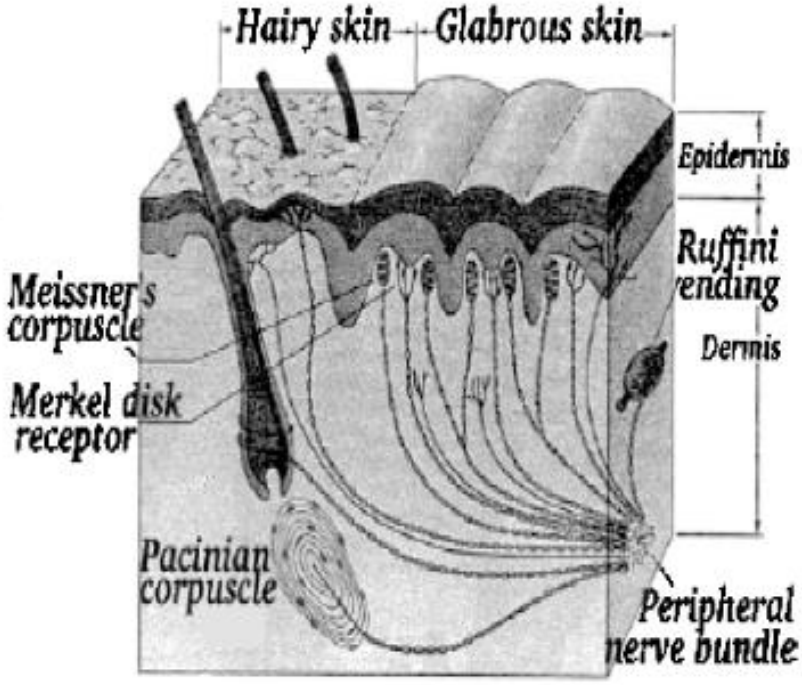

Figure 1.7 – Mechanoreceptors in human fingertip.[28]

	Receptive Field	**Response Characteristics**	**Primary Function**	**Density*, cm^{-2}**
Merkel cells	Small (Type I)	Slow Adapting (SA I)	-Coarse texture and pattern detection -Stable precision grasp and manipulation	70
Meissner corpuscles	Small (Type I)	Rapid Adapting (RA I)	-Low frequency detection -Stable precision grasp and manipulation	140
Pacinian corpuscles	Large (Type II)	Rapid Adapting (RA II)	-High frequency detection -Fine texture detetion -Stable precision grasp and manipulation	21
Ruffini endinds	Large (Type II)	Slow Adapting (SA II)	-Direction of object motion and force due to skin stretching Finger position	49

Table 1.3 – Summary of mechanoreceptors under human fingertips.[29,30]

*: Density is number of sensor per cm^2.

1.3.2 TACTILE SENSOR

In recent years, tactile sensors or electronic skin have been rapidly renewed in interest due to advances in nanoscale fabrication and new discoveries of nano-materials.[33-40] Tactile sensors are electronic devices that mimic the sense of touch through local pressure mapping by a transduction method. The sense of touch is deemed extremely useful in several technological fields such as robotics, minimally invasive surgery, and remote sensing applications.[34,38-40] In robotics, tactile perception still remains an interesting challenging due to its complex nature.[40] Tactile information regarding roughness or smoothness, softness or stiffness completely lacks in minimally invasive surgery.[34] In general, tactile devices are made of arrays of pressure-sensor elements (similar to pixels in digital images) based on several transduction principles such as piezoelectric, piezoresistive, optical (IR), and vibration.

Depending on the design, these pressure sensitive elements are usually fabricated using the bottom-up procedure. Despite their differences, the result is displayed as a 2-D or 3-D pixelated image via an interpretive software and complex electronics.[33,36] Compared to human fingers (spatial resolution of 40um in a stress range of 10-40 kPa[31]) the current tactile sensor can distinguish surface roughness at a spatial resolution of 2mm.[41] In order to achieve spatial resolution comparable to human finger, an approximate 500x500 sensory array is needed over an area of 1cm^2.

Capacitive tactile sensors utilize an array of capacitor cells as active sensing elements.[42-44] This type of sensor can image stress distribution by measuring change in local capacitance. Usually a capacitive tactile senor is fabricated using MEMS

technology in which the bottom (fixed) electrode is topped by floating electrode, and separated by flexible spacer, like rubber, silicon, or elastomer dielectrics. Because each sensing element is a capacitor, its capacitance is sensitive to the separation distance between the electrodes which changes with applied pressure. Thus the sense of touch is achieved and the result can be visualized in a tactile image. Capacitance based tactile sensors exhibit a linear response to stress with high sensitivity but are susceptible to external noise.[34]

Piezoresistive tactile sensor is based on the intrinsic property of the active sensing material, the piezoresistivity.[45-48] Piezoresistivity materials transduce applied forces to a change in electrical resistance. A piezoresistive based tactile sensor is constructed with bottom (fixed) electrode and a floating to electrode, sandwiching an thin film of piezoresistive material, such as silicon, carbon nanotube, graphene, and conductive polymer composite.[34] Due to the simple structure, this type of tactile sensor is the most successful approach to building larger area device over 10 cm^2, especially for polymer composites. Research has shown that a spatial resolution of 1mm can be achieved with a piezoresistive tactile sensor, which is the highest for any tactile device with an area of 1 cm^2. CNTs and graphene also attracted significant attention due to their unique electrical and mechanical properties, exhibiting exceptional sensing capabilities.

Piezoelectric tactile sensors measure a generated voltage in the active sensing material by an applied force.[34] It depends on a unique electro-mechanical property called piezoelectricity, or the ability to generate a voltage according to the mechanical strain of the material. The tactile device is also arranged in an array structure comprised of many cells or pixels. Piezoelectricity occurs in highly crystalline materials such as lead

zirconium titanate (PZT), or ZnO. Polymers such as poly (vinylidene difflouride) (PVDF) have also shown piezoelectricity.[34]

Optical tactile sensors operate based on changes of intrinsic (intensity, phase, and polarization) and extrinsic (reflection and deflections) properties of light.[49,50] In robotic applications, the extrinsic properties based sensor is the most widely used sensor due to its simplicity. These types of sensors are comprised of 3 parts: a light source, transmission medium and a detector. Typically, light from the light source is reflected or blocked from the detector through the transmission medium by external forces on the detector, resulting in a digitized signal. Light used in this tactile sensor is usually in the infrared range for transparency purposes, though several devices based on visible light laser have been demonstrated.[34]

There are several other principles that tactile sensors can be built upon such as magneto-resistivity, and vibration reflection.[34] These types of tactile devices are not well-studied and still under development, and hence not mentioned here in detail. A majority of researches focus on detection of surface features or properties, like surface roughness, and shape. The palpation function of touch is a less-explored area that is vital in CBE for breast cancer screening and melanoma detection. The first part of this dissertation describes a NPs based tactile sensor optimized for palpation touch.

1.3.3 TACTILE IMAGING

Tactile imaging is a new and emerging field aiming at detection through visualization of palpable structures.[51] It begins as an effort to provide tactile sensation during minimally invasive surgery. For the last decade, most of research on tactile imaging focused on feeling for lumps under human skin, or palpation, especially in breast cancer.[52-55] As previously stated, palpation of the breast for an abnormal tumor (lump) is the fundamental principle of CBE and BSE. Palpation is the ability to detect an object (size, shape, stiffness, and roughness) imbedded under the surface. The minimum sized of tumor detected by CBE is 21mm[26] while mammography, the current most effective breast cancer screening modality, can detect a tumor size of 10mm.[24] This limitation corresponds to detection of stage III or above breast cancer with a 5 year survival rate of 50%.[21] Early detection of breast cancers (during stage I or II) where tumor size is 5mm or less leads to 100% 5-year survival rate.[21]

Tactile imaging seeks to achieve this important function of touch, augmenting the subjective CBE screening. Several tactile devices have tackled this challenge with different approaches: piezo-resistive pressure sensor,[55] piezoelectric finger,[56] vibration based pressure sensor,[57] and optoelectronic mechanic tactile sensor.[58] Among these approaches, the optoelectro-mechanical tactile sensor has shown the best sensitivity. 10mm spherical tumors can be detected up to 20mm deep under the surface with a stiffness contrast of 5-8 folds compared to its surrounding.[58] This device demonstrates an equivalent result to CBE. However, its high spatial resolution (2.8mm) is not optimized for smaller tumor size (< 10mm). In addition there are two commercially available tactile imaging systems, Sure Touch (by Medial Tactile Inc.) and another by Assurance Medical

Inc. Both systems have been used in clinical studies to detect breast cancer tumor and showed to be effective.[55] However, the discrepancy in size detected by these tactile systems and actual value (obtained by lumpectomy) limits their validity as an individual screening tool. Thus there is an urgent need to develop a large-area tactile sensor with better sensitivity and effectiveness to aid the invasive mammography and subjective CBE in breast cancer screening.

1.4 SINGLE ELECTRON DEVICE

Silicon and other semiconducting materials are key components in modern electronic devices from personal computer to robotics, sensor, and solar cells. One of the most important characteristics of semiconducting materials is the unusual non-Ohmic electronic transport. Instead of a linear relationship, current (or electrons) flowing in semiconducting devices (p-n junctions) in forward modes is characterized with a critical bias. Below this bias the current is insignificant. Beyond the critical bias current rises exponentially as $J \sim \exp[e(V-V_g)/kT]$ (Fig. 1.8).[59] The current on/off ratio, i.e. gain, is usually more than 5 orders of magnitude. This characteristic makes semiconductor ideal materials for building digital transistor which is at the heart of modern electronics.

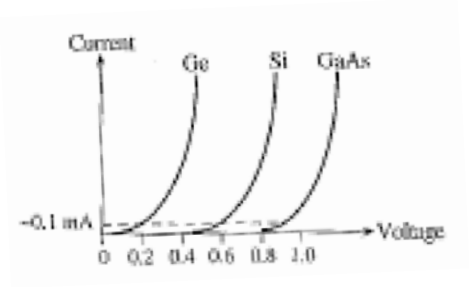

Figure 1.8 – Electronic characteristics of Ge, Si, GaAs p-n junctions.[58]

Another type of material has also shown similar transistor behavior with on/off states is percolating arrays of metal NPs.[60-62] Several studies have shown that 2-D arrays of An NPs[61] and Co NPs[62] self-assembled between two electrodes exhibit non-linear electronic transport behavior with an apparent threshold bias, V_T, and a gain constant, ξ. This behavior is attributed to the local charging effect of multiple NPs by a single electron, i.e. single electron effect. As a result, at low bias a potential barrier is created by the single electron effect, thus blocking the current, i.e. Coulomb blockade.[63] Above

V_T, the electron has enough power to overcome this barrier, and current rises as $I \sim (V/V\text{-}V_T)^{\xi}$.[60] However this transistor-similar behavior has only been observed at cryogenic temperature.[60-62] Thus modification to the 2-D array of metal NPs to achieve single electron effect at room temperature is of importance. A very efficient method is to further confine the dimension of NPs assembly to local 1-D.[64] Quantum confinement in 1-D nanomaterials such as nanowires (NWs) and nanotubes (NTs) have enabled numerous advantages in designing and building nanoscale devices such as solar cells, lasers, nano actuators and force sensors.[65] Using a simple strategy, Maheshwari, Kane, and Saraf achieved a 2-D array of Au NPs with 1-D locality (quasi 1-D structure) by bridging the negatively charged NPs with Cd^{2+} ions and later cementing them with Na_2S solution (Fig. 1.9).[64] Due to the local 1-D nature of this material, single electron effect was observed at room temperature with a non-linear collective electronic transport in agreement with theoretical prediction.[60]

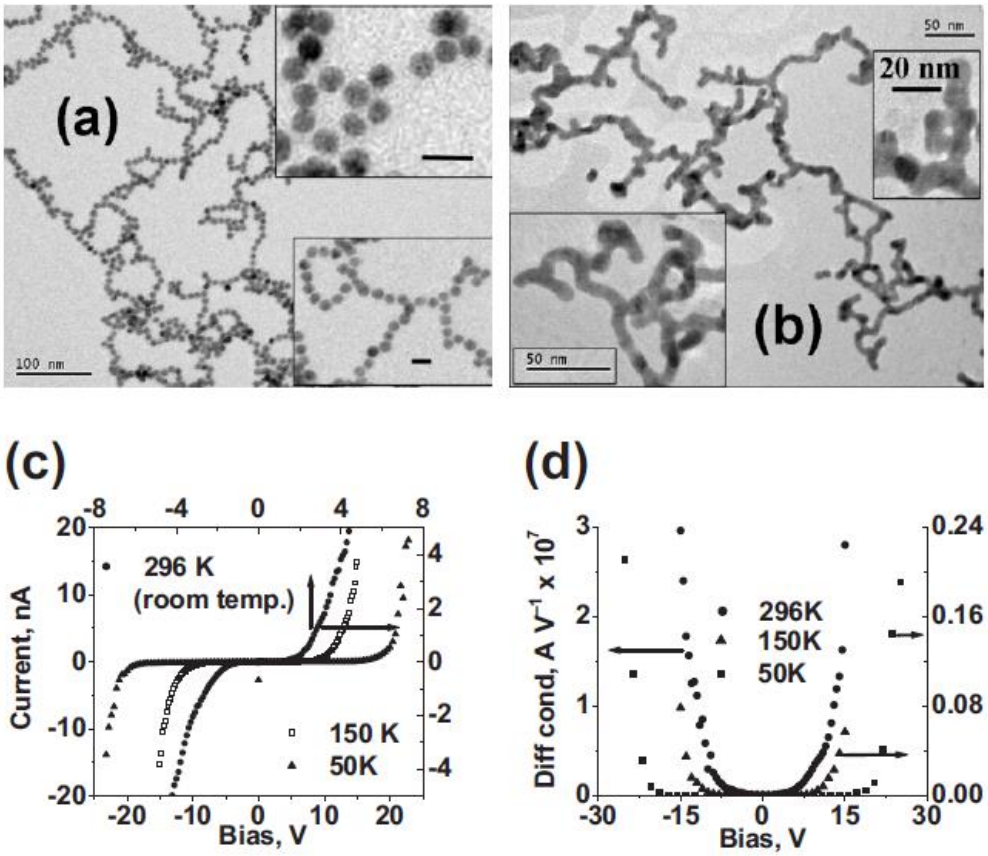

Figure 1.9 – 1-D self assembled branched array of Au NPs and the electronic transports.[64]

In this dissertation, two single-electron devices are described adopting similar strategy. The first device is an electroluminescent 1-D array of Au NPs connected by CdS nano-cement material. The details of this unique material will be presented in depth in Chapter 4. The second device is a ferromagnetic quasi 1-D array of Au NPs linked by Fe_xO_y nano material. Chapter 5 describes this surprising magnetic behavior. The versatility in functionality of this heterogeneous 1-D array of Au NPs is determined by the bridging materials. The ability to fabricate reproducibly such 1-D nanomaterial is a huge advantage in designing novel nanoscale devices.

CHAPTER 2

ULTRASOFT 100 NM THICK ZERO POISSON'S RATIO FILM WITH 60% REVERSIBLE COMPRESSIBILITY

About a 100 nm thick multilayer film of nanoparticles monolayers and polymer layers is shown to behave like cellular-foam with a modulus below 100 KPa. The 1.25 cm radius film adhered to a rigid surface can be compressed reversibly to 60% strain. The more than 4 orders of magnitude lower modulus compared to its constituents is explained by considering local bending in the (nano) cellular structure, similar to cork and wings of beetles. As the rigidity of the polymer backbone is increased in just four monolayers, the modulus of the composite increases by over 70%. Electro-optical map of the strain distribution over the area of compression and increase in modulus with thickness indicates the films have zero Poisson's ratio.

2.1 INTRODUCTION

Squeezing films of most solids, liquids, and granular materials causes dilation in the lateral dimension which is characterized by a positive Poisson's ratio. Auxetic materials,[66] such as, special foams,[67] crumpled graphite,[68] zeolites,[69] spectrin/actin membrane,[70,71] and carbon nanotube laminates shrink,[72] that is, their Poisson's ratio is negative. As a result of Poisson's effect, the force to squeeze an amorphous material, for example, a viscous thin film coating adhered to rigid surface increases by over million fold as the thickness decreases from 10 μm to 100 nm due to constrain on lateral deformations and off-plane relaxation.[73] In contrast, for zero-Poisson's ratio material, the absence of lateral deformation on bending, compressing, or extending, they can be tightly rolled or designed to make soft ultrathin film without any thickness enhancement. Because of a special cellular structure,[74] cork is a near-zero-Poisson's-ratio-material that does not dilate or contract on compression;[75] therefore it can be pressed in a wine bottle with ease to form a seal.[67] Wings of beetles also have near zero Poisson's ratio.[76] No lateral strain during flight allows the wings to morph without (energy expensive) bulging and buckling in other directions.[77] Biomimicked special cellular urethane foams are designed with zero Poisson's ratio to make morphing wings for (future) fuel efficient aircraft.[78] Gas is an ideal zero Poisson's ratio material that easily compresses while constrained in the lateral direction.[66] Thus, a soft, gaslike, solid thin film that can be conformally deposited on surfaces of any shape will be an effective coating for improving damping, cushioning, and traction for gripping. Especially, the soft modulus comparable to tissue (i.e., less than 100 KPa)[79] will have potential applications, for

example, as coating on surgical tools to improve traction to grip delicate tissue samples with high precision for robotics and minimally invasive surgery,[29,80-82] as a surface coating on a complex three-dimensional (3D) scaffold to regulate differentiation of stem cells by regulating the modulus in the 10 to 100 KPa range,[83] as a highly compressible pressure-sensitive dielectric or conductive film for tactile sensing on par with a human finger for surgical and robotic applications,[37,81,84,85] and as soft-cellular-structured porous coating on to 3D scaffold surface for cell proliferation.[86]

2.2 METHODS AND CHARACTERIZATIONS

We demonstrate, ultrasoft, 100 nm films of polymer/nanoparticles composite made by conventional dip coating on solid surface that can be reversibly compressed over 60% strain between rigid plates requiring (very low) stresses below 100 KPa. Using a strategy similar to cellular foams where compressive strain is distributed in the off-plane direction by local bending,[87] we demonstrate a general approach to fabricate nanostructured composite films of modulus in 30 to 100 KPa range. The modulii of individual components of the film, Au and CdS nanoparticles in a polymer matrix, are well above 1 GPa, including the polymer matrix.[88] The 10^4-fold reduction in modulus and gas-like compressibility is explained as local (reversible) bending of the polymer layer as the nanoparticles in adjacent layers interdigitate on compression.

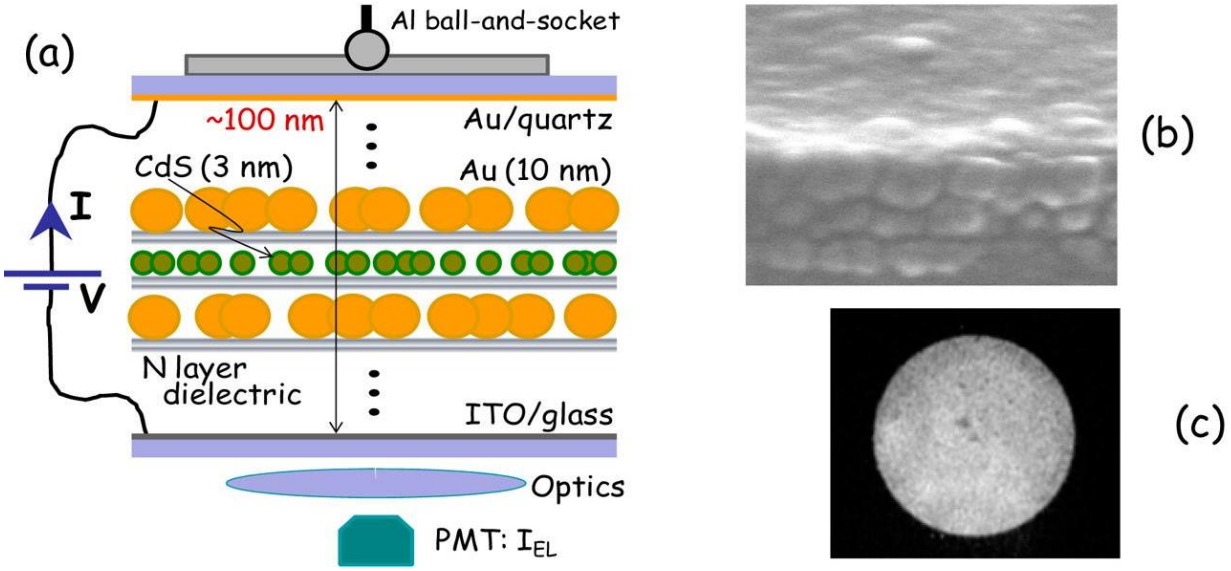

Figure 2.1 - (a) Schematic of electrical characterization of the device showing the load application and optical signal collection on a photomultiplier tube. Films are made with three and two monolayer of Au and CdS particles, respectively. (b) The 140 nm wide SEM image (with no metal deposition) shows the three 10 nm Au particle layers. The CdS particles are too small to visualize. (c) The tactile image of the quartz disk formed on the CCD camera at 40 KPa.

The composite film is made by spin casting alternate layers of poly(allylamine hydrochloride) (PAH) and poly(styrene sulfonate) (PSS) followed by absorbing a monolayer of 10 nm Au or 3 nm CdS particles[89] (Figure 2.1a,b). The molecular weights are 15 000 and 70 000 Da and solution concentrations are 0.1 and 0.2% by weight for PAH and PSS, respectively. The films are deposited on an indium tin oxide (ITO) electrode on glass. The final structure is composed of three layers of Au nanoparticles and two layers of CdS nanoparticles spaced by N layers of PSS and PAH that alternate such that PAH is in contact with the nanoparticles layer or the electrode. Over 60 samples with N ranging from 3 to 21 layers are studied. The average thickness of the PSS/PAH layer, measured by ellipsometry for N = 3 to 21 layer films on Si is 1.12 nm/layer. The estimated thickness of the composite film ranges from 65 to 180 nm. The load is applied by pressing a flat Al platen onto a 12.5 mm radius optically smooth quartz disk coated with 500 nm thick Cr/Au electrode placed on the device. The Al platen is attached to a ball-and-socket joint to ensure uniform force distribution. A bias, V, is applied across the thickness of the film and the current, I, and electroluminescence intensity, I_{EL}, from CdS is recorded concomitantly as a function of applied stress, σ, to quantitatively measure the strain, ε, in the film. The "tactile image" is recorded by focusing the electroluminescent light distribution on CCD camera (instead of PMT tube) (Figure 2.1c). The tactile image is sensitive to local modulation in electron tunneling due to local strain.[37] The uniform light in tactile image, especially closer to the edge compared to the center indicates that the stress distribution is uniform. A uniform stress distribution under no slip condition from center to the edge indicates no Poisson's effect.[73]

As the film is squeezed, the particles come closer and both I and I_{EL} increase. The sensitivity on I−V characteristics of the device to stresses <100 KPa indicates that the modulus of the film is expected to be low (Figure 2.2). In contrast, the current, through a pure polymer film made of 84 layers of PSS/PAH incorporating no nanoparticles, does not exhibit any depend-ence on σ for the same range (Figure 2.3). The (expected) high toughness of pure polymer film on squeezing is typical for a solid thin film due to confinement of in-plane strain. The linear I−V behavior of the film made from just PSS and PAH is due to (ohmic) ionic current, I_N, due to the hygroscopic nature of polyelectrolytes. The ohmic current, $I_N = V/R$, where R is the (ionic) resistance. An order of magnitude higher current and nonlinear I−V behavior in the composite film, compared to pure polymer, is due to electron tunneling between the adjacent nanoparticles along the thickness direction superimposed on I_N. The nonlinear tunneling current, I_T, given by the Fowler− Nordheim equation is $I_T = P \exp(-aK/V)$, where P is proportional to the number of percolating channels, a is the tunneling distance between the particles, and K is a proportionality constant.[37,90,91] As a result, the total current for the composite film is given by $I = V/R + P \exp(-aK/V)$. By differentiating the I−V at fixed σ, the differential conductance, dI/dV, as a function of V is obtained (Figure 2.4). On extrapolating to $V \rightarrow 0$, $[dI/dV]_{V=0} = 1/R$ at various σ is estimated (Figure 2.4 inset). As expected, R deceases monotonically as σ increases. Subsequently, by subtracting the ionic current and fitting a single exponential to V versus $I - V/R$ (= I_T), P and aK are determined. Interestingly, from the I_T characteristics, as the film deforms, the tunneling current increases largely due to P (Figure 2.5) while the interparticle distance remains nominally constant (Figure 2.5 inset). Thus, on deformation, the rise in tunneling current occurs

primarily due to a linear increase in the number of percolation channels as the particles come closer, that is, $I_T \sim P$. Furthermore, the tunneling current is exclusively through the CdS nanoparticles; and electroluminescence only occurs due to transport through CdS, that is, $I_{EL} \sim I_T$. Thus, a linear correspondence between $I_{EL} \sim P$ at all the σ is expected (Figure 2.6).

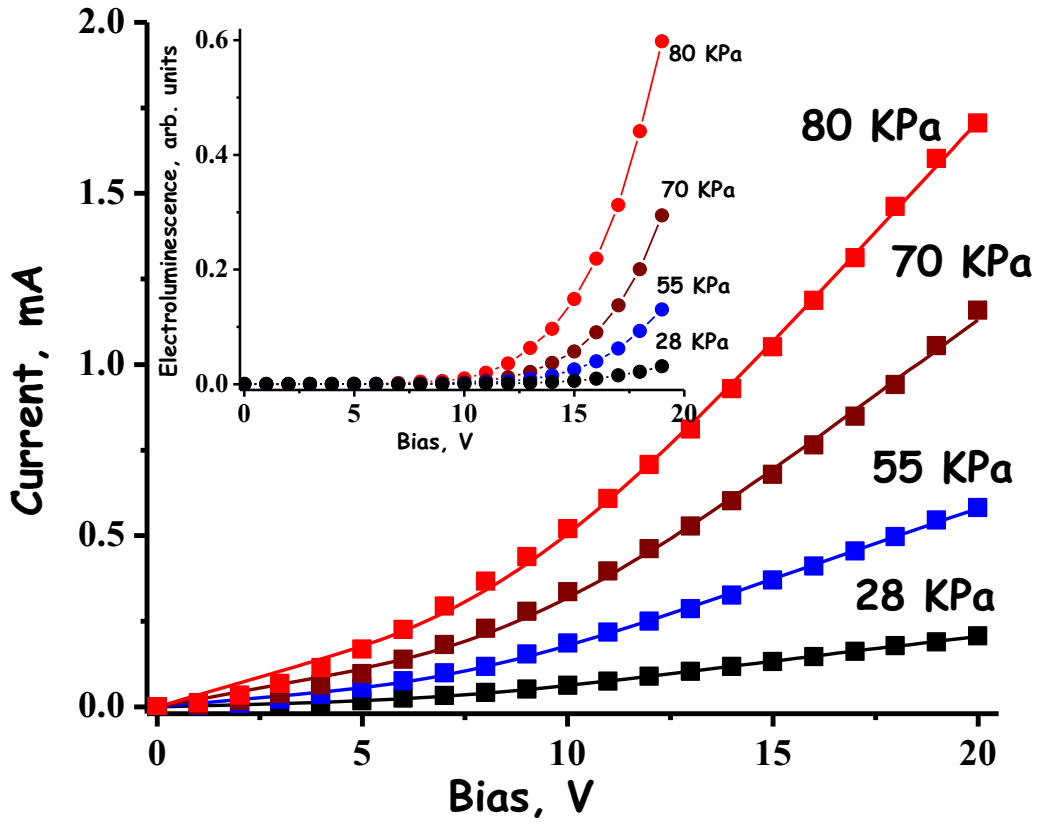

Figure 2.2 - Electrical response of the film on uniaxial compression. A typical change in I–V response at different applied stress (N = 13). The line is a fit to the tunneling and ionic current model. Inset: Corresponding I_{EL} measured concomitantly with the I–V characterization.

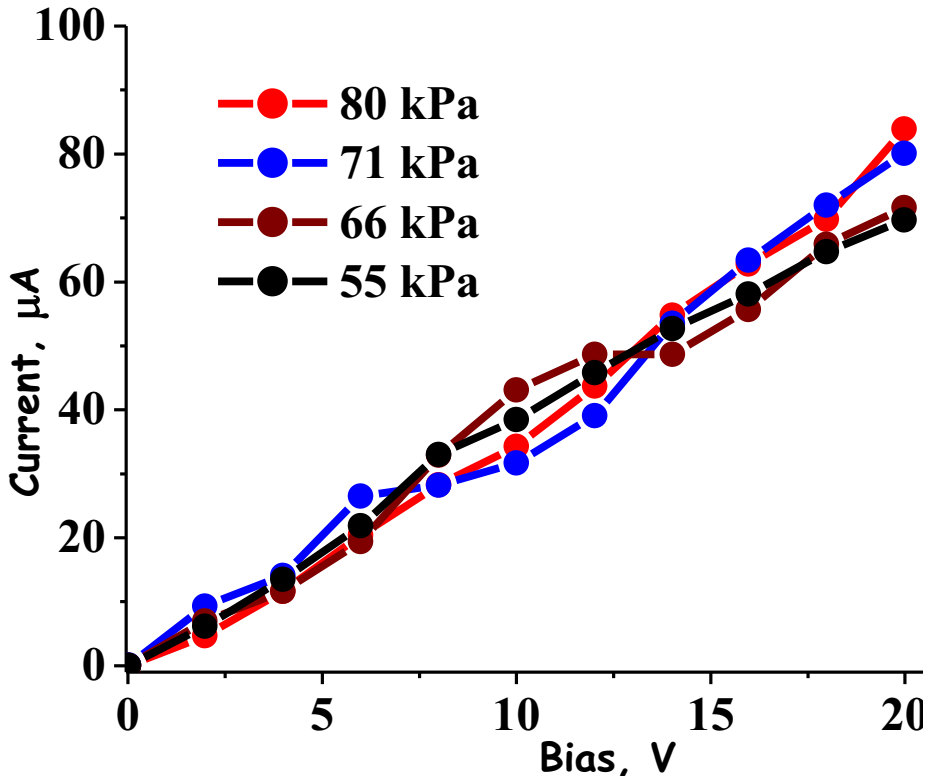

Figure 2.3 - The I–V curve does not change for PSS/PAH film (N = 84 with no NPs).

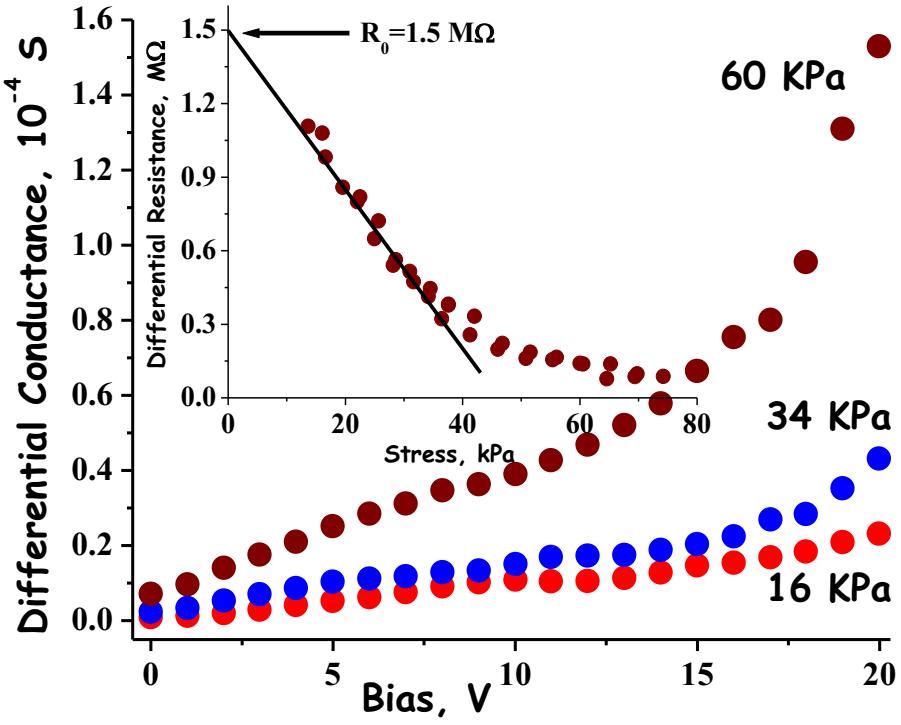

Fig 2.4 - Typical effect of stress on dI/dV versus V behavior (N = 5).

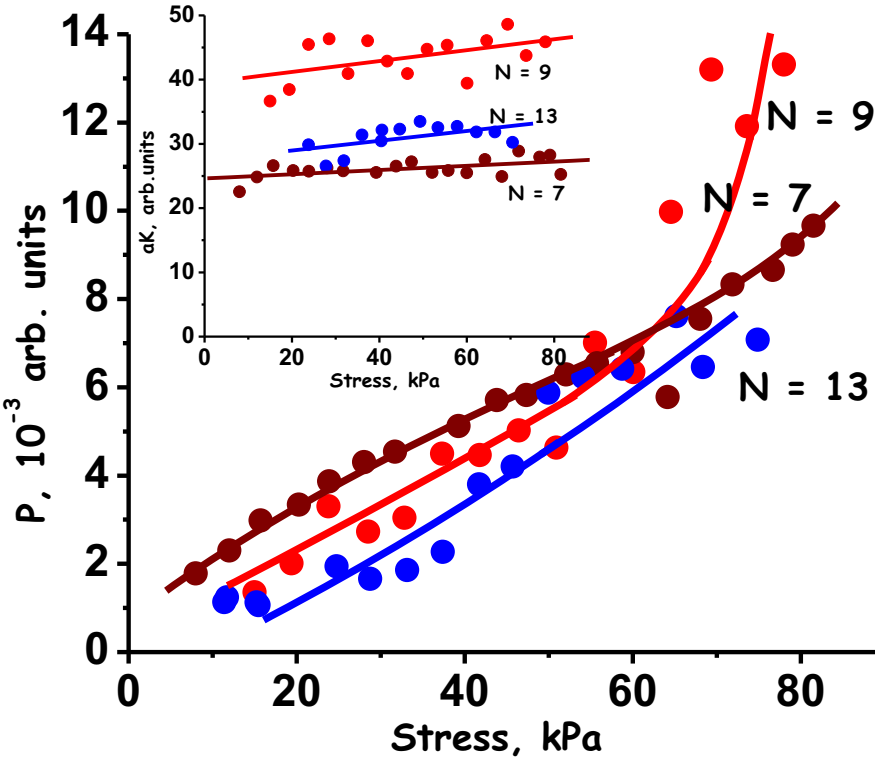

Fig 2.5 - Typical behavior of tunneling parameters, P and aK, as a function of stress for three films. Each data point is based on an I–V curve at fixed σ.

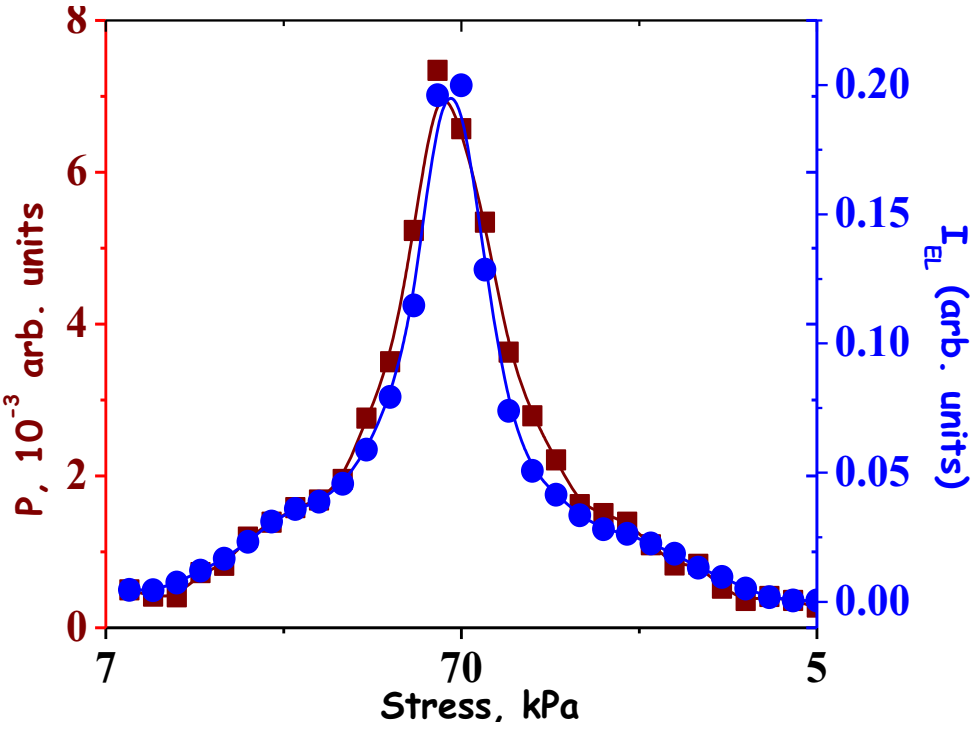

Fig 2.6 - Typical correspondence between P and I_{EL} (N = 5).

The compressive strain in the film is estimated from R. The ionic resistance is given by $R = \rho L/A$, where ρ is the resistivity, L is the film thickness, and A is the "effective" cross-sectional area for ion transport along the thickness of the film. The resistivity, $\rho \sim 1/c$, where c is a concentration of mobile ions, that is, charge density. Assuming the number of ions does not change on compression (i.e., the lateral strain is negligible), $c \sim 1/AL$. Thus, $R \sim (1/AL)^{-1}(L/A)$, or $R \sim L^2$. Important to note is that even though A may change on deformation due to a more constricted path for ion conduction as particles come closer, the scaling $R \sim L^2$ is still valid. Considering affine deformation, the strain in the film is given by $\varepsilon_{aff} = (R_O^{0.5} - R^{0.5})/R_O^{0.5}$, where R_O is obtained by extrapolating the ionic resistance to $\sigma = 0$ (Figure 2.4 inset). A typical stress−strain curve shows two distinct regimes: at low stress, the deformation is linear with low modulus and, subsequently, the strain tends to flatten leading to a higher modulus similar to the densification observed in foams[87] (Figure 2.7, 2.8, 2.12, 2.13, 2.14, 2.15, 2.16, 2.17). Typical stress-strain curves for other values of N studied among more than 60 films tested are shown in Figure 2.12, 2.13, 2.14, 2.15, 2.16, 2.17. The data at low stress−strain is difficult due to the small forces involved. Although a low friction universal joint is used to ensure flat contact, a small force is needed to "settle" the parallelism between the film and the Al platen before deformation of the film commences. On the basis of the data obtained for the low stress linear regime, the strains are 35 to 60% for all of the samples tested. Similar to conventional foams, at high strains the actual strain may be smaller than ε_{aff} in the densification region.[87]

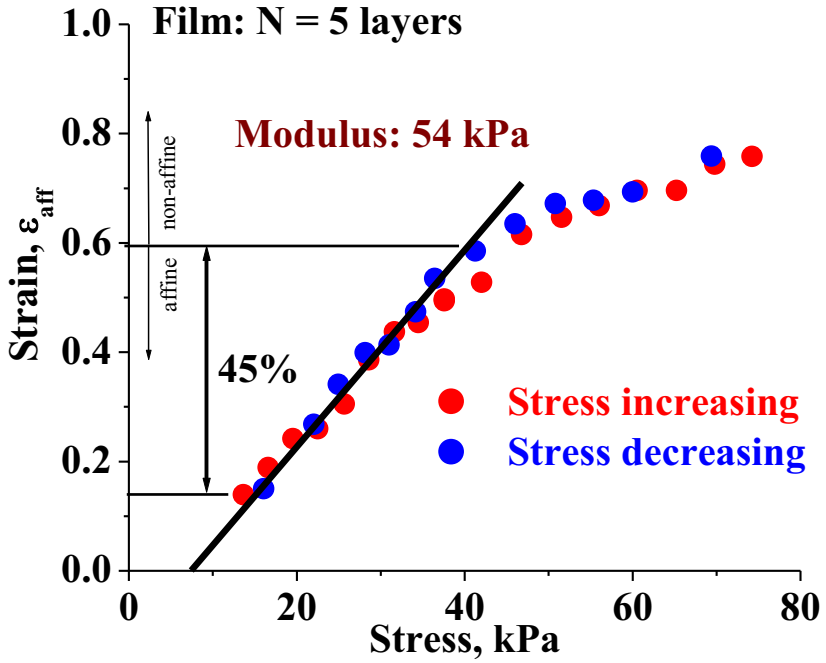

Figure 2.7 - Typical mechanical behavior of two films calculated from ionic resistance exhibiting the reversible deformation to high compressive strains for N = 5.

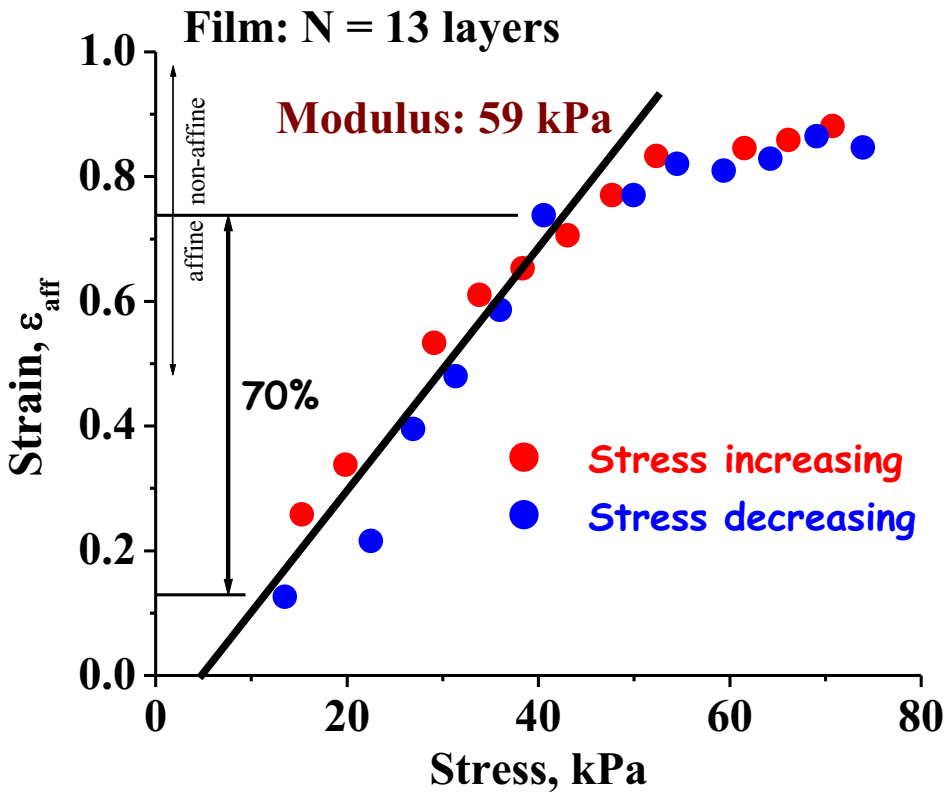

Figure 2.8 - Typical mechanical behavior of two films calculated from ionic resistance exhibiting the reversible deformation to high compressive strains for N = 13.

The large reversible strain with low modulus of the composite films is qualitatively explained in terms of a simple model (Figure 2.9a). Owing to large particle density,[37] highly stratified, parallel layers of Au nanoparticles are formed (Figure 2.1 scanning electron microscope (SEM) image). The non-conformal coating of the polymer on high density Au particle coverage leads to interparticle voids (Figure 2.9a). Voids in the interstitial regions have been inferred from x-reflectivity measurements on similar multilayer structure incorporating nanoparticle.[92] As the film is compressed, the larger Au nanoparticle will bend or squeeze the polymer layer containing the smaller CdS

particles. The schematic, nominally to scale for N = 7 that will have a nominal thickness of ~ 7 nm for the PSS/ PAH layers, shows ε of ~ 40% by local bending and squeezing of the polymer layer. As the tunneling current is exponentially sensitive to interparticle distance, which does not change significantly (Figure 2.5 inset), the primary mode of deformation is by bending and not squeezing. The reversibility also suggests that the film does not rupture during buckling. The deformation of the cellular structure in Figure 2.9a is similar to cork[75] where the schematically marked nodes of the cell correspond to the location of the Au nanoparticles (Figure 2.9b). Consistent with the bending, as the interposer layer gets thicker, the film becomes stiffer leading to higher modulus (Figure 2.10) even though the amount of polymer relative to the nanoparticles increases. Conventionally, due to Poisson's effect, the lateral strain on compression is relieved more effectively as thickness increases leading to lower stiffness. A reverse effect is observed in films studied; the stiffness increases monotonically with thickness in the range studied (Figure 2.10 inset). This implies that the strain in the lateral direction is insignificant or zero; in other words, the Poisson's ratio is close to zero.

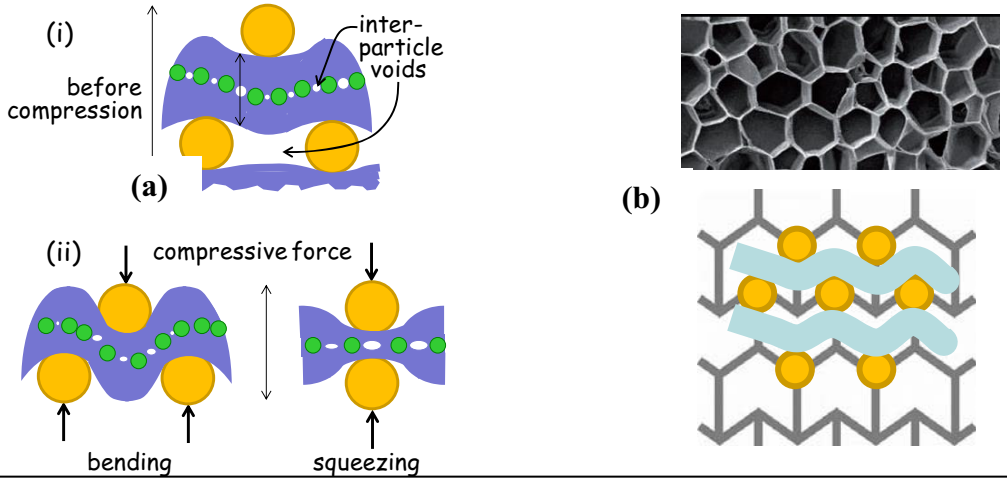

Figure 2.9 - (a) The two local deformation modes on compression are bending and squeezing of the dielectric layer. The relative dimensions of the schematic are nominally to scale depicting a strain of about 40% in N = 7 film. (b) The electron microscope image of the cellular structure of cork. Reproduced with permission from ref 73. Copyright 2005 Maney Publishing. Idealized model with an overlay of the nanoparticle/polymer layered structure. The width of the image is 350 μm. Reproduced with permission from ref 74. Copyright 2010 John Wiley and Sons.

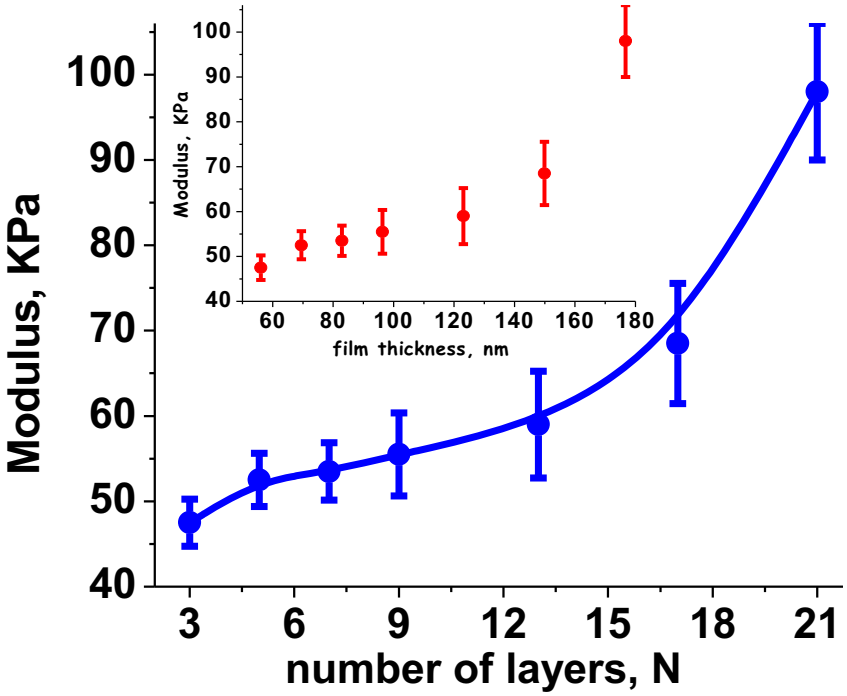

Figure 2.10 - Effect of N on the modulus of the film based on initial linear region (Figure 2.7, 2.8) averaged over 60 samples.

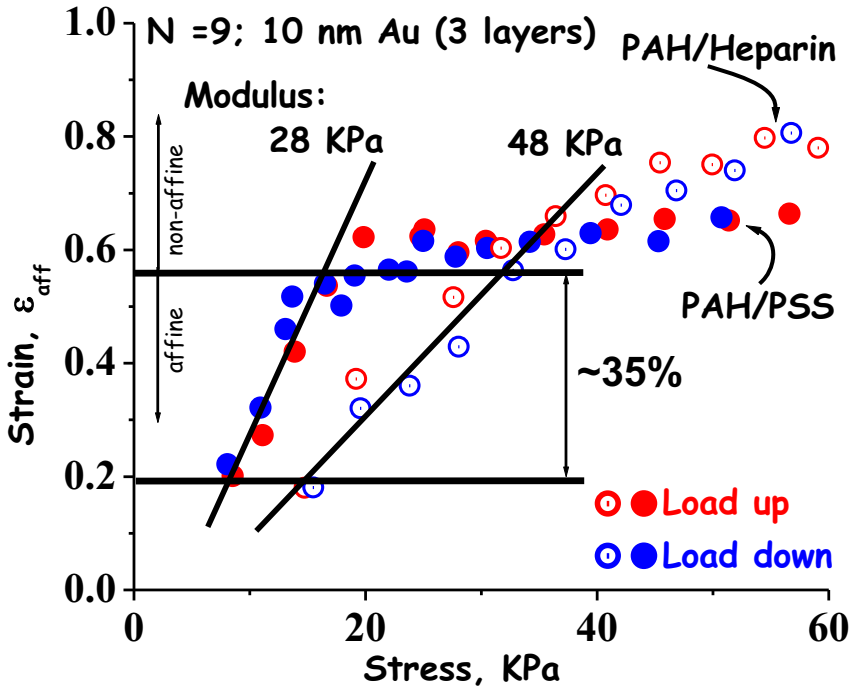

Figure 2.11 - The effect of stiffness of the polymer layer on the modulus of the film made from three layers of 10 nm Au particle monolayer with no CdS particles.

To further evaluate the validity of the bending model, the stiffness of the interposer layer is significantly reduced by eliminating CdS particles. As expected, the modulus is lowered compared to CdS-containing film (Figure 2.11). Furthermore, the plateau occurs at a lower stress level indicating that the pure polymer interposer layer is easier to bend at lower stress levels (Figure 2.11). Conversely, consistent with the bending model, replacing the flexible PSS polymer with a more rigid electrolyte, heparin, the modulus is enhanced 2-fold. Furthermore, the modulus can be reduced by increasing the Au particle size to incorporate larger voids. For example, for N = 9, the modulus is reduced from ~ 55 to ~ 30 KPa as Au particle size increases from 10 to 15 nm (Figure 2.17).

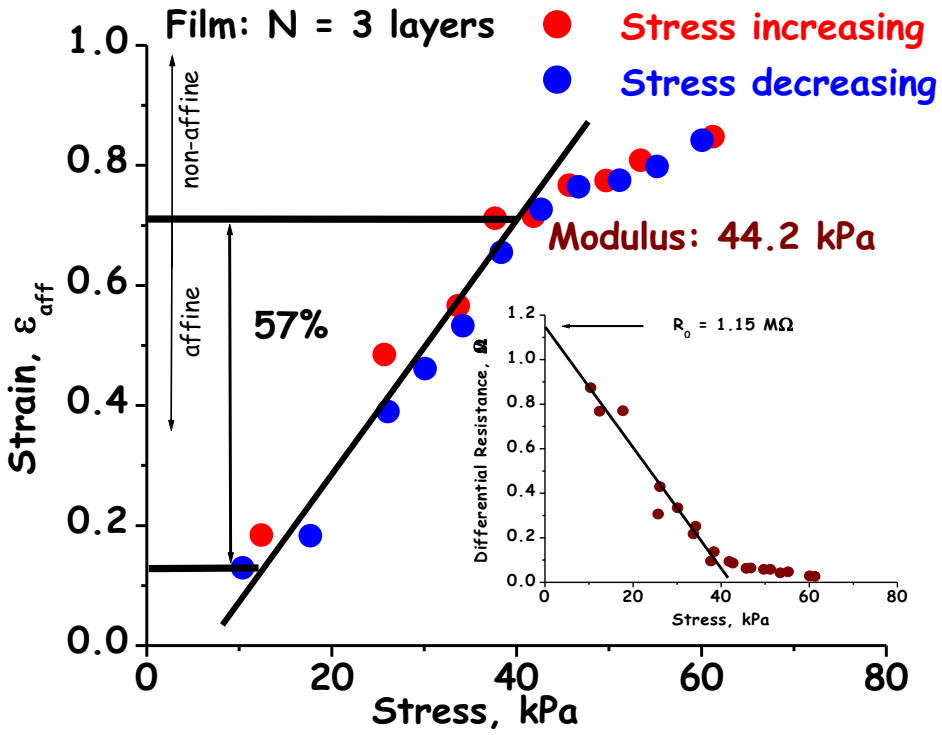

Figure 2.12 - Typical stress – strain curve for N = 3.

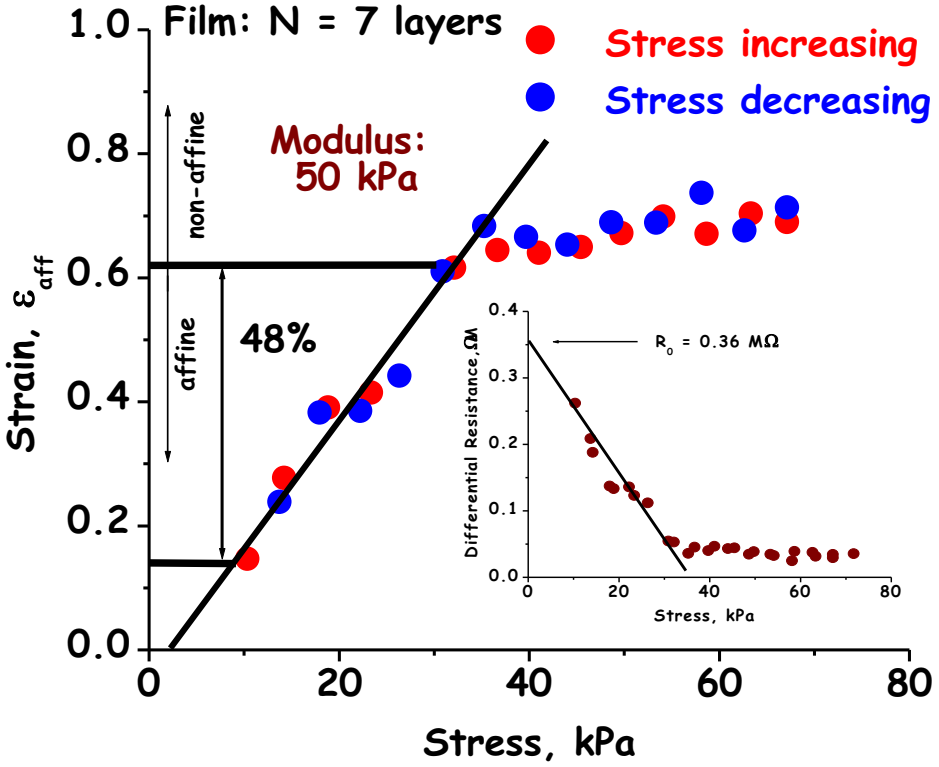

Figure 2.13 – Typical stress – strain curve for N = 7.

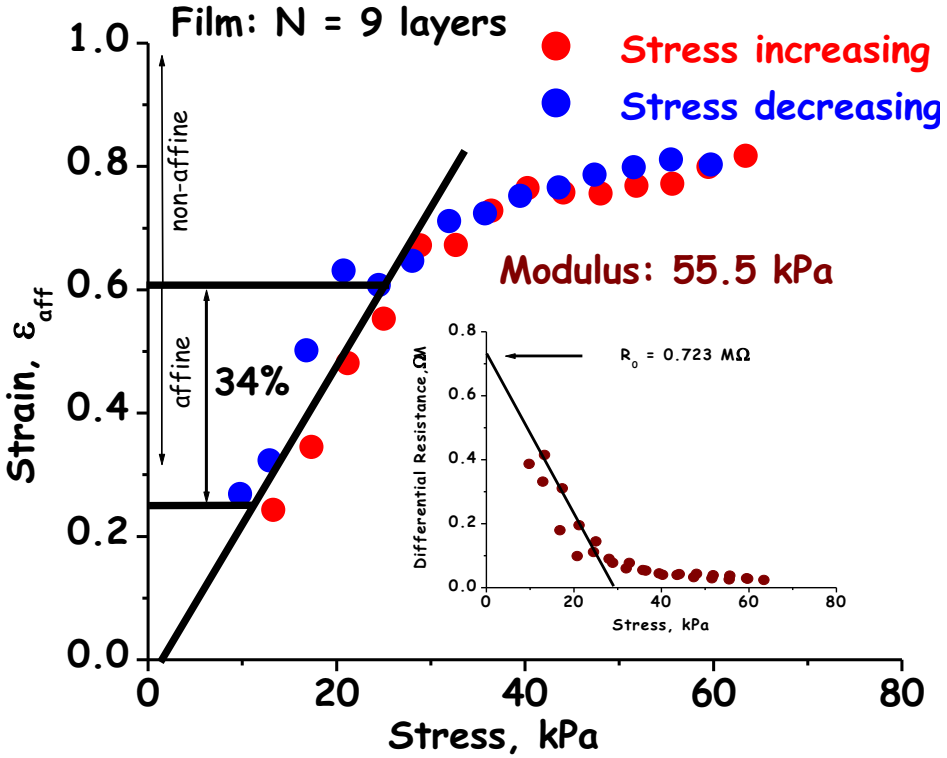

Figure 2.14 – Typical stress – strain curve for N = 9.

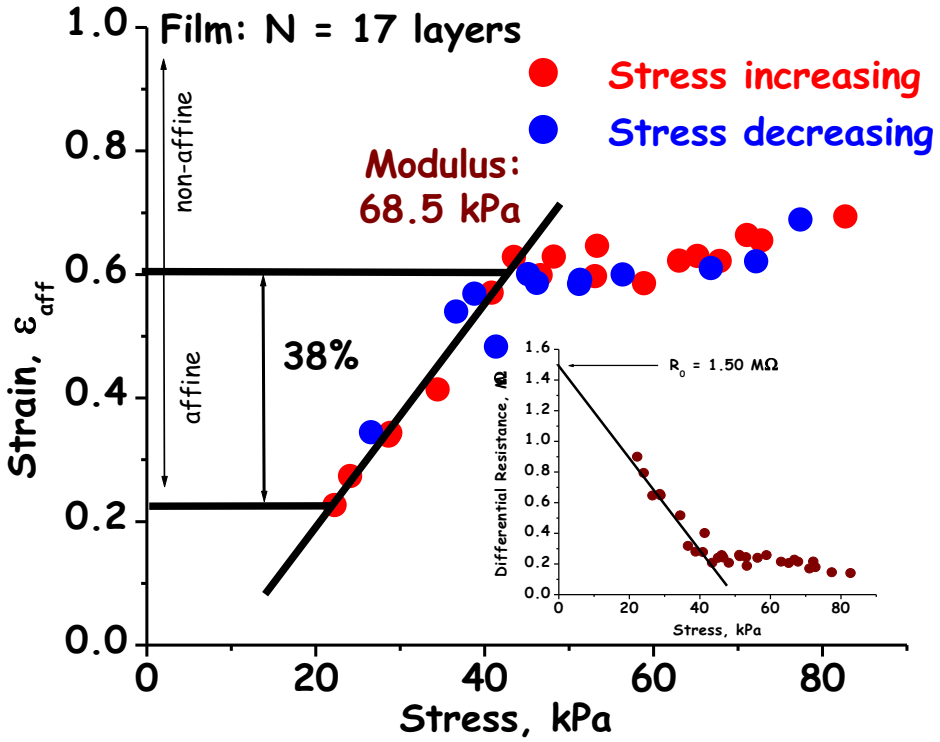

Figure 2.15 – Typical stress – strain curve for N = 17.

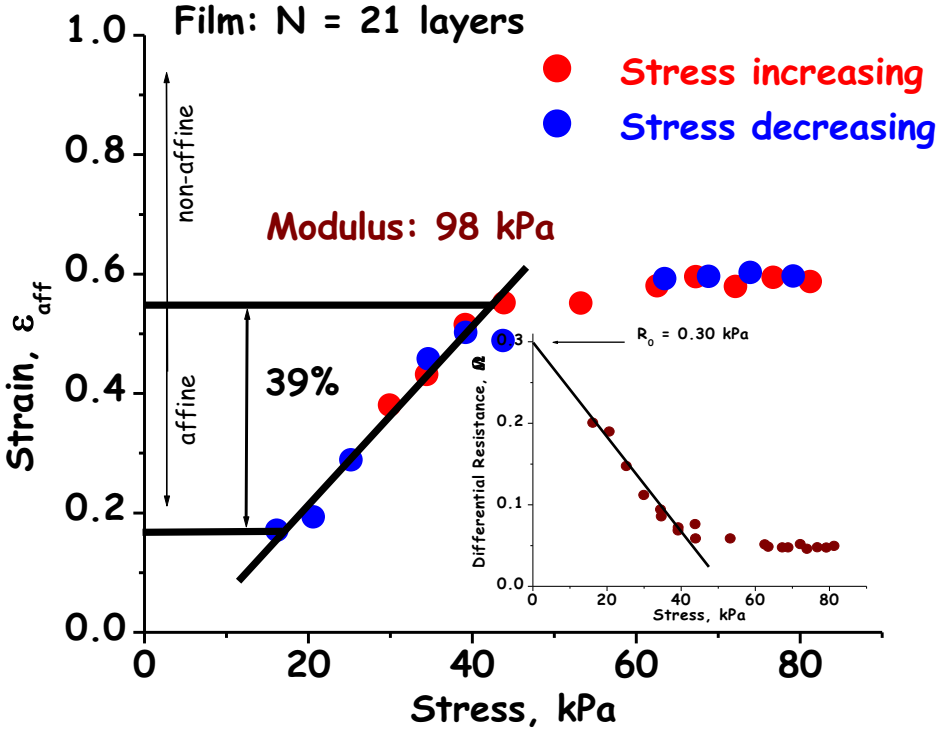

Figure 2.16 – Typical stress – strain curve for N = 21.

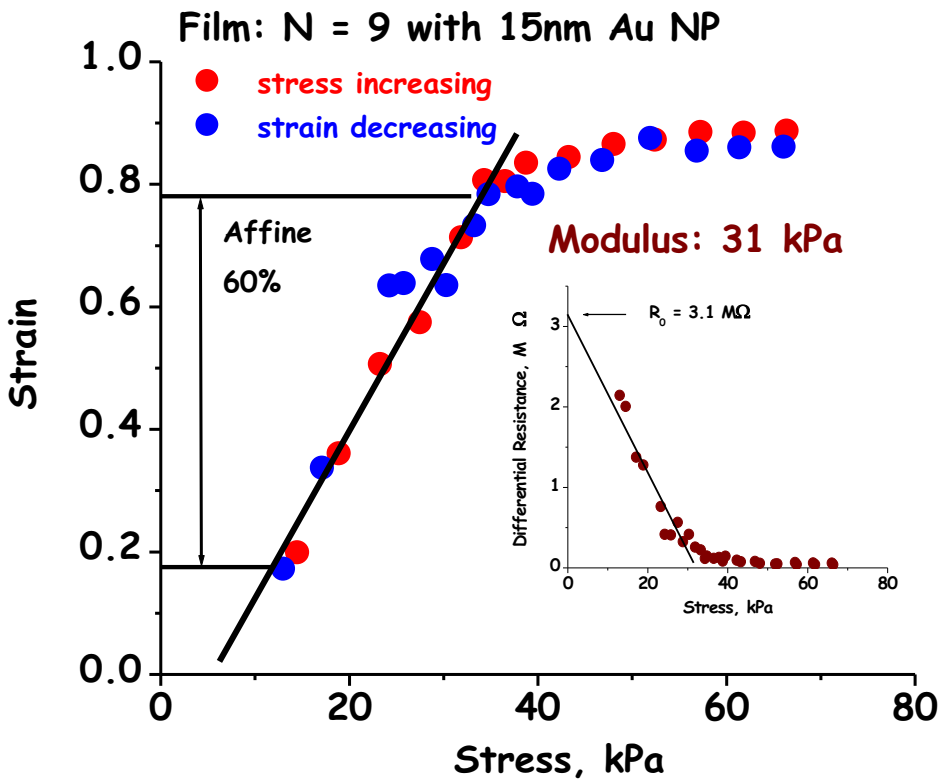

Figure 2.17 – Stress-strain curve for three monolayers of 15 nm Au particle and two monolayers of 3 nm CdS particles.

2.3 GRAPHENE OXIDE – NANOPARTICLE COMPOSITE FILM

Graphene is a single atom thick two-dimensional (2 – D) honeycomb sheet in which sp^2 bonded carbon atoms are arranged in honeycomb lattices, whereas graphite is a three-dimensional stack of graphene sheets. Yet these single sheets of graphene have been estimated to be the hardest material known to man with a modulus of approximately 1TPa and intrinsic strength of 130 GPa.[93] Charge carrier mobility in graphene has been experimentally achieved in excess of $2x10^5$ $cm^2 V^{-1}s^{-1}$ at electron densities of ~ 2 x 10^{11} cm^{-3} [94] which is 200 times higher than that of Silicon.. Light, yet strong and high conductivity are the gravitational features of graphene that have sparked a research "boom" on graphene and many of its derivatives: graphene oxide, carbon nanotube, and fullerene in the last decade. Its high optical transmission of more than 97% at room temperature[95] and atomic impermeability[96] make it an ideal candidate for transparent electronics and membrane material. One of the key challenges in graphene is lack of an appreciable band gap (> 1eV), a key requirement in semiconductor technology. However theoretical calculation predicts mechanical strain of ~12% can cause large band gap opening in graphene.[97] In this section a 2 – D sandwich structure of graphene sheets between gold (Au) nanoparticles (NPs) monolayer will be studied to apply well-controlled strain (over 10%) to graphene.

In Section 2.2, polyelectrolyte – nanoparticle composite films were shown to possess unique mechanical properties such as ultralow modulus, high compressibility over 60%. In this section we extended our studies to a film that contained graphene oxide. The central principle is to replace the polymer layer between the Au NPs layers with graphene oxides sheets (Fig. 2.18).

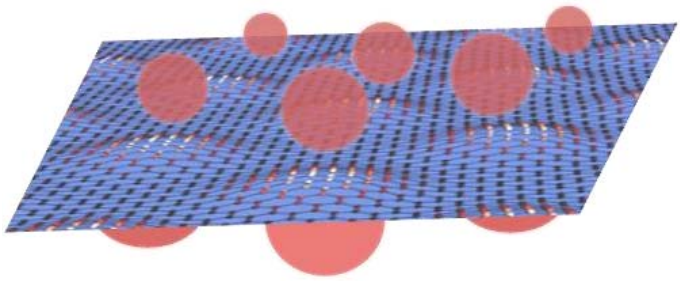

Figure 2.18 – Schematic of the graphene oxide – NPs composite structure. The reddish spherical balls are Au NPs, while the blue sheet is graphene oxide.

When an external stress is applied the graphene oxide layer (sandwiched in between 2 Au NPs layers) will be bent to extremely high strain (over 40%). In this particular study we prepared a film with a total of 3 layers of Au NPs and 2 graphene oxide layers between them. Graphene oxide (Fig. 2.19) was deposited in a polymer matrix of seven layers of PAH – PSS.

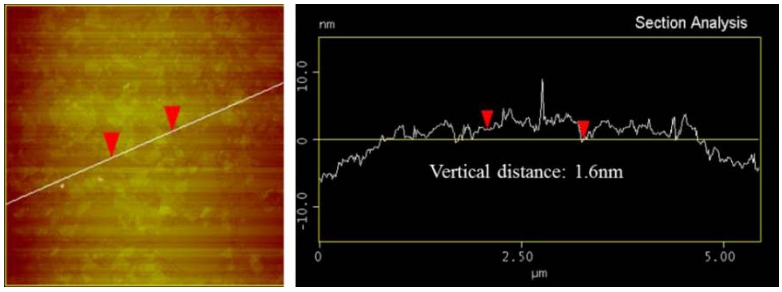

Figure 2.19 - AFM image of the dip – coated graphene oxide on a SiO_2/Si substrate modified with PAH. The obtained data shows an average thickness of 1.6nm, an equivalence of ~ 4 – 5 monolayers. The film appears continuous throughout the surface. The AFM image is 5µm x 5µm.

We found that the film with graphene oxide behaves similarly compared to a film without graphene oxide, meaning it is ultra – soft. Figure 2.20 shows the stress – strain behavior of the film containing graphene oxide. From the linear region a Young's modulus of 51 kPa is computed, which is ultra – soft compared to ~ 1 – 10 GPa of thin PAH/PSS film or particles. Although enforced with graphene oxide, the nano device is

still ultra – soft, suggesting occurrence of buckling phenomenon or bending of graphene oxide sheets.

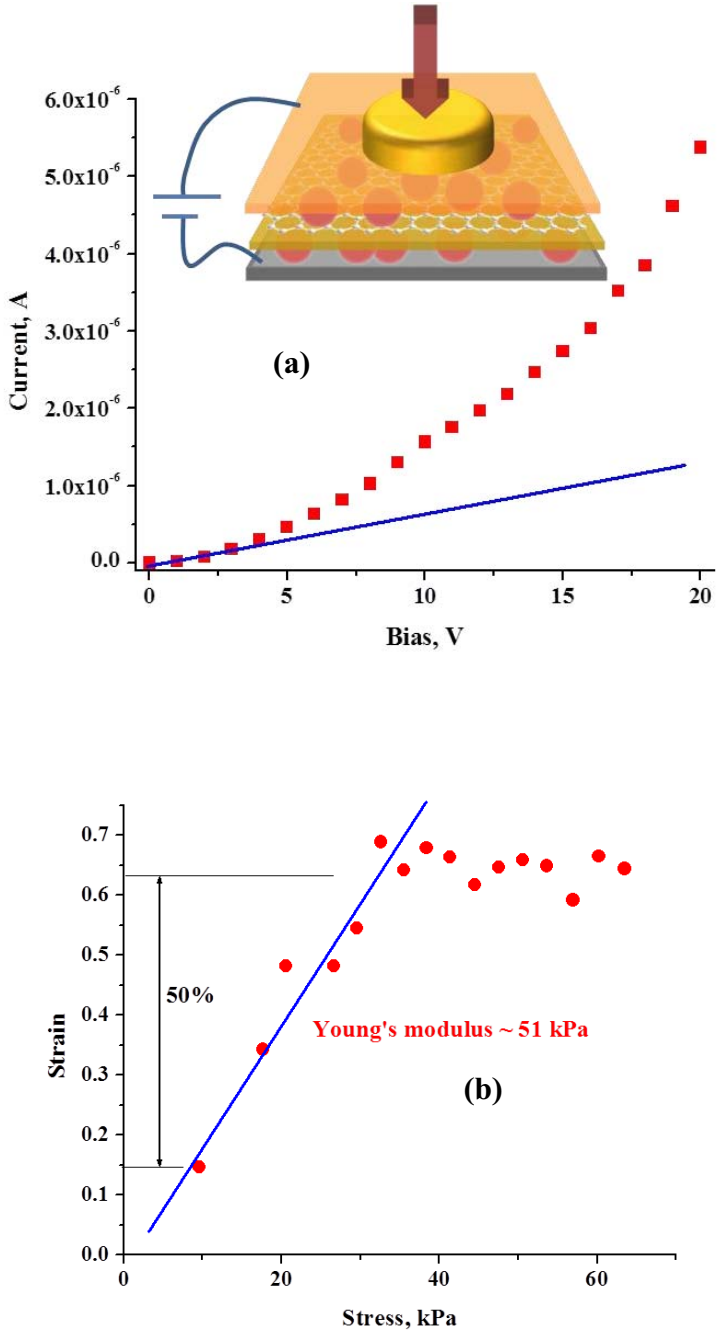

Figure 2.20 – Electrical and mechanical properties of the graphene oxide device. (a) I – V measurement of the device shows a non-linear relationship. Bias was applied across the top and bottom Au NPs layers. (b) Mechanical strain as a function of stress is shown.

2.4 SUMMARY

In summary, a ~ 100 nm thick layered film of polymer and nanoparticle monolayers is self-assembled to impart gaslike compressibility with a modulus of 50 to 100 KPa that is comparable to tissue. The compression modulus of the film is 4 orders of magnitude lower than its individual constituents. The low modulus and large reversible compressibility up to 60% strain is explained by local bending of the polymer layer. The modulus of the composite film increases with film thickness. The measurements on the mechanics of the film indicate that the Poisson's ratio is zero. The films can be self-assembled by sequential dip coating process to form a soft, foam-like coating for applications, such as improving traction to grip delicate tissues by surgical tools, sensitive tactile devices, and coatings on scaffolds for stem cell differentiation. To our knowledge, this is the first demonstration of thin films of thickness in nanometer scale that exhibit zero Poisson's ratio. The approach can be generalized to micrometer to centimeter scale by using larger particles and inter particle layering material.

CHAPTER 3

TACTILE IMAGING OF IMBEDDED PALPABLE STRUCTURE AT SENSITIVITY AND RESOLUTION OF HUMAN FINGER

Apart from texture, human finger can sense palpation. The detection of imbedded structure depends on the relative stiffness of the matrix, the object, and the device. If the device is too soft, its high responsiveness will limit the depth to which the imbedded structure can be detected. The sensation of palpation is an effective procedure for physician to examine irregularities. In Clinical Breast Examination (CBE), by pressing over 1 cm^2 area, at contact pressure in 70-90 kPa range, the physician feels cancerous lumps that are 8-18-fold stiffer than surrounding tissue. Early detection of lump in 5-10 mm range leads to an excellent prognosis. We describe a thin-film tactile device to emulate the human-touch to quantify CBE by imaging size and shape of 5-10 mm objects at 20 mm depth in a breast model using ~80 kPa pressure. The linear response of the device allows quantification where the grey scale corresponds to the relative local stiffness. The (background) signal from < 2.5-fold stiffer objects of size below 2 mm is minimal.

3.1 INTRODUCTION

With an estimate of almost 300,000 new cases diagnosed in 2013, accounting for 29% of all cancers, breast cancer is the most common type of cancer among women.[98] Similar to other type of cancers, an abnormal mass (or a lump) developed in the breast either benign (in situ) or cancerous (invasive) grows in size with time, eventually spreads out to neighboring regions. While there is no cure today, early diagnosis when the lump is less than 10 mm can improve the survival rate to more than 94%.[98] Using x-ray radiation, mammography images the lump based on (< 50%) density contrast between the lump and surrounding tissue which is not an effective approach for young women or women with dense and vascular breast.[99] Medical imaging tools such as MRI, ultrasound are more sensitive than mammography but too expensive for a screening tool. Palpability is more effective parameter to detect malignancy, especially in younger women.[100] Higher palpability of the lump has higher probability of being malignant irrespective of size.[101] Typically, the malignant lump is 8-18 folds stiffer than surrounding tissue.[27] Clinical breast examination (CBE) is a recommended complementary tool to mammography that measures palpability.[102] CBE is an inexpensive, radiation free procedure that can be performed in the doctor's office where a professional manually feel the patient's breast for lumps.[25] However, the result is qualitative with no tangible record-keeping[25] and typical size detected is above 21 mm.[26]

The rapid development of thin-film tactile devices in the recent years, also called "electronic skin", spurred by a variety of applications, such as robotics, minimally invasive surgery, haptics, prosthetics…,[34,38-40] has a natural extension to quantitatively image palpability by touch.[103] The contact pressure corresponding to the texture and/or

shape of the object is mapped by measuring the local deformation of the tactile-device film to form a continuous or pixelated image. Typically, the local deformation is measured by probing the modulation in conductivity of a granular composite,[45,46,56] capacitance,[42-44] piezoresistance,[45-48] or refractive index.[49,50] Sensitivity to touch of less than 1Pa has been demonstrated.[104] Resolution of 20 μm has been achieved for contact area of 1cm^2.[37] To image palpable features in the breast, a key required characteristic is to emulate the human touch with optimum sensitivity in pressure range of 50-90 kPa over a contact area in excess of 1 cm^2. Higher sensitivity would saturate the image preventing visualization of deeper imbedded mass and will have large background from the natural heterogeneities. While lower sensitivity would require large applied pressure, leading to discomfort. Recently there are several tactile device reported to image breast cancer lumps. SureTouch, a commercial product can image 22-fold stiffer mass with 6mm and 11mm diameter at a depth of 17mm and 27mm, respectively.[103] Based on piezoresistivity,[55] piezoelectricity,[56] vibration[57] and IR pressure sensor[58] masses as small as 10 mm diameter up to 20 mm in depth with a stiffness contrast 5-8 folds larger than surrounding has been detected.[58] However, the resolution is only in 2.8 mm range making the image quality poor to determine the shape of the lump. The shape, especially the irregularities is a critical feature, for example to detect palpability at the skin level to diagnose other cancers such as, melanoma.[105]

Here we describe a tactile device to quantitatively image 5-10 fold stiffer object imbedded as much as 20 mm deep in a softer matrix. The emitted light is linearly proportional to local stress. The tactile device is a multilayer composite thin film consisting of nanoparticles (NPs) and polymers. The film is an analog electro-optical

device where the imbedded stiffness is imaged as continuous variation in light emission that can be focused directly on a camera. The electro-mechanical characteristics of the flexible thin film is precisely tuned to obtain tactile image of the palpable structure for contact pressure in 30 to 90 kPa range, similar to human touch. About 5 mm stiff features embedded 20 mm deep in an artificial breast model are imaged to demonstrate the performance of the device. Features softer than 2.5 fold relative to the surrounding do not produce significant background. The image has sufficient resolution to determine both the size and shape of the mass.

3.2 METHODS AND MATERIALS

The tactile sensor is fabricated by interposing three monolayers of Au (10 nm) and two monolayer of CdS (3 nm) spaced by dielectric polymer film (DPF). The polymer film is made by spin-coating at 3000 rpm in 20 seconds alternate layers of PAH and PSS, and spin-washing with DI H_2O also at 3000 rpm in 20s in between . Thus the tactile sensor has the following tandem structure: ITO-DPF-(Au-DPF-CdS-DPF)$_2$-Au-DPF. The top layer is DPF for protective purpose. The structure and process is described in more details in the literature.[106] The device is deposited on 25 x 25 mm^2 ITO glass (Delta Technologies Limited, CB-90IN-0105). PAH (15,000 Da) and PSS (70,000 Da) were purchased from Sigma-Aldrich.

The palpable structures are designed in a matrix of extra-soft cellular silicone (Rogers Corporation, BF-1000 in 1.5mm, 3.2mm, and 6.5mm thicknesses). The filler was closed cell silicone sponge of (Rogers Corporation) and/or silicone rubber sheet (McMaster-Carr, 8632K44). The sponge is 2.5 and 5 folds stiffer than matrix and the silicone rubber is 10 folds stiffer than matrix. Their mechanical properties are investigated with a tensile test instrument (TestResources; Model 225LB Actuator and Model 3397-136 Load Cell). The results on mechanical properties can be found in Fig 3.1.

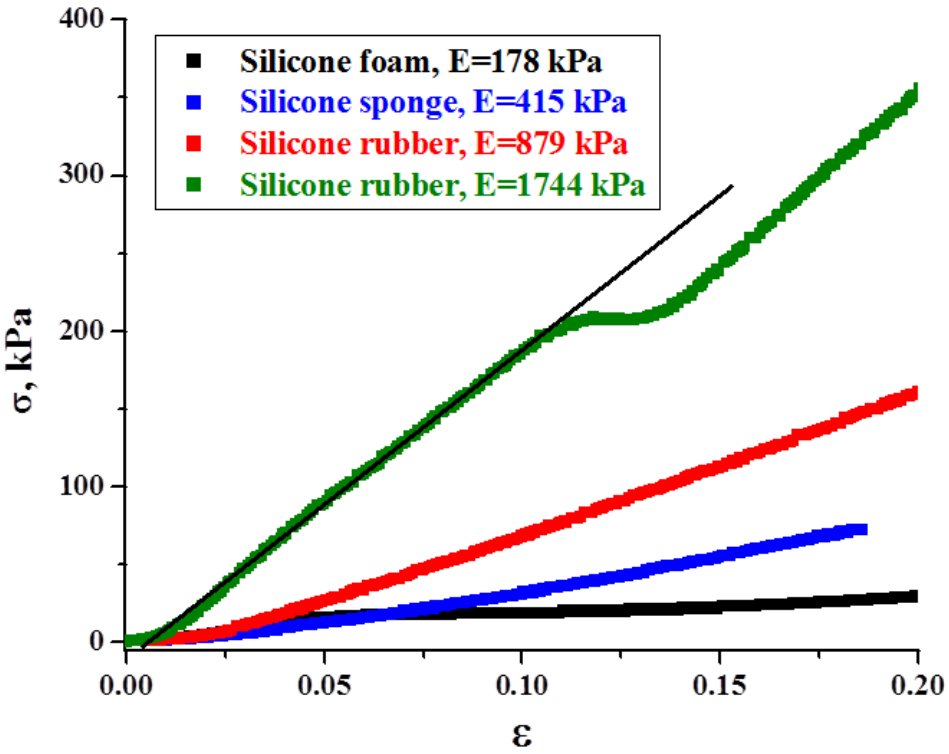

Figure 3.1 – Stress–strain measurements of silicone materials used to construct palpable structures.

The breast model was provided by MammaCare (Health Program Opaque Breast Model). This model is widely used in various training programs and "tactually accurate to teach the difference between the feel of normal, nodular breast tissue and the feel of small lesions (www.mammacare.com).

3.3 RESULTS AND DISCUSSION

The tactile device is a fabricated layer-by-layer spin-coating of two polyelectrolytes: poly(allylamine hydrochloride) (PAH) and poly(styrene sulfonate) (PSS); and deposition of 10nm Au and 3nm CdS NPs.[106] The overall multilayer structure was a total of 3 and 2 layers of Au and CdS NPs deposited alternatively and separated by 9 layers of PAH and PSS. The device was deposited on a 25x25 mm^2 ITO glass substrate. The active area of the device is 500mm^2. The ITO served as the bottom electrode. The top electrode was a smooth Aluminum foil. The top surface of the device was protected with an additional PAH-PSS bilayer. The overall thickness of the thin film device was ~ 150nm.

To quantitatively study the performance of the device for imaging palpability, composite structure was fabricated with a soft Silicone foam matrix of modulus, E_M ~ 178 kPa imbedded with a stiffer filler (of fixed thickness, 3 mm). The filler was a combination of Silicone sponge (E_T ~ 415 kPa), and two types of silicone rubbers (E_T ~ 879 and 1744 kPa). The details of the materials are in the Methods section. Depending on the filler materials, the stiffness ratio, E_T/E_M ranged from 2.5 to 10. In a typical imaging experiment, the composite structure is placed above the device and a constant load of 80 kPa is applied (Fig. 3.2). The lateral dimension of the filler, L and the depth from the contact, d were varied (as described later). On pressing against the tactile device, the pressure distribution is uneven corresponding to modulation in the local stiffness relative to the surrounding matrix. The device is like an electro-optical "strain gauge" that converts the compressive stress to electroluminescence intensity (I_{EL}) from

the CdS nanoparticles. The tactile image is obtained by focusing the distribution of emitted I_{EL} on a CCD camera (Roper Cascade II).

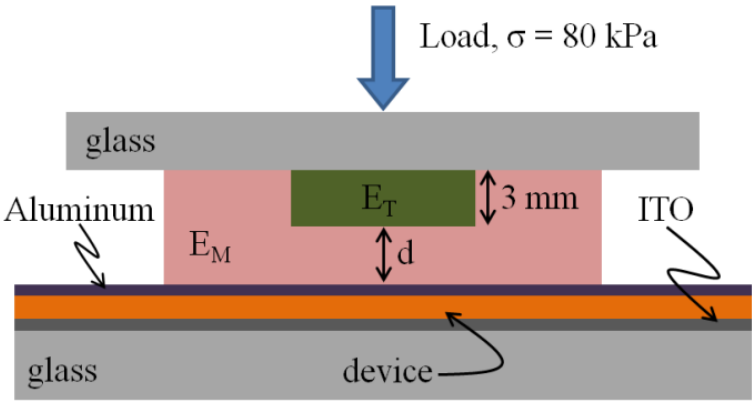

Figure 3.2 – Schematic of touch experiment of palpable structure. A touch pressure applied on the top through a glass slide, compressed the palpable structure on the tactile device. Bias was supplied across the top (Al) and bottom electrodes (ITO). The pressure was fixed at 80 kPa. Bias was constant at 18V.

The device principle is similar to compression sensitive elastomer used in electronic skin except, the thickness is only ~150 nm with reversible stress-strain response over 40% compression and linearity up to 60% (Fig. 3.3). The mechanical properties of the tactile device is obtained by applying uniform compressive stress, σ, on the film at constant bias, and measuring the change in resistance to calculate the strain as, $\varepsilon = (R_O^{0.5} - R^{0.5})/R_O^{0.5}$, where R_O is the resistance at $\varepsilon = 0$.[106] The σ - ε characteristics indicate that the device film deforms linearly at a modulus of 55.5 kPa (Fig 3.3). The low modulus and high compressibility of the device are attributed to local (reversible) buckling to the polymer interpose layer.[106] The low modulus at 55.5 kPa allows the tunability for tactile imaging at 80 kPa that is comparable to human-touch. The device is highly linear in terms of both the current and I_{EL} (Fig. 3.4). The linearity is due to the

increase in number of percolation channel per unit cross-sectional area as the film is compressed. The electroluminescence conversion is high corresponding to low power consumption, ~0.25mW/mm^2, comparable to other electronic skin sensor (~0.6 mW/mm^2 [36]). As I_{EL} is linearly proportional to the local strain, the grey-scale of the tactile image maps the local stiffness variation.

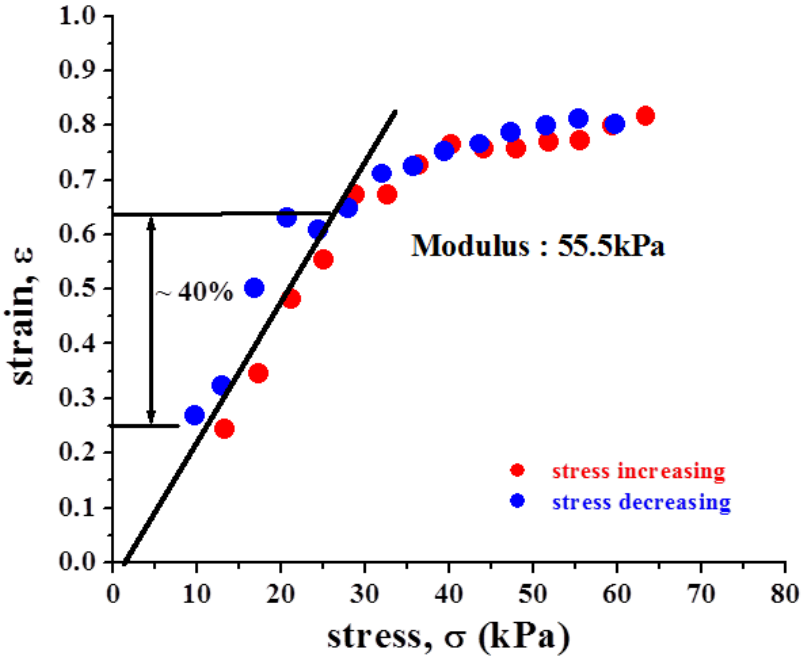

Figure 3.3 – Mechanical properties of the thin film tactile device. Strain-stress relationship was obtained from the electro-mechanical measurements. The modulus of the thin film was computed from the linear region, as indicated by the black line.

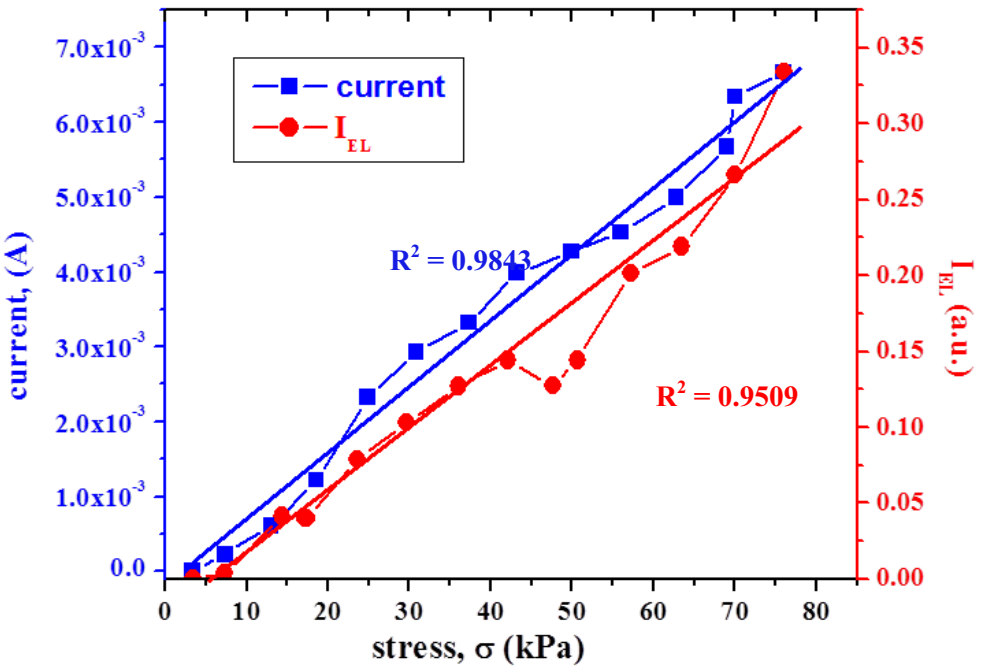

Figure 3.4 – Electro-optical properties of the tactile device. Electrical current and EL were measured as functions of stress. The dots represented experimental data while the corresponding lines were to guide the eye.

Two classes of palpable composite structures were fabricated to quantitatively image the variation in stiffness and anisotropic shape of the filler, respectively. For both structures, the filler d = 3.2 mm deep. In the first structure the cross-section was circular with E_T/E_M from 2.5 to 10 (Fig. 3.5a). The corresponding tactile image clearly shows the gradual decrease in contrast (i.e., lower EL) as E_T/E_M decreases from 10 to 2.5 (Fig. 3.5b). In the image (Fig. 3.5b), the region for E_T/E_M = 2.5 is not apparent indicating palpability at relative stiffness below 2.5x is background. (Although the contrast of 2.5 is measurable in quantitative line scan (Fig. 3.6a)). The increase in average EL from 2.5 to 5 and 5 to 10 are ~2.4 and ~4.1 that are reasonably linear. The strong contrast in the

tactile image for E_T/E_M above 5 meets the requirement for imaging mass of stiffness 10-fold higher than surrounding tissue for breast cancer screening. The second composite structure has two fillers but the cross-section is non-circular with sharp corners (Fig. 3.5c). The image clearly shows the non-circular shaped "corona" for E_T/E_M of 5 and the circular shaped central core with larger intensity (Fig. 3.5d). The linear scan across the image shows a rise in intensity ~ 6 folds (Fig. 3.6b).

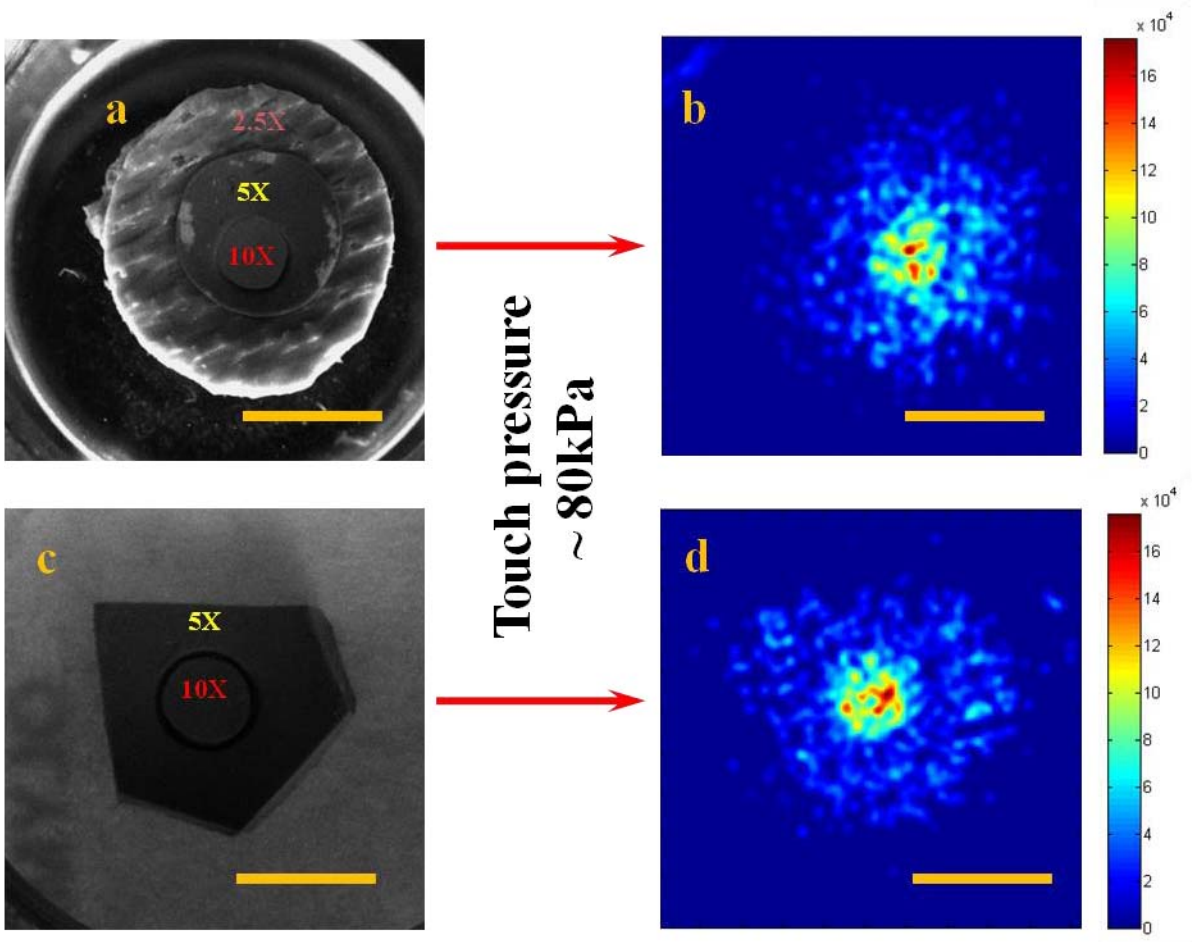

Figure 3.5 – Detection of 2 heterogeneous palpable structures. The first structure (Fig. 3.5a) included eccentric filler with E_T/E_M ranging from 10 to 2.5 in radial direction. The second structure was made with arbitrary shaped filler with E_T/E_M = 5, 10 (Fig. 3.5c). Tactile images (Fig. 3.5b, d) were obtained through touch experiments. The scale bar is 5mm. The tactile images are color coded with scale immediate to their right.

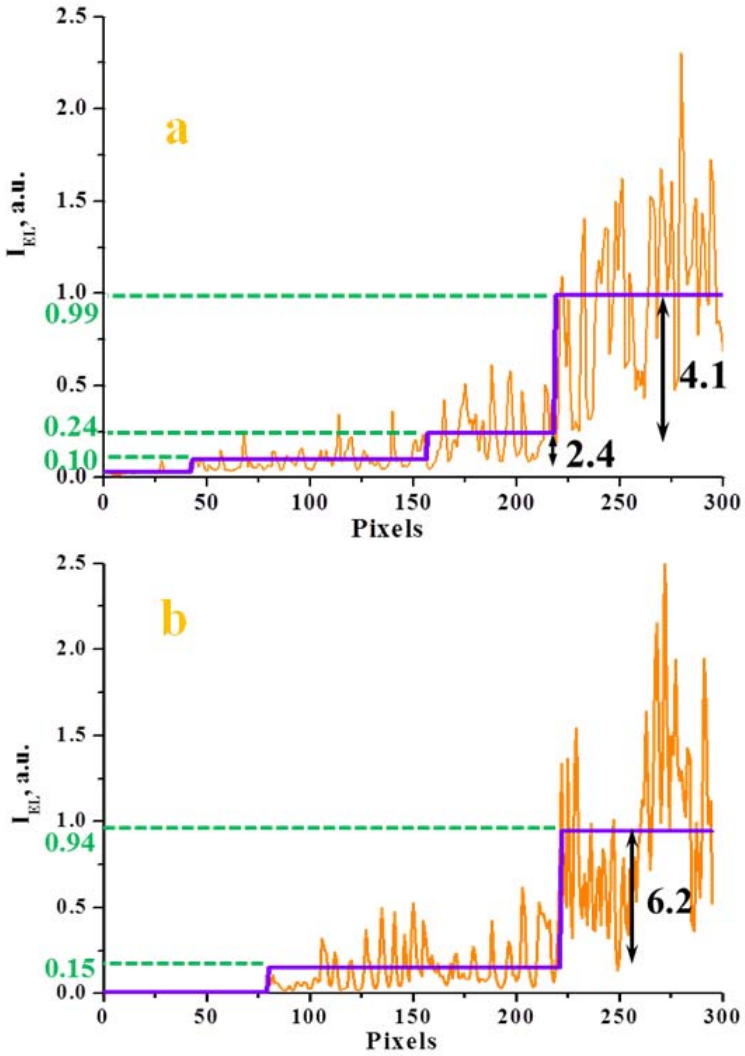

Figure 3.6 – Linear I_{EL} scans of tactile images. Figure 3.6 (a) and (b) are linear scans of Figures 3.5b, 3.5 d, respectively. The horizontal segment (purple) is averaged intensity.

We quantify the effect of d at fixed E_T/E_M, and conversely the effect of E_T/E_M at fixed d, on the image quality. The fillers are 3 mm thick (see Fig. 3.2) with L = 2 mm and 5 mm square cross-section, respectively (Fig. 3.7a, f). The $E_T/E_M = 10$ is fixed. For shallow depths $d \leq 3.2$ mm, the contrast is remarkable with sharp edges and corners (Fig.

3.7). The 2 mm mass (i.e., filler) is easily detected up to depths of 10 mm. However, the sharp edges at d = 10 mm is smeared. The circular-like shape and larger apparent size at 10 mm depth is because the differential stress field due to the filler tends to become isotropic. For larger size the shape appears to be intact. Importantly, For E_T/E_M = 10, the required minimum stiffness ratio to detect cancerous tumors in the breast, palpable filler of L = 2 mm at d = 10 mm is clearly visible in the tactile images. The EL intensity in all tactile images was color-coded with similar scale as in Fig. 3.5.

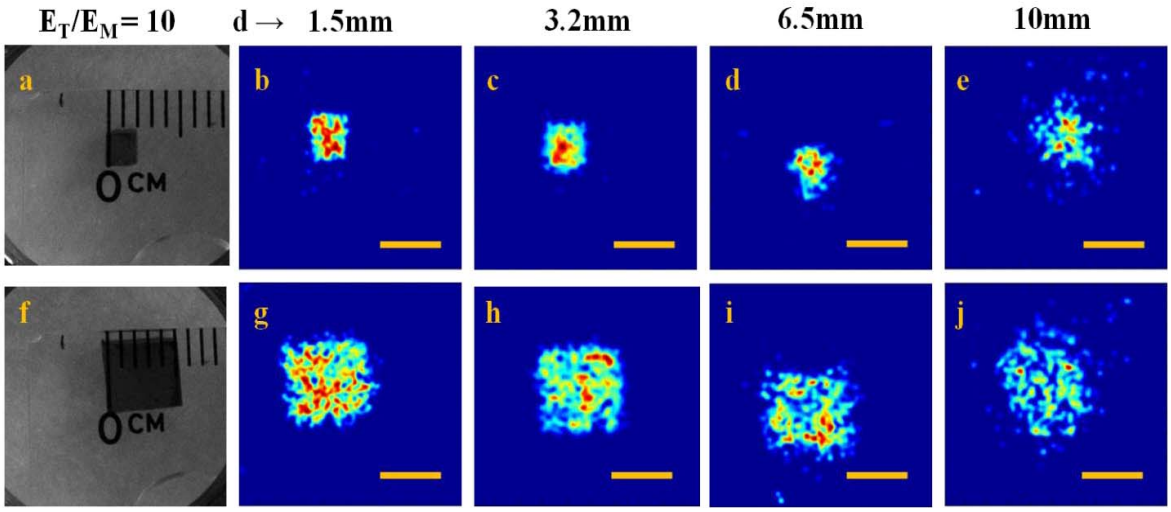

Figure 3.7 – Study of the effect of the embedded depth, d, on the performance of the tactile sensor. The stiffness ratio, E_T/E_M, is fixed at 10X. Two small rectangular fillers are placed at different depth ranging from 1 to 10mm (Fig. 3.7a, f). From left to right (Fig. 3.7b →e and Fig. 3.7g →j) tactile images of the 2mm and 5mm objects are shown, respectively. Scale bar is 5mm.

Next, d = 6.5 mm is fixed and effect of E_T/E_M was studied. The fillers are identical as in Fig. 3.7. Tactile images for L = 2mm filler were detectable for E_T/E_M = 10 (Fig. 3.8a). For E_T/E_M = 5, the shape is not apparent while at 2.5, the filler is below the detection limit. It is important to note that for this particular depth and E_T/E_M < 5 the

2mm filler is undetectable by human fingers. The larger filler (L = 5 mm) however, is clearly visible in the images for all E_T/E_M values. The device can clearly image fillers larger than 5 mm even at low stiffness ratio. This suggests that small variation in the stiffness (below 2.5) of size less than 2 mm, which may be due to (normal) heterogeneity in the breast tissue, will not be visible, indicating a low background, leading to higher contrast in tactile images for features with higher relative stiffness.

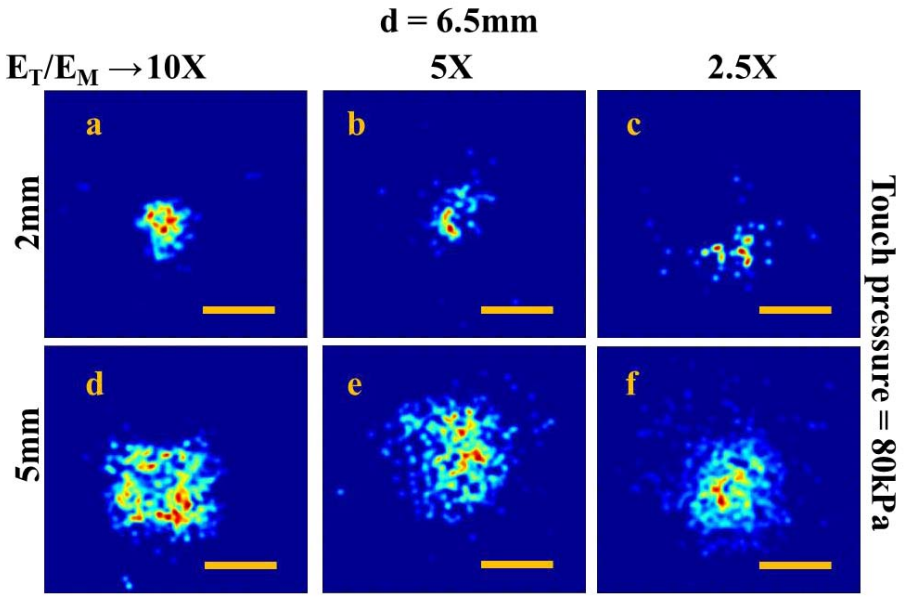

Figure 3.8 – Study of the effect of stiffness ratio, E_T/E_M on the tactile image quality. The fillers from Fig. 3 are used in this experiment. From left to right, tactile images of the fillers are shown (Fig. 3.8a →c and 3.8d →f) as E_T/E_M varies from 10 to 2.5, respectively. Color scale is similar to that of Fig. 3.5. Scale bar is 5mm.

A translucent breast model with visible fillers of relative stiffness, E_T/E_M = 10 from MammaCare Corp. is tested (Fig. 3.9a). The mechanical properties of the breast model are realistic in terms of overall stiffness, and are used to train medical personnel for CBE. The fillers of different shapes and size are located at depths ranging from ~ 2 to 20 mm (Fig. 3.9b). The tactile image of each of the fillers (i.e., simulated mass) 20 mm

below surface are correctly detected in the tactile images including the anisotropic shape (Fig. 3.9c to g). Dimensions of 5 mm are clearly apparent indicating that the device is promising as a screening tool to emulate CBE. To also note is that small distortion occurs because during the palpation the filler is mobile (similar to mass in breast) so only a portion of the filler produces the stress distribution (Fig. 3.10 and 3.11). Unfortunately the filler under the papilla could not be imaged properly although it was the largest. However the outline of the image is visible but not too conclusive. Feeling mass under the papilla also remains a challenge for CBE.

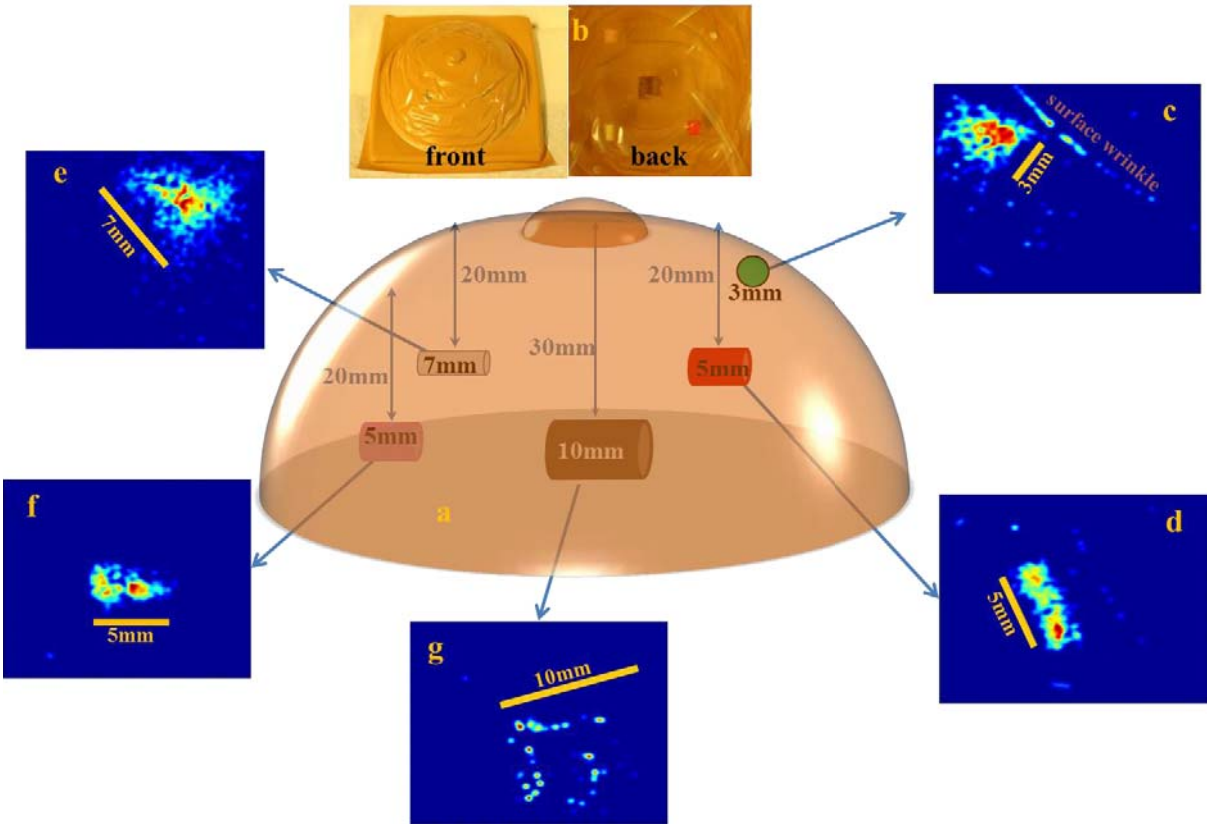

Figure 3.9 – Tactile imaging of a MammaCare breast model. Schematic and optical image of the model are shown in Fig. 3.9a, b. Note from Fig. 3.9b (left) there are wrinkles on the skin surface which are also detected in addition to the underlining tumors (Fig. 3.9c, d).

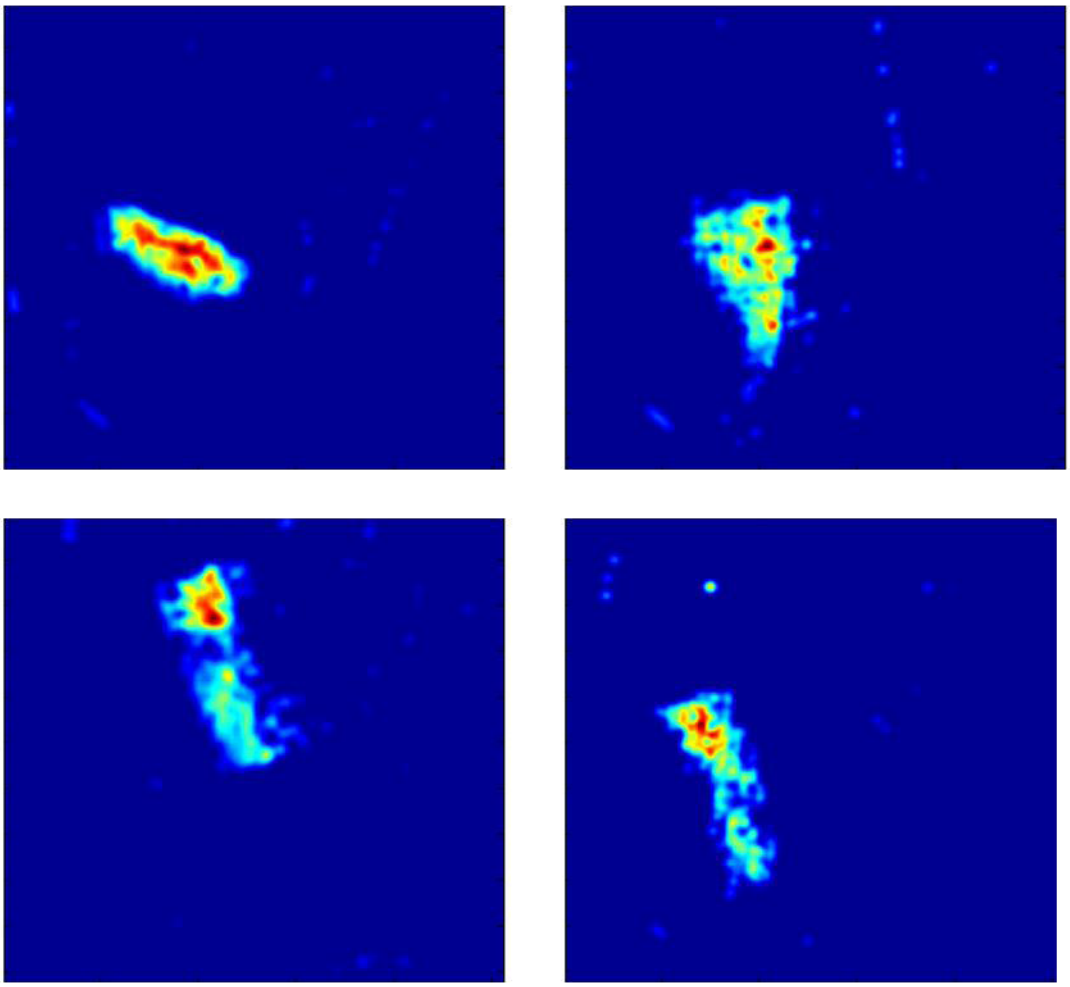

Figure 3.10 – A series of tactile images of the “red” filler (5 mm) in the breast model. The images are taken changing the relative angle of pressure applied on the breast model by the device. The change in measured shape is due to the movement of the filler.

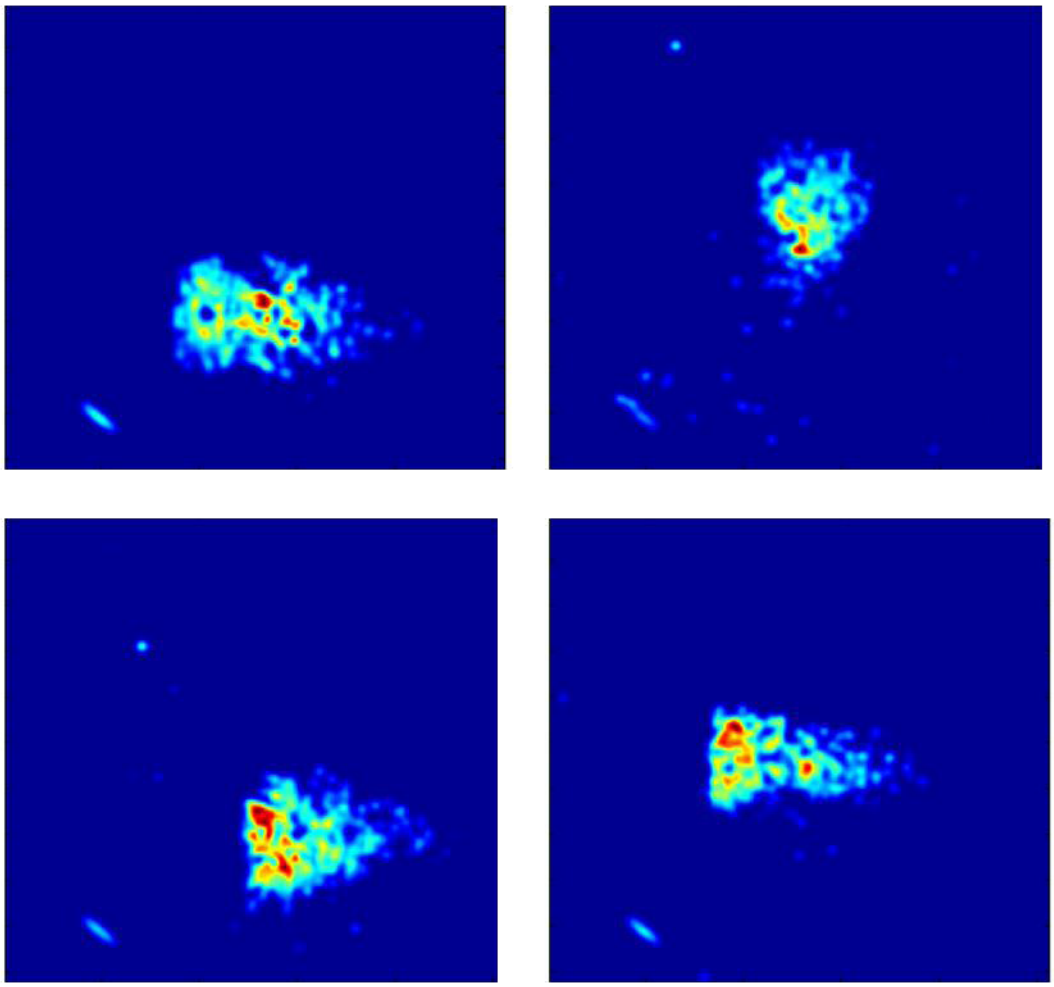

Figure 3.11 – A series of tactile images of the “pink” filler in the breast model. Similar to Fig. 3.10, the filler moves during imaging caused by changing the relative angle of applied pressure of the device.

3.4 SUMMARY

The device has four salient features that allows for optimum sensitivity to obtain palpable images 20 mm deep of 5 mm size structure. First, although the film is only ~150 nm it is sensitive to appreciable strain caused by contact pressure in 80 kPa range. The local buckling of the polymer film between the nanoparticles layers results in counter-intuitive softening of the film and reversible deformation up to 40% compression ratio (Fig. 3.4). The second aspect of the device is the linear response. The optical signal and the rise in electrical current on compression increase linearly with load (Fig. 3.3). The linearity is caused by linear increase in percolation path between the top and bottom electrode with increasing load. The tunneling current does rise due to compression but, the effect is insignificant compared to the increase in percolation. The third aspect is easy processing by simple dip coating and washing operation that allows fabrication of the device on large area flat or curved surface and substrates that may be rigid or flexible. The fourth aspect is that the signal from the film is continuous (i.e., analog device) where the contact pressure is directly converted to EL distribution making the data acquisition convenient and fast. Using an artificial breast model, the four features result in imaging palpability of clinical relevance to potentially screen for breast cancer. The smallest mass imaged by devices reported in the literature is 6 mm in diameter at depth up to 17.5mm but the stiffness ratio is ~ 22.[103] In breast model, a 5 mm long mass was accurately imaged at 20 mm depth (3 times the thickness of the mass itself) and E_T/E_M as low as 10. Smaller than 10mm in length are often difficult to detect even by a trained professional,[26] thus the device will improve outcome of CBE providing a quantitative image. Softer

mass ($E_T/E_M < 2.5$) are below the sensitivity level leading to background. Owing to the linear response of the device, the grey scale quantitatively maps the relative palpability.

CHAPTER 4

ELECTRICAL PLASMA FROM PERCOLATED 2-D ARRAY OF GOLD NANOPARTICLES AT ATMOSPHERIC PRESSURE

Smart designs of sub-wavelength structures enable observation of unusual properties of materials, and have led to new research areas such as metamaterials. Typically, Coulomb blockade effect is observed in array of conducting particles at cryogenic temperature due to local charging of a few particles by a single electron in the percolation path. We will describe a one dimensional (1 – D) network of Au nanoparticles (NPs) cemented by different materials exhibiting plasma generation in air at atmospheric pressure. The 1 – D array is a self-assembled monolayer network spanning between electrodes 10 – 100 μm apart. It is formed by first bridging the negatively charged 10 nm Au NPs with positive ions (Cd^{2+}, Zn^{2+}, Fe^{3+}) followed by cementing the bridge with reactive gas to form a robust 2 – D network. The nature of electronic emission in this nano – materials is explained in term of field induced ionization. These unique nano materials, that are fully self-assembled where, properties can be tailored by varying the cement chemistry, have potential applications in solid state lighting, and gas – sensors.

4.1 INTRODUCTION

Plasma is the fourth state of matter, besides solid, liquid, and gas. In general plasma can be defined as a neutral medium of positive and negative particles such as ions, charged molecules, electrons, etc. Following the discovery of carbon nanotubes (CNTs) using arc – discharge plasma, the use of plasma in nanoscience increases rapidly.[107,108] Ionized – gas (plasma) has proved essential in growth and processing (etching) of CNTs, graphene, graphene ribbons … in nanoelectronics. Recently it has been shown that atmospheric – pressure plasma can be used to treat cancer, such as melanoma.[108] Typically plasma is generated by a large electrical field applied across two electrodes in a closed environment (vacuum tube, chamber…) filled with a dielectric gas or fluid. The potential gradient beyond the dielectric limit of the gas causes electrical breakdown to occur as sparks (similar to lightning), leading to ionization of the gas, and creating plasma. The electrical field required is in the order of 10^7 V/cm.[109] In air at atmospheric pressure, electrical breakdown occurs between 10μm electrodes at bias of over 900V.[108,110,111] Several groups have studied applications of ionization gas sensors leveraging plasma generation.[112-114] The extremely high electrical field and vacuum environment requirements in these studies limited their practical use as gas sensors in the field. Thus an atmospheric – pressure plasma generation in air in low electrical field is of great interest.

Recently it has been shown that electrical breakdown in air can happen at ultra – low bias of ~ 40V using CNTs as anode.[115] Here we will describe a different approach leveraging self – assembled 2 – D array of Au nanoparticles (NPs) cemented by a dielectric material. Due to the unique spatial distribution of the NPs, electrical

breakdown occurs at 35V, leading to observation of plasma in air at atmospheric pressure. The light emitted from the plasma was visible to human naked eyes.

4.2 METHODS

Nanoparticle necklace array fabrication using Cd^{2+} ion and CdS nano-cement ($Au(Cd^{2+})$-NP necklace and Au(CdS)-NP necklace array):

A 3.2 mM of $Cd(ClO_4)_2$ solution was slowly added to 1 mL of 10 nm Au nanoparticle suspension at pH ~ 7 (BBI International) with 5.7 x 10^{12} particles/mL to form a necklace.[116] The formation of the necklace was evidenced by a change in color from red to blue after 12 hr. due to the shift in the Surface Plasmon Resonance (SPR) band from 525 nm to 610 nm in the UV-Vis spectrum. The shift, as discussed in the previous report,[116] was due to delocalization of electrons confined to a single particle to a larger number of particles in the 1D necklace.[116] The Cd^{2+} ion bridged necklace ($Au(Cd^{2+})$-NP necklace) was adsorbed on a SiO_2/Si chip by exposing it to the necklace suspension for 12-14 hr. at room temperature. The deposition occurred selectively on the patterned NH_3-plasma modified poly(dimethyl siloxane) (PDMS) stripes described below.

The chip has the following structure. The SiO_2 passivation layer was 500 nm thick, and the 50 nm thick Au electrodes with 10 nm thick TiO_2 adhesion layer were RF sputter through patterned SU8 photo resist. The gap between the Au electrodes was 10 μm. Prior to PDMS, patterning the chip was cleaned in a solution mixture of acetone and 2-propanol under ultrasonic treatment for 30 min. After vigorously washing in distilled water, the chip was exposed to Piranha solution (1:3 by volume of 50 wt% H_2O_2 and 95.0-98.0% H_2SO_4) to make its surface hydrophilic.

Subsequently, the $Au(Cd^{2+})$-NP necklace array was exposed to H_2S gas. The H_2S gas was generated by adding 0.5 g of sodium sulfide (from Sigma-Aldrich) to 5 mL of

sulfuric acid (from Sigma-Aldrich) in a home-built "Kipps" apparatus. On exposure, the Cd^{2+} ion bridge was converted to CdS causing nano-cementing between the adjacent particles. The formation of a Au(CdS)-NP necklace array was confirmed by optical and structural measurements discussed in the text. We also noted that because H_2S is a colorless and extremely toxic gas, the experiments were conducted in a well-sealed enclosure with an H_2S monitor.

For TEM sample preparation, a drop of fresh solution (~5 μL) was casted directly on a carbon-film-coated copper (Cu) grid (from Electron Microscopy Sciences) followed by immediate removal of the excess solvent using a blotting paper. The samples were allowed to dry for ~3 hr. For the Au(Cd^{2+})-NP necklace samples, the dried samples were subsequently exposed to H_2S gas in a home-built "Kipps" apparatus as mentioned above.

Necklace array fabrication using CdS nanoparticles bridge (Au(CdS NP)-NP necklace):

Instead of using Cd^{2+} ions as described above, CdS NPs were used to form a necklace with 15 nm Au NPs. Positively charged CdS NPs dispersed in water solution were synthesized using $Cd(ClO_4)_2$ as the Cd source and capped with cysteamine hydrochloride; and the density was about 10^{16} particles/mL.[117] The negatively charged 15 nm Au NP suspension at pH 7 with 1.4 x 10^{12} particles/mL was purchased from BBI International. A mixture ratio of 1:300 of CdS NPs to Au NPs suspension was prepared and shaken for about 12 hr. to form a necklace. Similar to the above necklace, the color of the mixture changed from red to blue upon the formation of the Au(CdS NP)-NP necklace. The necklace was deposited on the chip using a procedure similar to the one described above.

Soft lithography:

PDMS (Sylgard 184) purchased from Dow Corning was used to make a stamp for microcontact printing (μCP) using a standard method.[118] A 10:1 ratio of PDMS to cross-linking agent was mixed thoroughly and degassed under vacuum for 10 min. to remove unwanted microbubbles. The solution was poured on a mould with 80 μm wide lines (lithographically) etched in 3 μm thick photo resist (SU8). The PDMS was cured at 60 °C for 30 min. and peeled off from the mould to form a stamp.

An ink was prepared by mixing a 1:1 ratio of PDMS (viscosity 1500cst) and cross-linking agent (Gelest Inc.) followed by a 25-time dilution with Hexane. The 150 μL of the ink solution was spin-coated at 3000 rpm for 30 sec. on a cover slip. The PDMS stamp was placed on the cover slip to pick up some ink. The inked stamp was placed on the chip and heated at 60 °C for 30 min. The stamp was removed leaving a pattern of PDMS ink that had been cured due to the heating.

The 80 μm wide PDMS stripes were activated for selective deposition. The chip was exposed to NH_3 plasma at 80 W and 380 mTorr for 60 sec. On exposure to plasma, the surface of the PDMS stripes was modified by amine groups. Upon dipping the chip in the solution, the negatively charged necklace from the solution deposited on the positively charged $-NH_3^+$ group formed by the NH_3-palsma treatment.

Device characterization methods:

Absorption spectra were measured using an Ocean Optics Model USB2000 spectrometer. Scanning Electron Microscope analysis was performed on Hitachi S4700 Field-Emission SEM. Transmission Electron Microscopy (TEM) images were obtained by a JEOL 2010 Hi-Resolution TEM. Photoluminescence spectra of the necklace

suspension were obtained by a Hitachi Fluorescence Spectrophotometer F-4500. Electroluminescence experiments were performed in a home-built system using Acton Spectrophotometer 150 and IN/CCD-1340/100-EB/1 CCD camera to capture the spectrum. The total electroluminescence intensity data was acquired using a Hamamatsu H5784-03 photomultiplier tube (PMT). The current (I) – voltage (V) measurements were preformed in a Faraday cage using an Agilent 3458A multimeter and Agilent 6613C power supply.

Imaging specular EL from the array:

The EL from the nanoparticle array was imaged on an optical microscope using a Cascade II CCD camera from Roper Scientific. Cascade II CCD camera has pixel size of 16 by 16 micron with an imaging array of 512 by 512. The quantum efficiency is more than 90%. The CCD was installed on the optical microscope with a 20X objective for a total of 200X magnification. The images were taken at a fixed bias for 2-3 minutes at an interval of 2 seconds each. This step was repeated across a range of biases (12V-20V).

Analysis of the EL images:

The images obtained are 512 by 512 in a tiff file format. The noise was filtered by removing high frequency noise and setting illuminated pixel cluster below a certain threshold to zero. The data was processed in Matlab. All the temporal images acquired every 5 seconds at fixed bias were superimposed to generate a composite image. The composite images were compared to quantitative measure the amount of overlap between illuminated pixels. The comparison was performed for composite images at various magnitude and direction (i.e., forward and reverse) of bias.

4.3 RESULTS AND DISCUSSION

The chain – like self – assembly (necklace) of Au nanoparticles (NPs) (10nm in diameter) was mediated by oppositely charged ions (Cd^{2+}, Zn^{2+}, Ca^{2+}, Fe^{2+}, Fe^{3+}, H^{+}). The cemented necklace material was subsequently deposited on a Si/SiO_2 chip. The bridging ions was then allowed to react with H_2S gas in a control environment, forming cementing materials such as CdS, ZnS, CaS…, respectively. At this point, the necklace is considered cemented due to an apparent coating of the NPs with correspondent cementing material. This unique 2 – D array morphology is evident in Fig. 4.1a. The entire process was published in the literature with more details.[119] Upon applying bias exceeding 40V, the 2 – D morphology of the necklace transformed into a highly heterogeneous structure including coalesced islands interconnected by Au nanowires (filled with voids) (Fig. 4.1b). Typically prior to the transformation the 2 – D array of necklaces is percolated and electroluminescence due to ionization of the cementing material has been observed at bias under 20V.[119] However in the 40V bias regime, the Au NPs appear to be welded and become large island (~ 100nm across) and nanowires (~ 50nm wide). The coalescence of the necklace is a random process. As the result, the dense and uniform coverage of necklaces when first deposited on the chip (Fig. 4.1a) turned into more condensed and rugged morphology with void area (Fig. 4.1b). Such extreme transformation under the influence of electrical bias has not been observed.

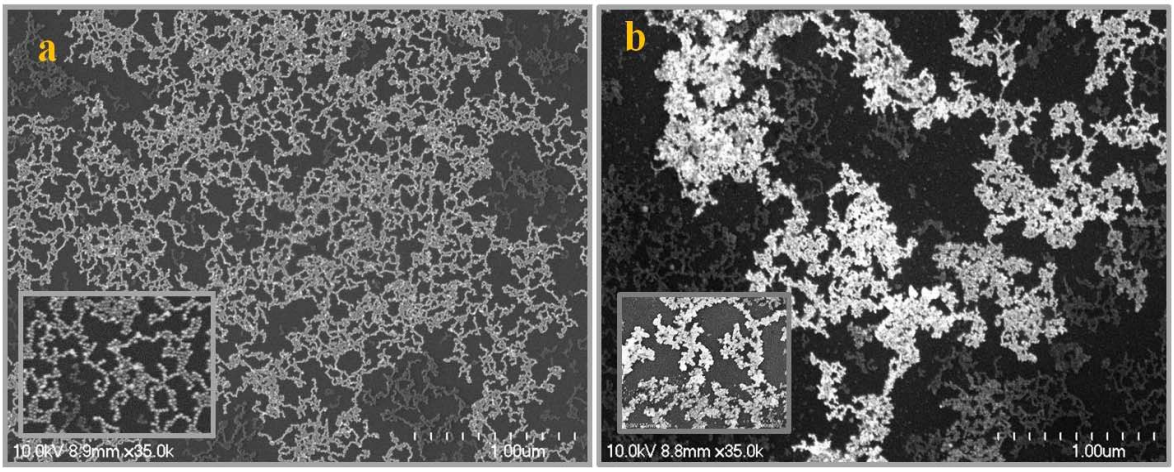

Figure 4.1 – Scanning Electron Micrographs of the cemented ZnS – Au NPs necklace device. Fig 1a shows the morphology of the necklace after cementing with H_2S, including a magnified view in the inset. Fig 1b is the SEM images of the cemented necklace after a bias of 40V was applied.

As a result, the current (I) – bias (V) behavior of the necklace device is extraordinary (Fig. 4.2). Initially the electrical conductance was low up to ~ 30V (black curve in Fig. 4.2). At 40V, there was a sudden increase up to ~ 10 folds (Fig. 4.2, inset). This unique behavior is in agreement with the morphological transformation to nanowires (Fig. 4.1) (as described above). Electrical conductance continued to rise after the first bias scan even when bias decreased (red curve in Fig. 4.2). All I – V data obtained later were signified with a definitive peak around 7V followed by a negative resistance behavior in bias region of 7 – 10V. Note that the current was high (mA) throughout the entire bias range. Owing to the highly rugged morphology of the necklace – nanowire formation (Fig. 4.1b), at low bias (0 – 7V) electrical charging occurred and maxed at 7V, resulting in a decline in conductance even when bias increased from 7 – 10V. Beyond 10V, current rises with increasing bias monotonically. Compared to the 1st cycle, from the 4th cycle onward, current increased an additional 10 folds beyond bias of 40V. This

increment was possible due to the transformation from 10nm wide 1 – D chains of single NPs to larger "electrical highways" of 50nm wide welded – NPs nanowires. Optical measurements using a photomultiplier tube (PMT) obtained simultaneously with I – V measurements reveals that at 10V, optical signal begins to rise. Beyond bias of 30V, the entire necklace between the electrodes (10µm wide, 6mm long area) is visible to the naked eyes (Fig. 4.3, inset), owing to the extraordinary high optical signal (Fig. 4.3).

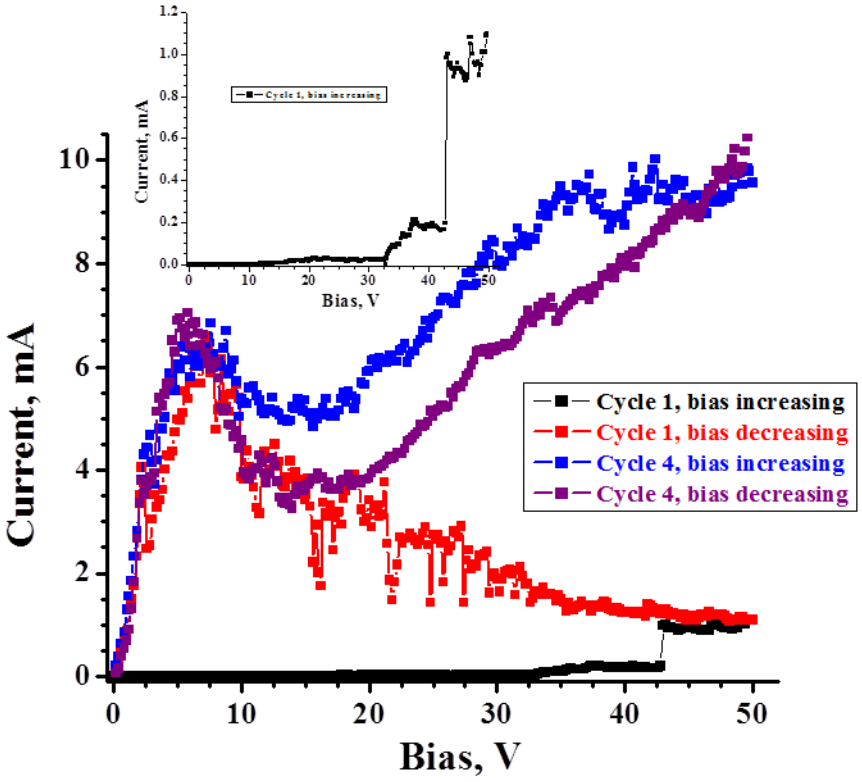

Figure 4.2 – Electrical property of the cemented necklace device. I – V data were obtained across 10µm gap electrodes. The inset shows I – V curve from cycle 1.

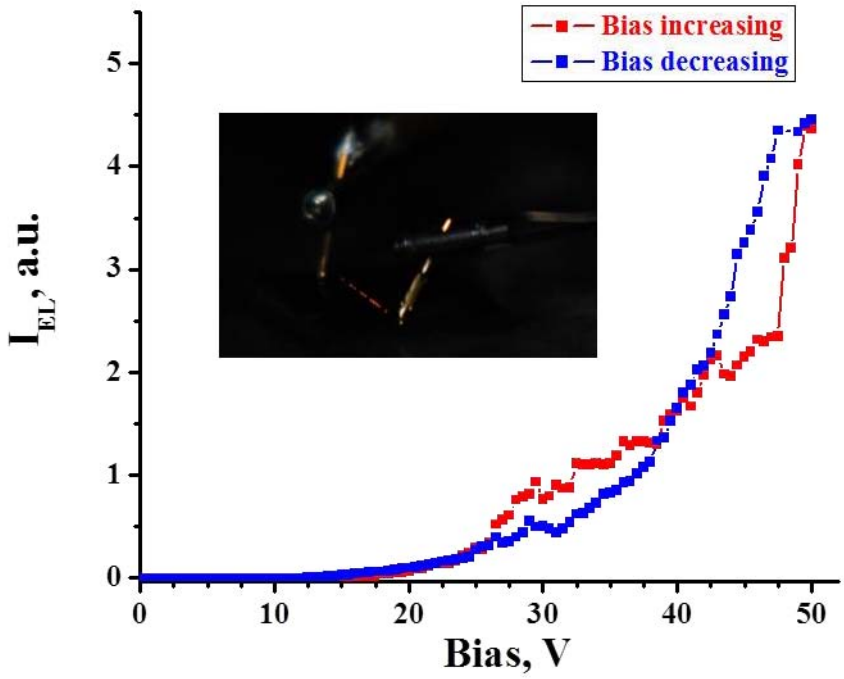

Figure 4.3 – Electro – optical measurements of the necklace device. The data were obtained simultaneously with Fig. 4.2. Note that optical signal starts increasing ~ 10V.

In this particular self – assembly of Au NPs, the property of the material as a whole is dictated by the cementing chemistry. For example, the cemented CdS – Au NPs necklace has been shown to emit electroluminescence (EL) from the CdS at bias of 20V[119] (black curve in Fig. 4.4). Interestingly, beyond 35V bias there are distinct narrow peaks (spikes) occurring on top of the base peak (broad EL from CdS at bias of 20V) (Fig. 4.4). From Fig. 4.4, it is apparent that these extra spikes are the only difference in optical property when applied bias increases from 20V to 50V. The spikes occurred at distinct spectral lines (2.08 eV, 1.97 eV, 1.84 eV, 1.76 eV, etc.) (Fig. 4.5). These extra contributions to the optical properties of the necklace are responsible for the extraordinary brightness of the material at bias exceeding 40V.

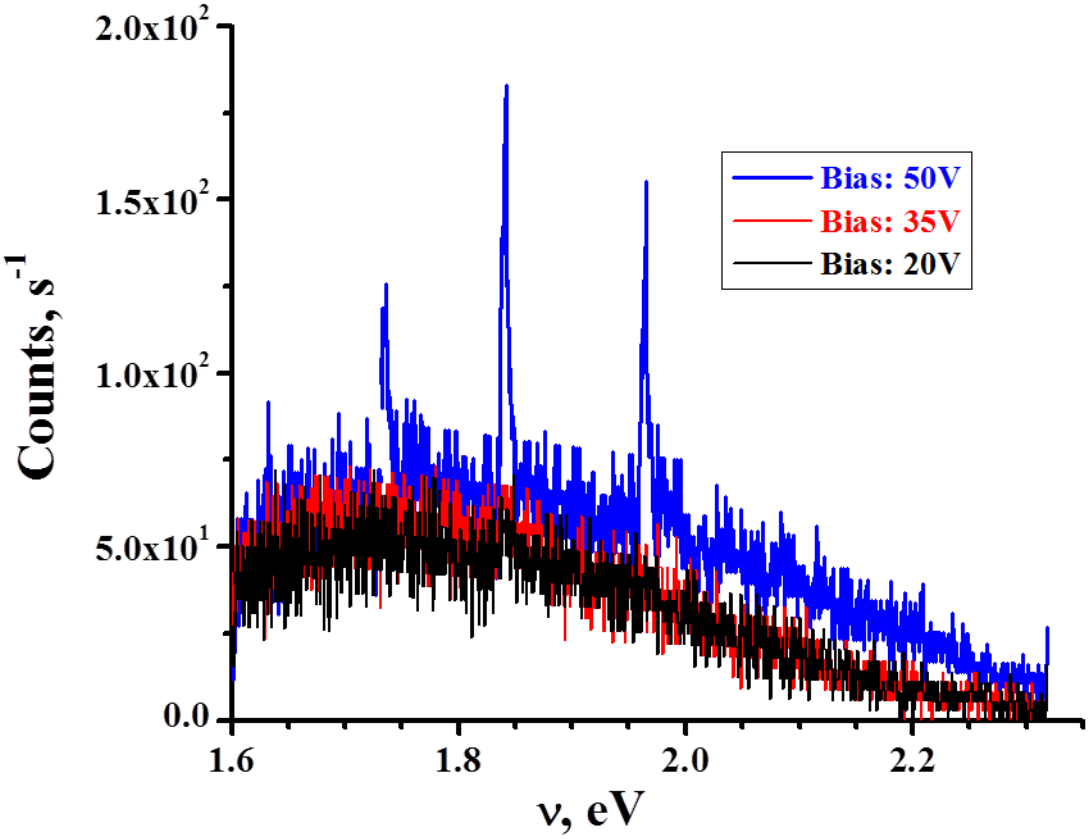

Figure 4.4 – Optical properties of the emitted light as a function of applied bias. The spectra were obtained with cemented CdS – Au NPs necklace device across 10μm gap.

To understand this unique observation, various experiments were conducted to understand the origin of the extra sharp spikes in the optical measurements (Fig. 4.4). A series of necklaces were fabricated with numerous cementing materials such as ZnS, CaS, FeS, and HS, following similar procedure described above. The precursor of the cemented HS – Au NPs necklace is proton (H^+) mediated Au NPs necklace. The optical properties of the necklace series are shown in Fig. 4.5. Depending on the cementing material, the broad base peaks varied (CdS against ZnS) but interestingly the narrow spikes were consistent in all necklaces. Independent of the materials, the spikes occurred

at exact distinct positions. The non – electroluminescent necklace (cemented HS – Au NPs NL) also demonstrated this phenomenon.

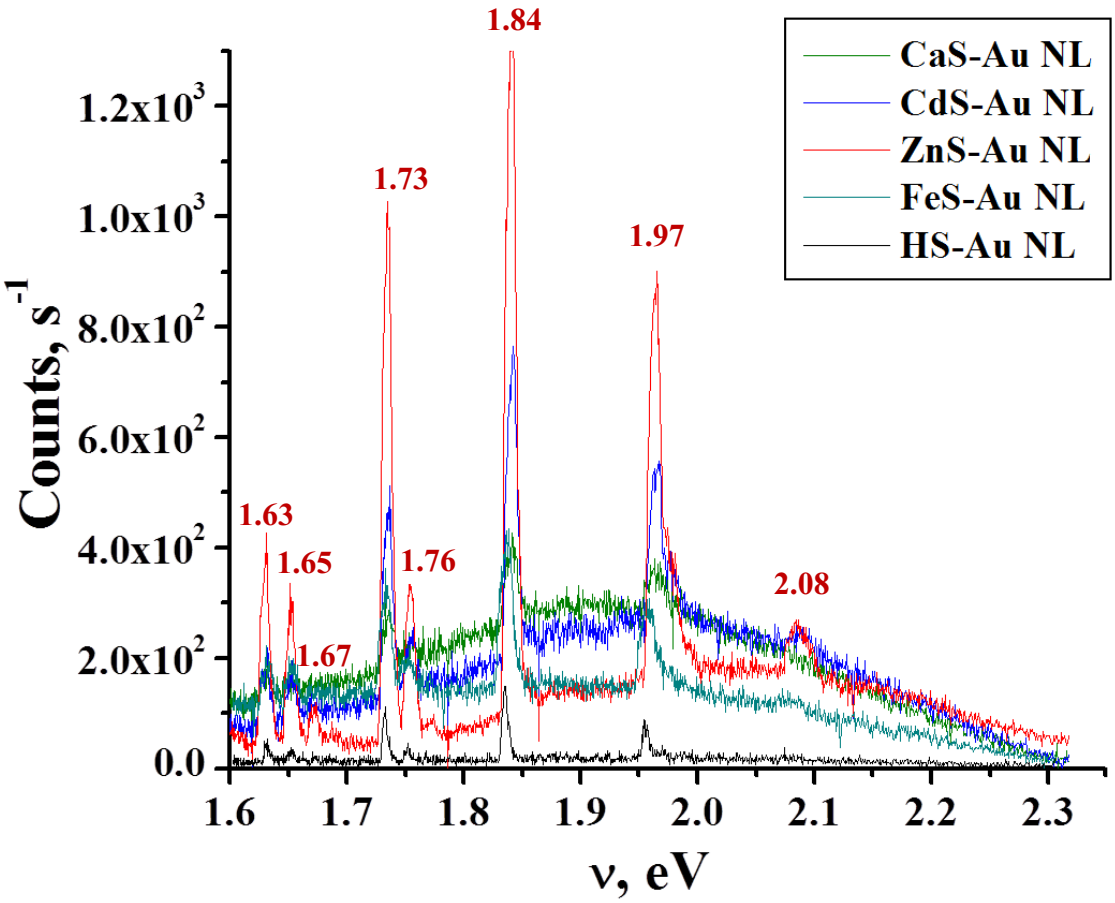

Figure 4.5 – Optical spectra of series of necklaces. All measurements were conducted with similar conditions such as applied bias, 10μm electrodes.

Subsequently a second series of necklaces (CdS is the common cementing material) were fabricated with larger (15nm in diameter) Au NPs, and 20nm Ag NPs. Also the Au electrodes were replaced with Pt electrodes. Their optical properties were measured in Fig. 4.6. Consistently the results are identical (Fig. 4.6). It is evident that

the extra spikes result from a secondary phenomenon to the necklace – related processes. All measurements were performed in air at atmospheric pressure.

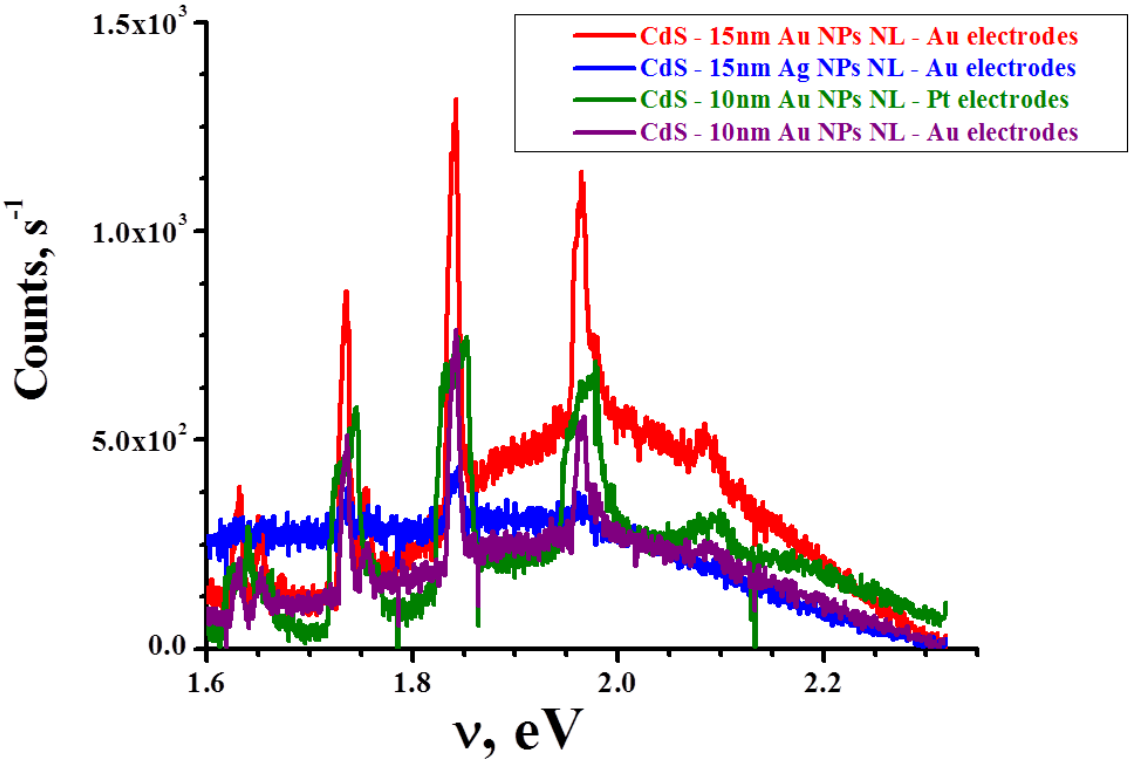

Figure 4.6 – Study of the effect of different NPs, electrode material on the optical property of the necklace.

Optical measurements of the cemented CdS – Au NPs necklace device were conducted in various gaseous environments (Fig. 4.7). Interestingly the broad base peaks from the CdS materials remain intact while the sharp spikes changes with different gases. The relative intensities of the spikes at 1.84, 1.76, 1.67, and 1.65 eV are distinctive for Ar and N_2 (Fig. 4.7). Thus the extraordinary brightness emitted in high bias regime (> 35V) is from electrical plasma created on the surface of the necklace. Following the morphological transformation, charging in low bias regime (0 – 7V) leads to extremely

large potential gradient within the necklace, enough to ionize the cementing material and the gas in the environment in high bias regime (> 35V). This process is power efficient. The external efficiency was estimated to be ~ 6%, comparable to light emitting diodes. In case of electrical breakdown and gas ionization between air – gap electrodes (< 50μm apart), the required applied bias is usually several 100s V and current is low (~ μA).[107,108] The described heterogeneous morphology of the 2 – D array of unique Au NPs necklace allows robust creation of plasma with the environment at atmospheric pressure that is visible to the naked eyes.

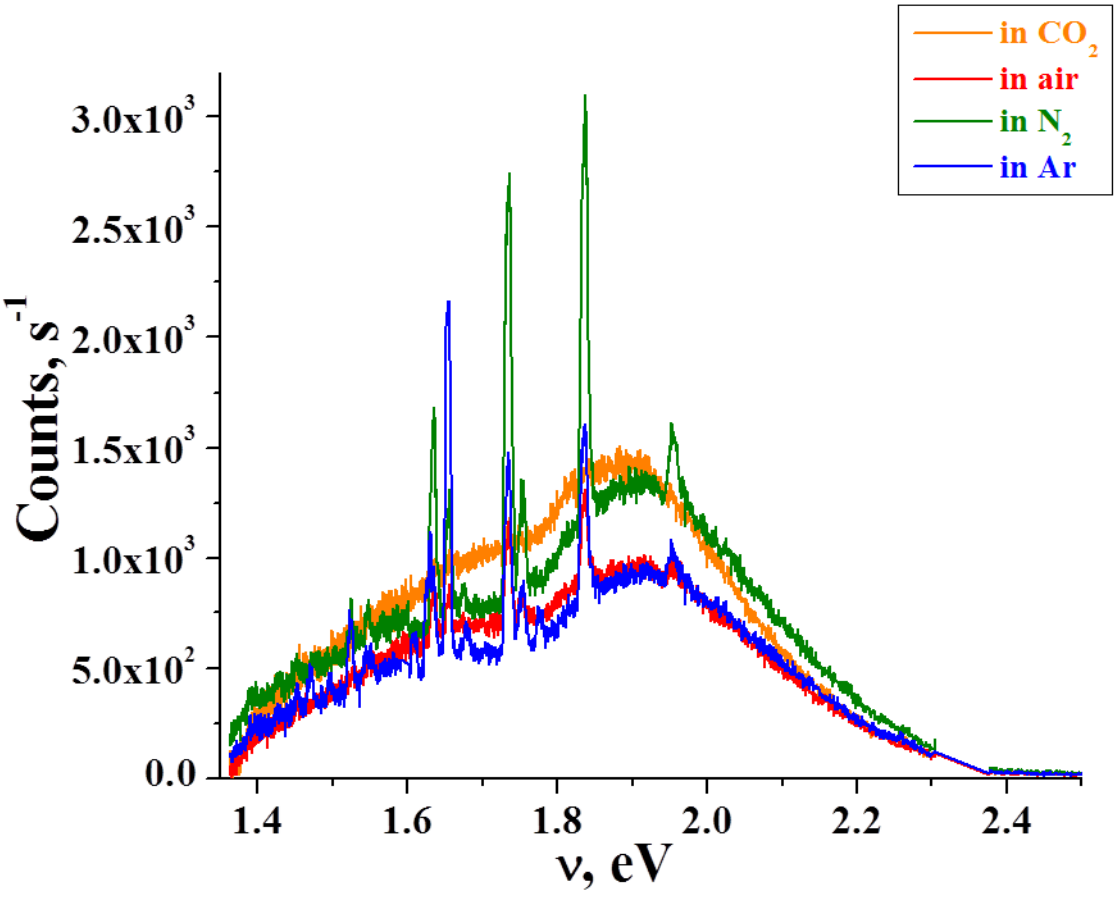

Figure 4.7 – Study the optical property of cemented CdS – Au NPs necklace in various gas environments.

4.4 SUMMARY

The self – directed self – assembly of Au NPs into micro meters long 1 – D chains is a versatile class of materials. The cemented CdS – Au NPs necklace when deposited in a quasi 1 – D array exhibits single electron effect at room temperature and electroluminescence due to ionization of CdS.[119] In 2 – D array the identical necklace material reveals interesting phenomena in high bias regime (> 35V). First is the negative resistance behavior from 7 – 10V. It is attributed to be the results of prior (bias lower than 7V) charging effect within the transformed necklace. Second phenomenon is the observation of electrical plasma demonstrated as sharp spikes on top of the typical base peak in optical spectra (Fig. 4, 5, 6, 7). Consequently, the entire necklace between the electrodes (10 μm wide, 6 cm long) is extraordinarily bright, thus visible to the naked eyes. The electron emission phenomenon (plasma) observed with the necklace device (similar to cathode ray tube) can pioneer new possibilities in solid state lighting applications.

CHAPTER 5

MAGNETIC 1-D CHAIN OF PERIODIC HETEROGENEOUS Fe_xO_y-AU NPs JUNCTIONs

In recent years magnetoresistance has been the fundamental concept responsible for many technological advances, especially in computing and memory devices. With the discoveries of giant magnetoresistance, device processing technique, i.e. lithography, is the only limiting factor. Self – assembly of nanometer sized nanoparticles (< 10nm) to form multifunctional device, especially those with heterogeneous structure, may be the key to future applications. Here we describe a simple design to fabricate a quasi one – dimensional self – assembly of Au nanoparticles connected by magnetic Fe_xO_y. The single – electron device based on this unique material exhibits spin – valve behavior at room temperature. The bridging Fe_xO_y was estimated ~ 2 – 3nm but shown ferromagnetic property at 295K. Magnetization hysteresis curve shows Barkhausen effect. The heterogeneous Fe_xO_y – Au NPs nanomaterial has a great potential in memory device applications.

5.1 INTRODUCTION

Rapid studies about magnetism have been spurred by not only curiosity but also great technological applications. The 21st century has witnessed great many developments in personal computing devices, solid state memory devices, spintronics.[120-124] The size of the computer decreases greatly from size of a truck before 1960s[125] to a book size (laptop computer) today. One of the most prominent discoveries is the work on giant magneto resistance (GMR),[126] which has led to 2007 Nobel Prize.[127] Magnetoresistance (MR) is the property of the material whose electrical resistance can be manipulated by external magnetic field. Today GMR is the fundamental concept in a variety of electronic devices such as magnetoresistive random accessing memory (MRAM),[128] Hall Effect devices,[129] spin valves,[121-123] spin transfer torque-MRAM (STT-MRAM).[130] A typical GMR-based device consists of thin multilayer film strutures of magnetic/non-magnetic/magnetic materials. In MRAMs and STT-MRAMs the write and read speed can be ultra-fast, but the size of each bit is still limited by fabrication process, i.e. lithography. Thus an ultra-small MR device is of great interest.

Here we describe a spin – valve behavior from a quasi one – dimensional (1-D) array of self – assembled Fe_xO_y – Au NPs necklace material. The necklace array spans several micro meters long, made up of Fe_xO_y – Au NPs junctions in periodical arrangement. Owing to the highly heterogeneous structure, the necklace device exhibits single electron effect coupled with ferromagnetism from ultrathin (2 – 3nm) Fe_xO_y cementing material. Coercivity, χ_c, of over 500 Oe was estimated, leading to ~ 30% increase in electrical conductivity. This spin – valve behavior was observed at room temperature (295K).

5.2 METHODS

Iron oxide – Au NPs 1 – D chain (necklaces) Fabrication. A stock solution was prepared by adding 7.894 mg iron (II) chloride tetrahydrate ($FeCl_2.4H_2O$) and 57.36 mg iron (III) chloride hexahydrate ($FeCl_3.6H_2O$) in 10ml H_2O. A total of 42µl of the stock solution added drop-wise to 1ml of 10nm Au NPs solution (BBI International). The mixture was allowed to stir overnight. The formation of the necklace was evidenced by a change in the solution's physical color from red to blue. The necklace solution was allowed to react with 10µl of 7% ammonia hydroxide (NH_4OH) solution to "cement" the Fe-Au NPs junctions to form iron oxides. This cement material (iron oxide) was formed when the solution changes color from blue to dark. The necklace was subsequently deposited on a Si chip between 2 Au electrodes (10µm apart). The Si surface was first cleaned and sonicated for 20 minutes in 1:1 mixture of acetone: isopropanol. Next the chip was rinsed thoroughly with DI H_2O before submerged in piranha solution (3:1 mixture of sulfuric acid: hydrogen peroxide). The a thin layer of poly(dimethyl-siloxane) (PDMS) was allowed to cure at 60 degree on top of the Si chip in 40 minutes before peeled off. The necklace solution was allowed to sit on t op of the Si chip in about 20 hours for adsorption of the necklace. The device was finally rinsed gently with DI H_2O and air dried.

Device characterization methods. UV-vis absorption spectra were obtained using an Ocean Optics model USB2000 spectrometer. Scanning electron microscopy analysis was performed with a Hitachi S4700 field-emission SEM Transmission electron microscopy (TEM) image were taken by a JEOL 2010-high-resolution TEM. The current

(I) – bias (V) measurements were collected using a Agilent 345A multimeter and Agilent 6613 C power supply via home-built computer software.

5.3 RESULTS AND DISCUSSION

The micrometers – long 1 – D chains necklace of periodic Fe_xO_y – Au NPs junctions was fabricated by first reaction Fe^{2+}, Fe^{3+} ions with negatively charged Au NPS, and second adding ammonia hydroxide to form iron oxide (FeO, Fe_2O_3, Fe_3O_4) (more details in section 5.2 Methods). The dimensional transformation from individual NPs to necklace – like structure (quasi 1 – D) was evidenced by color changing from red to blue (Fig. 5.1 inset). After the cementing step, the solution color changed from blue to dark brown, indication formation of Iron oxide (FeO, Fe_2O_3, Fe_3O_4) (Fig. 5.1 inset). The 2 step formation of the Fe oxide-Au NPs NL also resulted in a red shift in the optical absorption of the material in the UV – visible range (Fig. 5.1). The surface plasmonic resonance of 10nm Au NP peaked at ~ 520nm. Upon addition of Fe^{2+}, Fe^{3+} irons and subsequently NH_4OH solution, the absorption peak red-shifted to 620nm confirming structural transformation from 0 – D to local 1 – D.

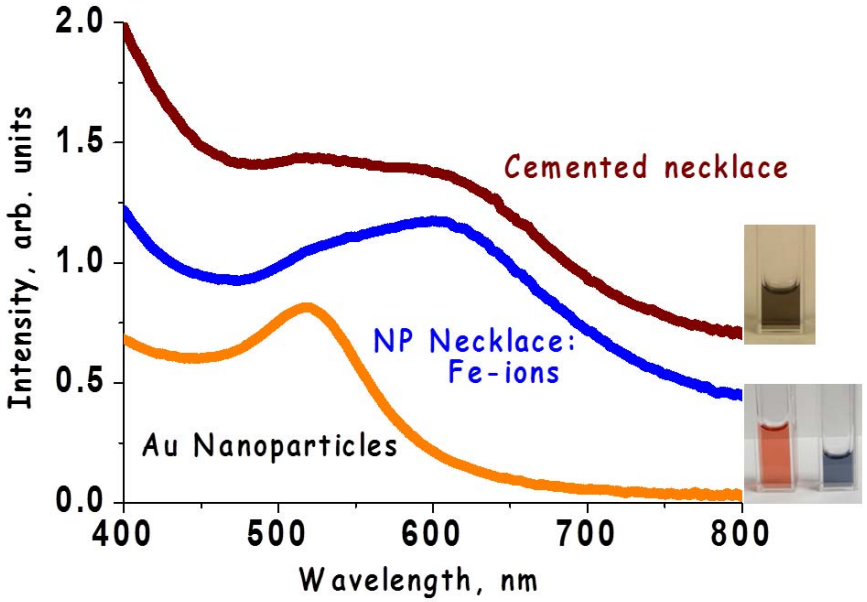

Figure 5.1 – Fe_xO_y – Au NPs necklace formation as evidenced by UV – vis absorption spectra. Insets are optical images of corresponding solutions.

The Fe_xO_y –Au NL has populated islands of NPs connected by local 1 – D chains, i.e quasi 1 – D (Fig. 5.2). Before cementing with NH4OH solution, the Au NPs were apparently individuals only bridged by Fe^{2+}, Fe^{3+} ions (Fig. 5.2a). The interparticle distance was estimated about 2nm. Upon cementing, these Fe^{2+}, Fe^{3+} bridges formed Fe_xO_y coating (cementing) surrounding Au NPs (Fig. 5.2b, c). The Fe_xO_y bridging material was approximately 2nm in length. The Fe_xO_y was evidenced in the result from an energy dispersive X-ray (EDX) analysis (Fig. 5.3). The approximated ratio of Fe:O is 1:7. It is not conclusive at this point the identity of iron oxide formed in the NL. Due to the self-assembly process, it is suspected to be highly heterogeneous. Therefore various combinations of FeO, Fe_2O_3, Fe_3O_4, are likely possible. From here on, the iron oxide material is referred to as Fe_xO_y.

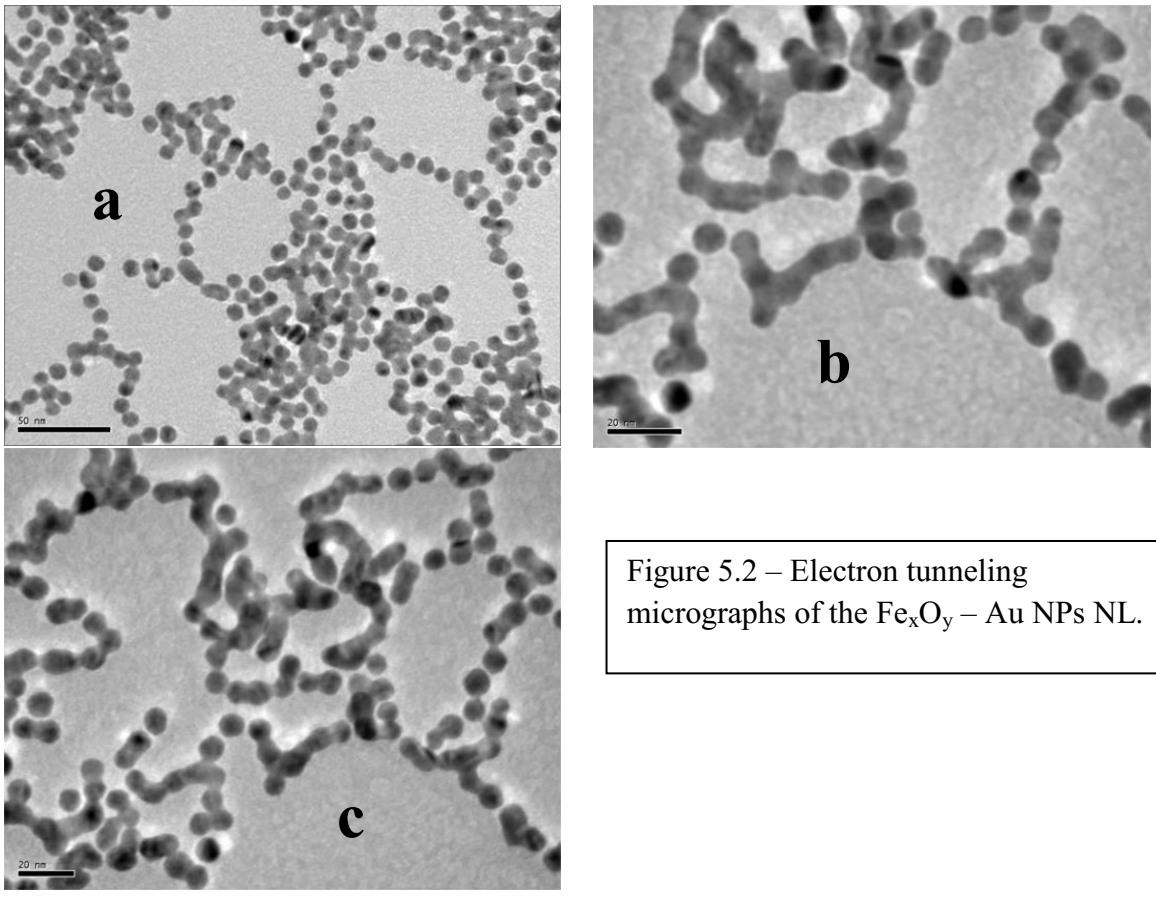

Figure 5.2 – Electron tunneling micrographs of the Fe_xO_y – Au NPs NL.

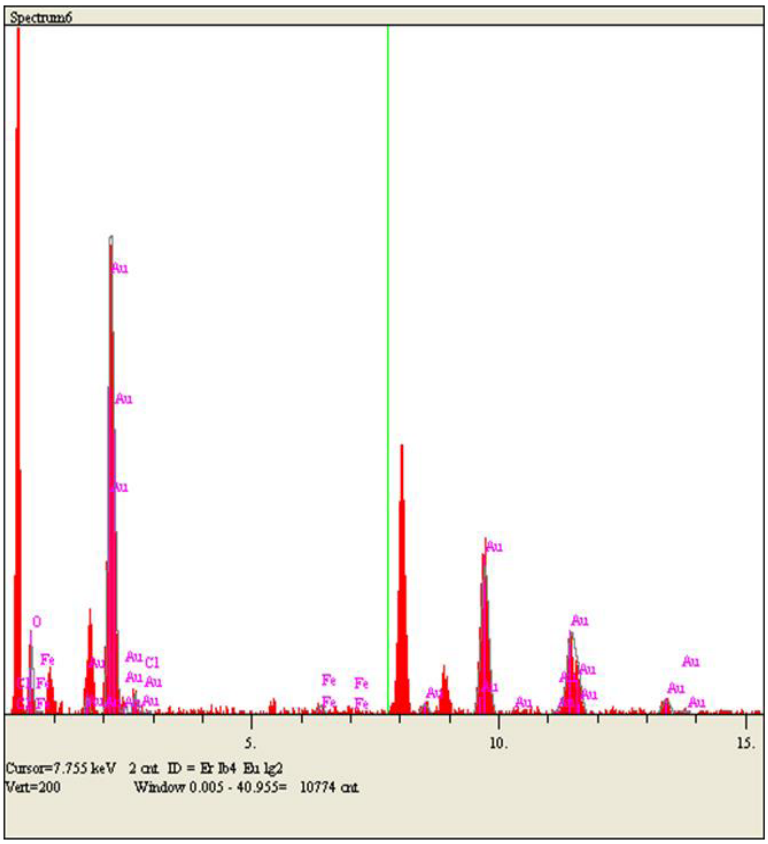

Elt.	Line	Intensity (c/s)	Error 2-sig	Atomic %	Conc	Units	
O	Ka	2.86	0.437	52.222	9.192	wt.%	
Cl	Ka	1.11	0.271	5.182	2.021	wt.%	
Fe	Ka	0.70	0.216	2.264	1.391	wt.%	
Au	La	13.96	0.965	40.332	87.396	wt.%	
				100.000	100.000	wt.%	Total

Figure 5.3 – Energy dispersive X-ray analysis of the Fe_xO_y – Au NPs NL.

The Fe_xO_y – Au NPs NL was deposited on a Si/SiO_2 chip by an adsorption procedure described in the literature. Electron micrographs of the deposited Fe_xO_y – Au NPs NL revealed 2 – D array structures with 1 – D locality (Fig. 5.4). The Au electrodes on Si/SiO2 chip were 10μm apart. The Fe_xO_y Au NPS NL was an adsorbed as a single layer (monolayer), apparent from Fig. 5.4. Therefore when a bias was applied across the Au electrodes, current flows only in the x-y plane, i.e. no contribution from z – direction.

Owing to the unique local 1 – D of the NL array (Fig. 5.2 and 5.4), the electrical current (I) – bias (V) relationship is non – linear (Fig. 5.5). The non – linearity arises from Coulomb blockade effect.[64] It is well-known that a single electron can charge several nanoparticles leading to a "blockade" (potential barrier) in current. Only above a certain bias, called threshold bias, electrons can overcome this barrier and current rises as..This single electron behavior has been observed primarily in cryogenic temperature (<70K). Here the Fe_xO_y – Au NPs NL device acts as a single electron device at 295K with a significant V_T ~1.59V. In addition, the highly heterogeneous Fe_xO_y – Au NPs junctions self-assembled periodically within this array exhibits magnetism. To our best knowledge, this is the first time single electron behavior coupled with magnetism is observed at room temperature (195K) in a single device. Under the influence of applied magnetic field (H) of ~ 70 mT, the electrical current doubles (Fig. 5.5). Also to be noted is stays constant at 2.1 (corresponding to the local 1 – D nature of the necklace[63] with applied magnetic field (apparent in blue and red curve in Fig. 5.5, while V_T increases from 0.81V to 1.5V. Thus magnetic field can amplify the single electron effect in this unique device.

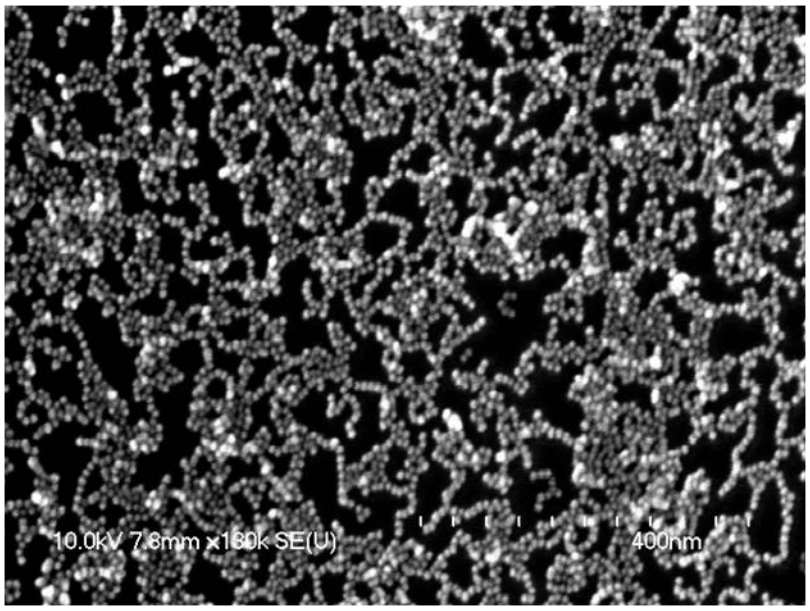

Figure 5.4 – SEM images of the Fe_xO_y – Au NPs NL device as deposited on Si/SiO_2 chip.

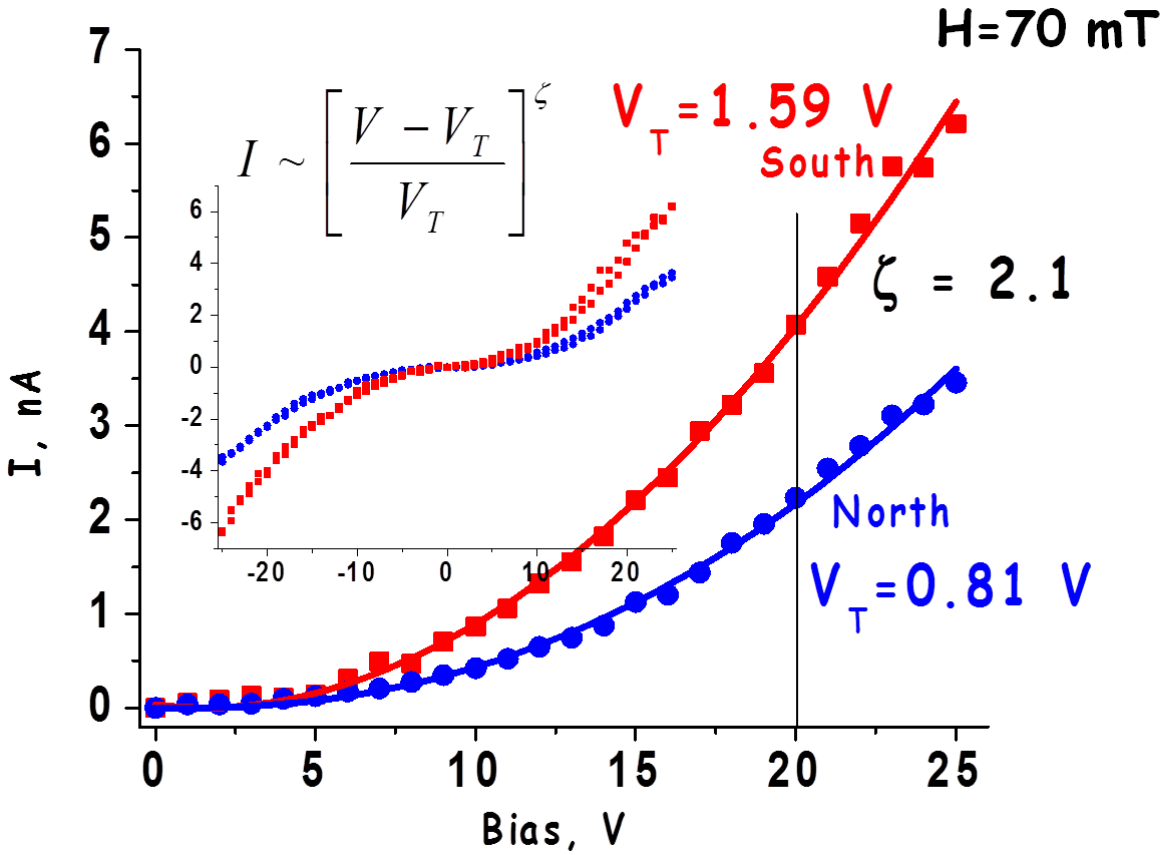

Figure 5.5 – Electronic transport behavior of the Fe_xO_y – Au NPs NL at 295K.

Given the estimated size of the Fe_xO_y bridging material between the Au NPs is ~ 2 – 3 nm (comparable to the size of a single magnetic domain), the observed magnetism is suspected to be para-magnetic. To study the magnetic properties of the Fe_xO_y – Au NPs NL we measured the magnetization behavior using an Alternative Gradient Field Magnetometer (AGFM). The results indicate ferromagnetism at room temperature irrespective of the orientation of applied mnetic field (Fig. 5.6 &5.7).

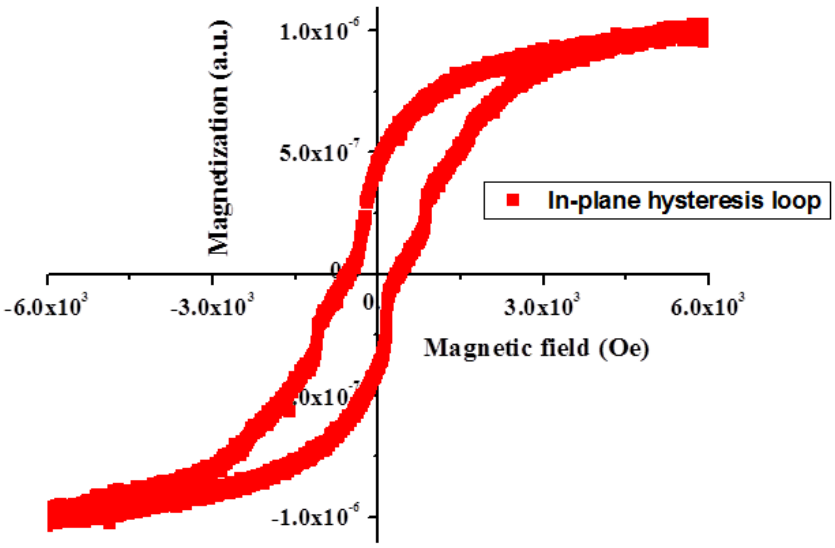

Figure 5.6 – Magnetization measurement of the Fe_xO_y – Au NPs NL material.

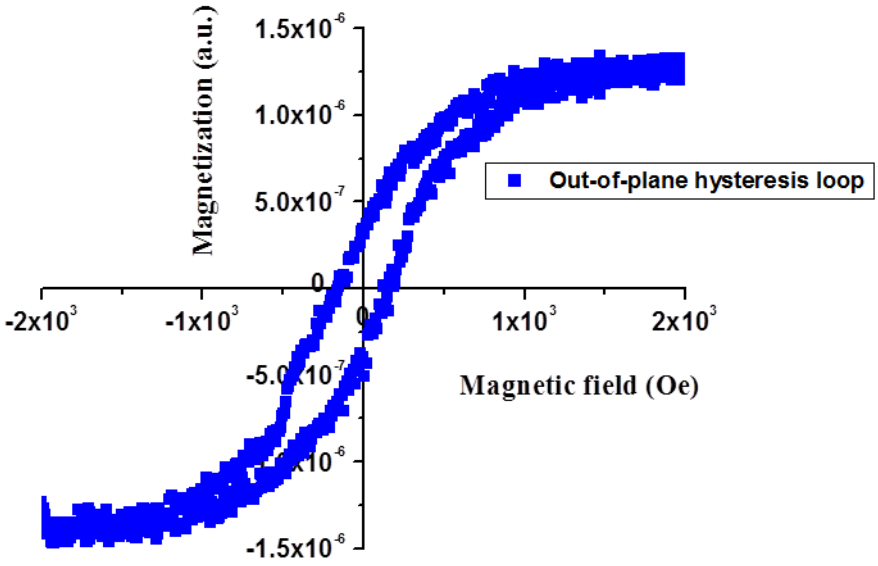

Figure 5.7 – Magnetization measurement of the Fe_xO_y – Au NPs NL material.

The magnetization hysteresis shows coercivity, χ_c, ~ 500-1000 Oe. Note that a field ~ 3000 Oe or 300mT is required to saturate the magnetization of the necklace device. This value is well above the applied field of 70 mT in the magneto-electrical measurements (Fig. 5.5). There are discontinuities in the middle section (near H ~ 0) of the hysteresis curve, resembling several small steps, regardless of the orientation of H. These step – like behavior is known as Barkhausen jumps[131] but are rarely observed at room temperature. Our observation may be attributed to the small size (2nm) in length of the FexOy material, leading to enhancement of Barhausen effect even at room temperature. This work is still under further investigation.

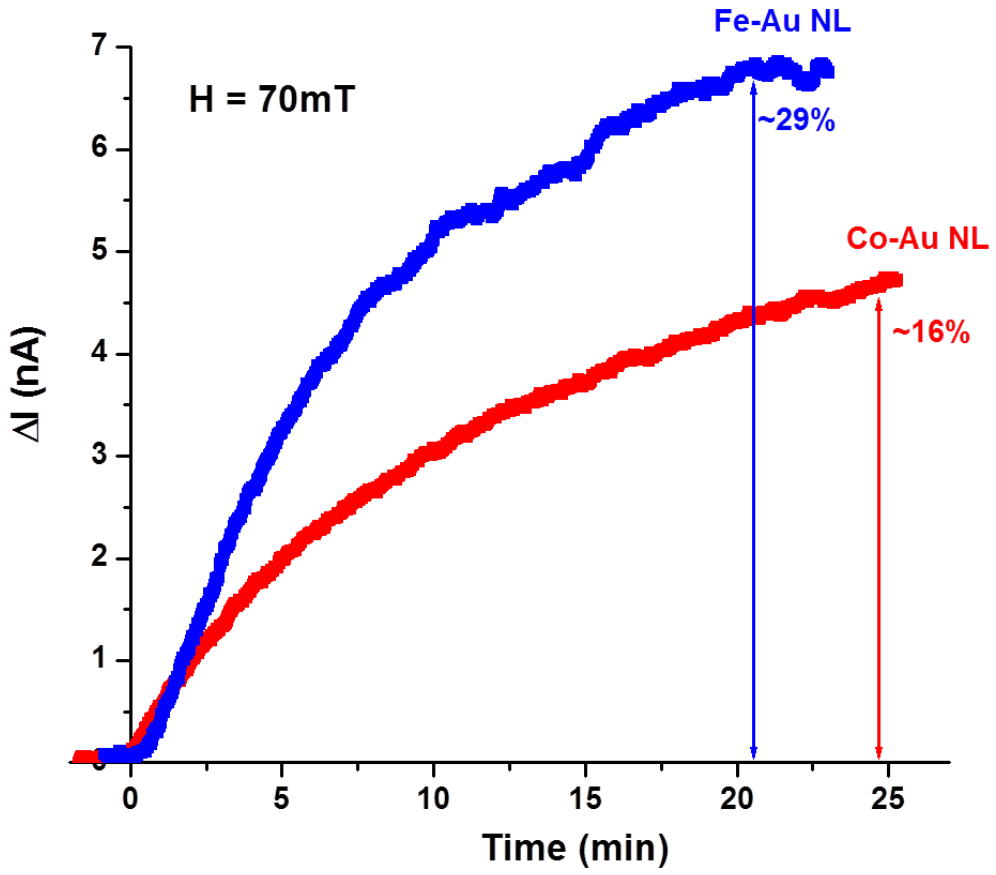

Figure 5.8 – "Spin – valve" like behavior of Fe_xO_y – Au NPs NL device.

In addition to Fe_xO_y – Au NPs NL, we also fabricated Cobalt (Co) – Au NPs NL using similar procedure. Because cobalt as an element is magnetic, the Co-Au NPs NL was not cemented with NH_4OH as in Fe_xO_y – Au NPs NL. A magneto – electrical measurement of Co-Au NPs NL device shows similar behavior as Fe_xO_y – Au NPs NL device but the extent is less significant (Fig. 5.8). Under constant applied bias, H = 70 mT, the current saturates in comparable amount of time (~ 20minutes) for both materials. The current gradient is larger for Fe_xO_y – Au NPs NL (~ 29%) as compared to Co – Au NPs NL (~ 18%). The lack of required cementing step allows simpler fabrication

procedure of Co – Au NPs NL, leading to more convenient and easier device processing. The large time domain (20 mins) of the device is reckoned as the extreme pinning of magnetic domain in the ultrathin Fe_xO_y and Co bridging materials and the low magnitude of applied H (70 mT) (saturation field was estimated as 300mT in Fig. 5.6 & 5.7).

5.4 SUMMARY

Quasi 1 – D (2 – D array with 1 – D locality) self-assembly of heterogeneous Fe_xO_y – Au NPs has been demonstrated. The nanomaterial has 3 salient features qualified for various applications in electronics, sensors, and solid state memory devices. First is the simple, easy fabrication process based on self-assembly of Au NPs. The negatively charged Au NPs were shown to be linked together via electrostatic interaction with positively charged Fe^{2+}, Fe^{3+} ions (and/or Co^{2+}). After formation of the necklace (Fig. 5.1 & 5.2) the bridging Fe^{2+}, Fe^{3+} ions were allowed to react with NH_4OH solution to form Fe_xO_y – Au NPs NL (Fig. 5.2). The second aspect of the device is the single electron behavior at room temperature. The I – V characteristics are non-linear, ideal for electronic switching applications. The threshold bias was significant, $V_T \sim 1.59V$ observed at 295K. The non-linearity of I – V relationship is attributed to the structural restriction of 1 – D locality. The third feature is the coupling of single electron effect and ferromagnetism (Fig. 5.5, 5.7). The cementing material, i.e. Fe_xO_y, was only 2 – 3nm in length but exhibits ferromagnetic property with a significant χ_c (coercivity) of over 500 Oe at room temperature. Thus the device can be a potential magneto – electrical switch or spin valve, a key component in solid state memory devices.

References

1. Grzelczak, M., Vermant, J., Furst, E. M. & Liz-Marzan, L. M. Directed Self-Assembly of Nanoparticles. *Acs Nano* **4**, 3591-3605 (2010).

2. Travesset, A. Self-Assembly Enters the Design Era. *Science* **334**, 183-184 (2011).

3. Lin, Y. *et al.* Self-directed self-assembly of nanoparticle/copolymer mixtures. *Nature* **434**, 55-59 (2005).

4. Whitesides, G. M. & Grzybowski, B. Self-assembly at all scales. *Science* **295**, 2418-2421 (2002).

5. Xu, L. G. *et al.* Nanoparticle assemblies: dimensional transformation of nanomaterials and scalability. *Chemical Society Reviews* **42**, 3114-3126 (2013).

6. Sun, S. H., Murray, C. B., Weller, D., Folks, L. & Moser, A. Monodisperse FePt nanoparticles and ferromagnetic FePt nanocrystal superlattices. *Science* **287**, 1989-1992 (2000).

7. Santhanam, V. & Andres, R. P. Microcontact printing of uniform nanoparticle arrays. *Nano Letters* **4**, 41-44 (2004).

8. Heath, J. R., Knobler, C. M. & Leff, D. V. Pressure/temperature phase diagrams and superlattices of organically functionalized metal nanocrystal monolayers: The influence of particle size, size distribution, and surface passivant. *Journal of Physical Chemistry B* **101**, 189-197 (1997).

9. Le, J. D. *et al.* DNA-templated self-assembly of metallic nanocomponent arrays on a surface. *Nano Letters* **4**, 2343-2347 (2004).

10. Aldaye, F. A. & Sleiman, H. F. Dynamic DNA templates for discrete gold nanoparticle assemblies: Control of geometry, modularity, write/wrase and structural switching. *Journal of the American Chemical Society* **129**, 4130 (2007).

11. Tang, Z. Y., Kotov, N. A. & Giersig, M. Spontaneous organization of single CdTe nanoparticles into luminescent nanowires. *Science* **297**, 237-240 (2002).

12. Thomas, J. R. Preparation and Magnetic Properties of Colloidal Cobalt Particles. *Journal of Applied Physics* **37**, 2914 (1966).

13. Nie, Z. H. *et al.* Self-assembly of metal-polymer analogues of amphiphilic triblock copolymers. *Nature Materials* **6**, 609-614 (2007).

14. Blunt, M. O. *et al.* Charge transport in cellular nanoparticle networks: Meandering through nanoscale mazes. *Nano Letters* **7**, 855-860 (2007).

15. Decher, G., Hong, J. D. & Schmitt, J. Buildup of Ultrathin Multilayer Films by A Self-Assembly Process .3. Consecutively Alternating Adsorption of Anionic and Cationic Polyelectrolytes on Charged Surfaces. *Thin Solid Films* **210**, 831-835 (1992).

16. Kotov, N. A., Dekany, I. & Fendler, J. H. Layer-By-Layer Self-Assembly of Polyelectrolyte-Semiconductor Nanoparticle Composite Films. *Journal of Physical Chemistry* **99**, 13065-13069 (1995).

17. Hong, X. *et al.* Fabrication of magnetic luminescent nanocomposites by a layer-by-layer self-assembly approach. *Chemistry of Materials* **16**, 4022-4027 (2004).

18. Decher, G., Lehr, B., Lowack, K., Lvov, Y. & Schmitt, J. New Nanocomposite Films for Biosensors - Layer-By-Layer Adsorbed Films of Polyelectrolytes, Proteins Or Dna. *Biosensors & Bioelectronics* **9**, 677-684 (1994).

19. Berry, V. & Saraf, R. F. Self-assembly of nanoparticles on live bacterium: An avenue to fabricate electronic devices. *Angewandte Chemie-International Edition* **44**, 6668-6673 (2005).

20. Atlanta: American Cancer Society, I. Breast Cancer Facts & Figures 2013-2014. *American Cancer Society* (2013).

21. American Cancer Society Breast Cancer. *American Cancer Society* (2014).

22. National Cancer Institute What You Need To Know About Breast Cancer. *National Cancer Institute* (2014).

23. National Cancer Institute Breast Cancer Screening. *National Cancer Institute* (2014).

24. Weedon-Fekjaer, H., Lindqvist, B. H., Vatten, L. J., Aalen, O. O. & Tretli, S. Breast cancer tumor growth estimated through mammography screening data. *Breast Cancer Research* **10**, (2008).

25. Saslow, D. *et al.* Clinical breast examination: Practical recommendations for optimizing performance and reporting. *Ca-A Cancer Journal for Clinicians* **54**, 327-344 (2004).

26. Guth, U. *et al.* Tumor size and detection in breast cancer: Self-examination and clinical breast examination are at their limit. *Cancer Detection and Prevention* **32**, 224-228 (2008).

27. Wellman P., Howe R.D., Dalton E. & Kern K.A. Breast tissue stiffness in compression is correlated to histological diagnosis. 1999. s.I.: Harvard BioRobotics Laboratory Technical Report.

28. Rangayyan, R. M., Mudigonda, N. R. & Desautels, J. E. L. Boundary modelling and shape analysis methods for classification of mammographic masses. *Medical & Biological Engineering & Computing* **38**, 487-496 (2000).

29. Dargahi, J. & Najarian, S. Human tactile perception as a standard for artificial tactile sensing - a review. *International Journal of Medical Robotics and Computer Assisted Surgery* **1**, 23-35 (2004).

30. Lederman, S. J. & Klatzky, R. L. Haptic perception: A tutorial. *Attention Perception & Psychophysics* **71**, 1439-1459 (2009).

31. Morley, J. W., Goodwin, A. W. & Dariansmith, I. Tactile Discrimination of Gratings. *Experimental Brain Research* **49**, 291-299 (1983).

32. Skedung, L. *et al.* Feeling Small: Exploring the Tactile Perception Limits. *Scientific Reports* **3**, (2013).

33. Wang, C. *et al.* User-interactive electronic skin for instantaneous pressure visualization. *Nature Materials* **12**, 899-904 (2013).

34. Hammock, M. L., Chortos, A., Tee, B. C. K., Tok, J. B. H. & Bao, Z. A. 25th Anniversary Article: The Evolution of Electronic Skin (E-Skin): A Brief History, Design Considerations, and Recent Progress. *Advanced Materials* **25**, 5997-6037 (2013).

35. Kaltenbrunner, M. *et al.* An ultra-lightweight design for imperceptible plastic electronics. *Nature* **499**, 458 (2013).

36. Schwartz, G. *et al.* Flexible polymer transistors with high pressure sensitivity for application in electronic skin and health monitoring. *Nature Communications* **4**, (2013).

37. Maheshwari, V. & Saraf, R. F. High-resolution thin-film device to sense texture by touch. *Science* **312**, 1501-1504 (2006).

38. Alvares, D., Wieczorek, L., Raguse, B., Ladouceur, F. & Lovell, N. H. Development of nanoparticle film-based multi-axial tactile sensors for biomedical applications. *Sensors and Actuators A-Physical* **196**, 38-47 (2013).

39. Mittendorfer, P. & Cheng, G. Humanoid Multimodal Tactile-Sensing Modules. *IEEE Transactions on Robotics* **27**, 401-410 (2011).

40. Dahiya, R. S., Metta, G., Valle, M. & Sandini, G. Tactile Sensing-From Humans to Humanoids. *IEEE Transactions on Robotics* **26**, 1-20 (2010).

41. Someya, T. *et al.* A large-area, flexible pressure sensor matrix with organic field-effect transistors for artificial skin applications. *Proceedings of the National Academy of Sciences of the United States of America* **101**, 9966-9970 (2004).

42. Cotton, D. P. J., Graz, I. M. & Lacour, S. P. A Multifunctional Capacitive Sensor for Stretchable Electronic Skins. *IEEE Sensors Journal* **9**, 2008-2009 (2009).

43. Metzger, C. *et al.* Flexible-foam-based capacitive sensor arrays for object detection at low cost. *Applied Physics Letters* **92**, (2008).

44. Sato, N. *et al.* Novel surface structure and its fabrication process for MEMS fingerprint sensor. *IEEE Transactions on Electron Devices* **52**, 1026-1032 (2005).

45. Dargahi, J., Parameswaran, M. & Payandeh, S. A micromachined piezoelectric tactile sensor for an endoscopic grasper - Theory, fabrication and experiments. *Journal of Microelectromechanical Systems* **9**, 329-335 (2000).

46. Kolesar, E. S. & Dyson, C. S. Object Imaging with A Piezoelectric Robotic Tactile Sensor. *Journal of Microelectromechanical Systems* **4**, 87-96 (1995).

47. Smith, C. S. Piezoresistance Effect in Germanium and Silicon. *Physical Review* **94**, 42-49 (1954).

48. Xiao, X. *et al.* High-Strain Sensors Based on ZnO Nanowire/Polystyrene Hybridized Flexible Films. *Advanced Materials* **23**, 5440 (2011).

49. Maekawa, H., Tanie, K. & Komoriya, K. A finger-shaped tactile sensor using an optical waveguide. 5, 403-408. 1993. Systems, Man and Cybernetics, 1993. 'Systems Engineering in the Service of Humans', Conference Proceedings., International Conference on.

50. Wang, A., He, S., Fang, X., Jin, X. & Lin, J. Optical Fiber Pressure Sensor Based on Photoelasticity and Its Application (Vol 10, Pg 1466, 1992). *Journal of Lightwave Technology* **10**, 2032 (1992).

51. Sarvazyan, A. & Egorov, V. Mechanical Imaging - a Technology for 3-D Visualization and Characterization of Soft Tissue Abnormalities: A Review. *Current Medical Imaging Reviews* **8**, 64-73 (2012).

52. A.J.Lawrence *et al.* Palpating Breast Cancer by Magnetic Resonance Elastography. *Proc. Int. Soc. Magn. Reson. Med.* **7**, (1999).

53. A.M.Galea & R.D.Howe TISSUE STIFFNESS FROM TACTILE IMAGING. *Proceedings of the Second Joint EMBS/BMES Conference* (2002).

54. Y.Wang, C.Nguyen, R.Srikanchana, Z.Geng & M.T.Freedman Tactile Mapping of Palpable Abnormalities for Breast Cancer Diagnosis. *IEEE* (1999).

55. Wellman, P. S., Dalton, E. P., Krag, D., Kern, K. A. & Howe, R. D. Tactile imaging of breast masses - First clinical report. *Archives of Surgery* **136**, 204-208 (2001).

56. Yegingil H.O. Breast cancer detection and differentiation using piezoelectric fingers. 2009. Drexel University.

57. Murayama, Y. *et al.* Development of a new instrument for examination of stiffness in the breast using haptic sensor technology. *Sensors and Actuators A-Physical* **143**, 430-438 (2008).

58. Ayyildiz, M., Guclu, B., Yildiz, M. Z. & Basdogan, C. An Optoelectromechanical Tactile Sensor for Detection of Breast Lumps. *IEEE Transactions on Haptics* **6**, 145-155 (2013).

59. S.O.Kasap *Principles of Electrical Engineering Materials and Devices*. Irwin McGraw-Hill, (1997).

60. Middleton, A. A. & Wingreen, N. S. Collective Transport in Arrays of Small Metallic Dots. *Physical Review Letters* **71**, 3198-3201 (1993).

61. Parthasarathy, R., Lin, X. M. & Jaeger, H. M. Electronic transport in metal nanocrystal arrays: The effect of structural disorder on scaling behavior. *Physical Review Letters* **87**, (2001).

62. Black, C. T., Murray, C. B., Sandstrom, R. L. & Sun, S. H. Spin-dependent tunneling in self-assembled cobalt-nanocrystal superlattices. *Science* **290**, 1131-1134 (2000).

63. Kane, J., Ong, J. & Saraf, R. F. Chemistry, physics, and engineering of electrically percolating arrays of nanoparticles: a mini review. *Journal of Materials Chemistry* **21**, 16846-16858 (2011).

64. Maheshwari, V., Kane, J. & Saraf, R. F. Self-assembly of a micrometers-long one-dimensional network of cemented Au nanoparticles. *Advanced Materials* **20**, 284 (2008).

65. Law, M., Goldberger, J. & Yang, P. D. Semiconductor nanowires and nanotubes. *Annual Review of Materials Research* **34**, 83-122 (2004).

66. Greaves, G. N., Greer, A. L., Lakes, R. S. & Rouxel, T. Poisson's ratio and modern materials. *Nature Materials* **10**, 823-837 (2011).

67. Lakes, R. Foam Structures with A Negative Poissons Ratio. *Science* **235**, 1038-1040 (1987).

68. Wen, X. *et al.* Crumpled and Collapsed Conformations in Graphite Oxide Membranes. *Nature* **355**, 426-428 (1992).

69. Grima, J. N., Jackson, R., Alderson, A. & Evans, K. E. Do zeolites have negative Poisson's ratios? *Advanced Materials* **12**, 1912 (2000).

70. Schmidt, C. F. *et al.* Existence of A Flat Phase in Red-Cell Membrane Skeletons. *Science* **259**, 952-954 (1993).

71. Bowick, M., Cacciuto, A., Thorleifsson, G. & Travesset, A. Universal negative Poisson ratio of self-avoiding fixed-connectivity membranes. *Physical Review Letters* **87**, (2001).

72. Hall, L. J. *et al.* Sign change of Poisson's ratio for carbon nanotube sheets. *Science* **320**, 504-507 (2008).

73. Engmann, J., Servais, C. & Burbidge, A. S. Squeeze flow theory and applications to rheometry: A review. *Journal of Non-Newtonian Fluid Mechanics* **132**, 1-27 (2005).

74. Silva, S. P. *et al.* Cork: properties, capabilities and applications. *International Materials Reviews* **50**, 345-365 (2005).

75. Grima, J. N. *et al.* Hexagonal Honeycombs with Zero Poisson's Ratios and Enhanced Stiffness. *Advanced Engineering Materials* **12**, 855-862 (2010).

76. Jin, T., Goo, N. S., Woo, S. C. & Park, H. C. Use of a Digital Image Correlation Technique for Measuring the Material Properties of Beetle Wing. *Journal of Bionic Engineering* **6**, 224-231 (2009).

77. Attard, D. & Grima, J. N. Modelling of hexagonal honeycombs exhibiting zero Poisson's ratio. *Physica Status Solidi B-Basic Solid State Physics* **248**, 52-59 (2011).

78. Olympio, K. R. & Gandhi, F. Zero Poisson's Ratio Cellular Honeycombs for Flex Skins Undergoing One-Dimensional Morphing. *Journal of Intelligent Material Systems and Structures* **21**, 1737-1753 (2010).

79. Butcher, D. T., Alliston, T. & Weaver, V. M. A tense situation: forcing tumour progression. *Nature Reviews Cancer* **9**, 108-122 (2009).

80. Lee, M. H. & Nicholls, H. R. Tactile sensing for mechatronics - a state of the art survey. *Mechatronics* **9**, 1-31 (1999).

81. Plinkert, P. K., Baumann, I. & Flemming, E. A tactile sensor for differentiation of tissue in minimally invasive ENT surgery. *Laryngo-Rhino-Otologie* **76**, 543-549 (1997).

82. Sakai, N., Tatsuta, M., Yano, H., Iishi, H. & Ishiguro, S. Diagnosis of the extent of gastric cancers by a new endoscopic ultrasonic tactile sensor. *Gastrointestinal Endoscopy* **51**, 69-73 (2000).

83. Engler, A. J., Sen, S., Sweeney, H. L. & Discher, D. E. Matrix elasticity directs stem cell lineage specification. *Cell* **126**, 677-689 (2006).

84. Maheshwari, V. & Saraf, R. F. Tactile devices to sense touch on a par with a human finger. *Angewandte Chemie-International Edition* **47**, 7808-7826 (2008).

85. King, C. H. *et al.* Tactile Feedback Induces Reduced Grasping Force in Robot-Assisted Surgery. *IEEE Transactions on Haptics* **2**, 103-110 (2009).

86. Stevens, M. M. & George, J. H. Exploring and engineering the cell surface interface. *Science* **310**, 1135-1138 (2005).

87. Gibson L.J. & Ashby M.F. *Cellular Solids: Structure and Properties*. Cambridge University Press: Cambridge, UK, (1997).

88. Nolte, A. J., Rubner, M. F. & Cohen, R. E. Determining the young's modulus of polyelectrolyte multilayer films via stress-induced mechanical buckling instabilities. *Macromolecules* **38**, 5367-5370 (2005).

89. Decher, G. Fuzzy nanoassemblies: Toward layered polymeric multicomposites. *Science* **277**, 1232-1237 (1997).

90. Maheshwari, V. & Saraf, R. F. High-resolution thin-film device to sense texture by touch. *Science* **312**, 1501-1504 (2006).

91. Fowler, R. H. & Nordheim, L. Electron emission in intense electric fields. *Proceedings of the Royal Society of London Series A-Containing Papers of A Mathematical and Physical Character* **119**, 173-181 (1928).

92. Cho, J., Char, K., Hong, J. D. & Lee, K. B. Fabrication of highly ordered multilayer films using a spin self-assembly method. *Advanced Materials* **13**, 1076-+ (2001).

93. Lee, C., Wei, X. D., Kysar, J. W. & Hone, J. Measurement of the elastic properties and intrinsic strength of monolayer graphene. *Science* **321**, 385-388 (2008).

94. Bolotin, K. I. *et al.* Ultrahigh electron mobility in suspended graphene. *Solid State Communications* **146**, 351-355 (2008).

95. Nair, R. R. *et al.* Fine structure constant defines visual transparency of graphene. *Science* **320**, 1308 (2008).

96. Bunch, J. S. *et al.* Impermeable atomic membranes from graphene sheets. *Nano Letters* **8**, 2458-2462 (2008).

97. Cocco, G., Cadelano, E. & Colombo, L. Gap opening in graphene by shear strain. *Physical Review B* **81**, (2010).

98. Siegel, R., Ma, J. M., Zou, Z. H. & Jemal, A. Cancer Statistics, 2014. *Ca-A Cancer Journal for Clinicians* **64**, 9-29 (2014).

99. Carney, P. A. *et al.* Individual and combined effects of age, breast density, and hormone replacement therapy use on the accuracy of screening mammography. *Annals of Internal Medicine* **138**, 168-175 (2003).

100. Hislop, T. G., Worth, A. J., Kan, L. & Rousseau, E. Post screen-detected breast cancer within the Screening Mammography Program of British Columbia. *Breast Cancer Research and Treatment* **42**, 235-242 (1997).

101. Skinner, K. A., Silberman, H., Sposto, R. & Silverstein, M. J. Palpable breast cancers are inherently different from nonpalpable breast cancers. *Annals of Surgical Oncology* **8**, 705-710 (2001).

102. McDonald, S., Saslow, D. & Alciati, M. H. Performance and reporting of clinical breast examination: A review of the literature. *Ca-A Cancer Journal for Clinicians* **54**, 345-361 (2004).

103. Egorov, V. & Sarvazyan, A. P. Mechanical imaging of the breast. *IEEE Transactions on Medical Imaging* **27**, 1275-1287 (2008).

104. Pan, L. J. *et al.* An ultra-sensitive resistive pressure sensor based on hollow-sphere microstructure induced elasticity in conducting polymer film. *Nature Communications* **5**, (2014).

105. Friedman, R. J., Rigel, D. S. & Kopf, A. W. Early Detection of Malignant-Melanoma - the Role of Physician Examination and Self-Examination of the Skin. *Ca-A Cancer Journal for Clinicians* **35**, 130-151 (1985).

106. Nguyen, C., Maheshwari, V. & Saraf, R. F. Ultrasoft 100 nm Thick Zero Poisson's Ratio Film with 60% Reversible Compressibility. *Nano Letters* **12**, 2171-2175 (2012).

107. Ostrikov, K., Neyts, E. C. & Meyyappan, M. Plasma nanoscience: from nano-solids in plasmas to nano-plasmas in solids. *Advances in Physics* **62**, 113-224 (2013).

108. Ostrikov, K., Cvelbar, U. & Murphy, A. B. Plasma nanoscience: setting directions, tackling grand challenges. *Journal of Physics D-Applied Physics* **44**, (2011).

109. Kisliuk, P. Electron Emission at High Fields Due to Positive Ions. *Journal of Applied Physics* **30**, 51-55 (1959).

110. Ono, T., Sim, D. Y. & Esashi, M. Micro-discharge and electric breakdown in a micro-gap. *Journal of Micromechanics and Microengineering* **10**, 445-451 (2000).

111. Strong, F., Skinner, J. L. & Tien, N. C. Electrical discharge across micrometer-scale gaps for planar MEMS structures in air at atmospheric pressure. *Journal of Micromechanics and Microengineering* **18**, (2008).

112. Modi, A., Koratkar, N., Lass, E., Wei, B. Q. & Ajayan, P. M. Miniaturized gas ionization sensors using carbon nanotubes. *Nature* **424**, 171-174 (2003).

113. Sadeghian, R. B. & Kahrizi, M. A novel miniature gas ionization sensor based on freestanding gold nanowires. *Sensors and Actuators A-Physical* **137**, 248-255 (2007).

114. Hou, Z. Y. *et al.* MEMS-based microelectrode system incorporating carbon nanotubes for ionization gas sensing. *Sensors and Actuators B-Chemical* **127**, 637-648 (2007).

115. Chen, Y. & Zhang, J. Ultra-Low Breakdown Voltage of Field Ionization in Atmospheric Air Based on Silicon Nanowires. *Plasma Science & Technology* **15**, 1081-1087 (2013).

116. Postma, H. W. C., Teepen, T., Yao, Z., Grifoni, M. & Dekker, C. Carbon nanotube single-electron transistors at room temperature. *Science* **293**, 76-79 (2001).

117. Bozyigit, D., Wood, V., Shirasaki, Y. & Bulovic, V. Study of field driven electroluminescence in colloidal quantum dot solids. *Journal of Applied Physics* **111**, (2012).

118. Wood, V. *et al.* Electroluminescence from Nanoscale Materials via Field-Driven Ionization. *Nano Letters* **11**, 2927-2932 (2011).

119. Ong, J. K. Y., Nguyen, C. V., Sayood, S. & Saraf, R. F. Imaging Electroluminescence from Individual Nanoparticles in an Array Exhibiting Room Temperature Single Electron Effect. *Acs Nano* **7**, 7403-7410 (2013).

120. Park, B. G. *et al.* A spin-valve-like magnetoresistance of an antiferromagnet-based tunnel junction. *Nature Materials* **10**, 347-351 (2011).

121. Monsma, D. J., Vlutters, R. & Lodder, J. C. Room temperature - Operating spin-valve transistors formed by vacuum bonding. *Science* **281**, 407-409 (1998).

122. Sato, R. & Mizushima, K. Spin-valve transistor with an Fe/Au/Fe(001) base. *Applied Physics Letters* **79**, 1157-1159 (2001).

123. Gardelis, S., Smith, C. G., Barnes, C. H. W., Linfield, E. H. & Ritchie, D. A. Spin-valve effects in a semiconductor field-effect transistor: A spintronic device. *Physical Review B* **60**, 7764-7767 (1999).

124. Hill, E. W., Geim, A. K., Novoselov, K., Schedin, F. & Blake, P. Graphene spin valve devices. *IEEE Transactions on Magnetics* **42**, 2694-2696 (2006).

125. Wikipedia contributors. Personal Computer. Wikipedia, The Free Encyclopedia . 2014.

126. Baibich, M. N. *et al.* Giant Magnetoresistance of (001)Fe/(001) Cr Magnetic Superlattices. *Physical Review Letters* **61**, 2472-2475 (1988).

127. Nobel Media AB 2013. The 2007 Nobel Prize in Physics - Press Release. Nobelprize.org . 2014.

128. Yuasa, S., Nagahama, T., Fukushima, A., Suzuki, Y. & Ando, K. Giant room-temperature magnetoresistance in single-crystal Fe/MgO/Fe magnetic tunnel junctions. *Nature Materials* **3**, 868-871 (2004).

129. Jungwirth, T., Wunderlich, J. & Olejnik, K. Spin Hall effect devices. *Nature Materials* **11**, 382-390 (2012).

130. Sbiaa, R. *et al.* Spin transfer torque switching for multi-bit per cell magnetic memory with perpendicular anisotropy. *Applied Physics Letters* **99**, (2011).

131. McClure Jr, J. C. S. K. The magnetic Barkhausen effect. *Critical Reviews in Solid State and Material Sciences* **6**, 45-83 (1976).